Institute of Thermoelectricity, Academy of Sciences and Ministry of Education and Science of Ukraine

Journal of THERMOELECTRICITY

International Research

Founded in December, 1993

published 6 times a year

No. 4 *2014*

Editorial Board

International Editorial Board

Founders - National Academy of Sciences, Ukraine
Institute of Thermoelectricity of National Academy of Sciences and Ministry of Education and Science of Ukraine

Certificate of state registration № КВ 15496-4068 ПР

Editorial office manager O. Pugantseva

Approved for printing by the Academic Council of Institute of Thermoelectricity of the National Academy of Sciences and Ministry of Education and Science, Ukraine

Address of editorial office:
Ukraine, 58002, Chernivtsi, General Post Office, P.O. Box 86.
Phone: +(380-372) 90 31 65.
Fax: +(380-3722) 4 19 17.
E-mail: jt@inst.cv.ua
http://www.jt.inst.cv.ua

Signed for publication 25.10.14. Format 70×108/16. Offset paper №1. Offset printing.
Printer's sheet 11.1. Publisher's signature 9.2. Circulation 400 copies. Order 6.

Printed from the layout original made by "Journal of Thermoelectricity" editorial board
in the printing house of "Bukrek" publishers,
10, Radischev Str., Chernivtsi, 58000, Ukraine

CONTENTS

A.A. Snarskii[1,2], I.V. Bezsudnov[3,4]

[1]Dep. of general and theoretical physics, National Technical University "KPI", Kiev, Ukraine
[2]Institute for Information Recording NAS Ukraine, Kiev, Ukraine
[3]Nauka – Service JSC, Moscow, Russia
[4]ITMO University, St. Petersburg, Russia

A.A. Snarskii

I.V. Bezsudnov

THERMOELECTRIC DEVICE IN PERIODIC STEADY STATE

We propose a rotating thermoelectric (TE) device comprised of a single TE conductor operating in two periodic steady state modes: switching periodic mode (P-mode) when the hot and cold ends of the TE conductor are periodically instantly reversed and continuous sinusoidal mode (S-mode) when the temperature of TE conductor edges varies continuously according to sine wave. Power generation and cooling regimes of the rotating (TE) device in the periodic steady state were studied analytically. The efficiency and cooling temperature of the rotating TE device was found to depend not only on a dimensionless TE figure of merit, but also upon an additional dimensionless parameter comprising of the rotation period, the size and the thermal diffusivity of the TE conductor. The proposed analytical method can be generalized to even more complex timing modes and allows solving the optimization problem for TE device parameters. We investigated whether it is possible to achieve better performance for the rotating TE device comparing to conventional stationary steady state, S-mode was shown to demonstrate deeper cooling at certain times.

Key words: thermoelectric device, periodic steady state, figure of merit, power generation, cooling.

Introduction

The main way to improve the efficiency of thermoelectric (TE) devices – power generators, coolers etc. is to increase the dimensionless figure of merit of TE materials, $ZT = \alpha^2 \sigma T / \kappa$, where α is the thermopower or the Seebeck coefficient, σ is the electrical conductivity, T is the absolute temperature, κ is the thermal conductivity.

Unlike superconductivity, where new materials with high temperatures of transition to the superconducting state have been invented, the progress in ZT improvement of TE materials is quite disappointing. Thus, for example, at room temperature ($T = 300°\mathrm{K}$) since 1950 to the present time the figure of merit has increased from $ZT \sim 1$ to $ZT \sim 1.2 \div 1.3$ only [1-5]. Moreover, today there are no commercially available TE materials with $ZT \sim 1.3$. Indeed, for common appliances use, for example, in the household or industrial refrigeration, TE materials with the figure of merit $ZT \geq 2.0$ [6-8] are required. There were expectations that the success could be achieved using tunneling and other quantum effects in nanostructured TE materials [5, 9-13]. However, there has been no significant progress so far.

The parameters of TE device in the stationary steady state depend only on the figure of merit ZT [14]. The higher ZT, the lower cooling temperature can be reached.

In transient modes, the efficiency of TE device is affected by many other parameters, such as the temperature diffusivity, the current pulse duration in a pulsed mode [6, 15-20], the relaxation time of thermal processes etc. Such transient modes are constantly in the focus of researchers [5, 15-29],

because they have advantages over the steady state. For example, at certain times in a pulsed cooling mode [15-20] deeper cooling can be reached. Optimization of transient mode parameters allows improving the operation of TE device as compared with the steady state even if the same TE materials are used.

Qualitatively, the improved performance of TE devices in transient mode is possible due to the fact that the relaxation time of electrical processes is negligible compared to the relaxation time of thermal processes [14]. When current flows through TE device in cooling regime in the stationary steady state, the Peltier heat removed from the cold junction and the Joule heat generated in the TE conductor are balanced. Increased current and, consequently, increased Joule heat would make the TE device inoperative. In the transient state, due to the relaxation times difference, the heat balance is uncompensated. Higher current passed through the TE device for a short time delivers additional cooling. Optimization of length and shape of the current pulses can give deeper cooling for limited time intervals [18] or cooling of small objects in a shorter time [19].

The pulsed cooling [21-24] consists of two major phases. The first phase is highly transient one implementing fast and deep cooling, the second phase is the relaxation, in this phase, as a rule, the TE device is out of use. Thus, if in the pulsed mode the second phase duration is equal to or longer than the relaxation time of thermal processes (i.e. the period during which thermal equilibrium has time to be established), in the mode in hand the characteristic times (the period of change in the boundary conditions in generator mode, or current in cooling mode) are, generally speaking, shorter than the relaxation time of thermal processes.

This paper studies TE devices operating in the periodic steady state mode. Unlike pulsed cooling, a TE device in the periodic steady state mode operates continuously. The basic question considered here is whether it is possible in this periodic steady state mode to achieve better performance relative to the stationary steady state mode, at least better at certain times. In this study, we omit particular technical details such as the contact resistance of the plates, the lateral heat transfer, parameters of the cooled object etc.

The proposed TE devices consist of a single TE conductor with the constant cross section made of thermoelectric material and the role of second conductor is played by the body of TE device, which is an ordinary metal conductor.

We consider two types of periodic steady state modes for proposed TE devices: the switching periodic mode (*P*-mode) when the hot and cold ends of TE conductor are periodically instantly reversed and the continuous sinusoidal mode (*S*-mode) when the temperature of TE conductor edges varies continuously according to sine wave.

For periodic steady state modes, along with ZT we found a new dimensionless parameter that is a combination of the period of temperature change, the TE conductor size and its temperature diffusivity. The optimal value of above parameter was calculated.

In the next section, TE devices in *P*- and *S*-modes are schematically described. The following sections contain analytical calculations and results for *P*-mode in the power generation and cooling regimes, and for *S*-mode cooling regime. The last section presents discussion and conclusions.

1. Model of TE device in a periodic steady state

The TE device operating in a switching periodic mode (*P*-mode) is shown schematically in Fig. 1*a*. The TE conductor turns periodically in the plane of the figure and its hot and cold ends (junctions) are instantly swapped.

The TE device operating in a continuous sinusoidal mode (*S*-mode) is presented schematically in Fig 1*b*. Let the TE conductor rotate in the hole of the orifice plate with linear temperature distribution from up to down (see Fig. 1*b*), consequently at the ends (junctions) of the rotating TE conductor (see Fig. 1*b*) the temperature varies continuously by sine wave.

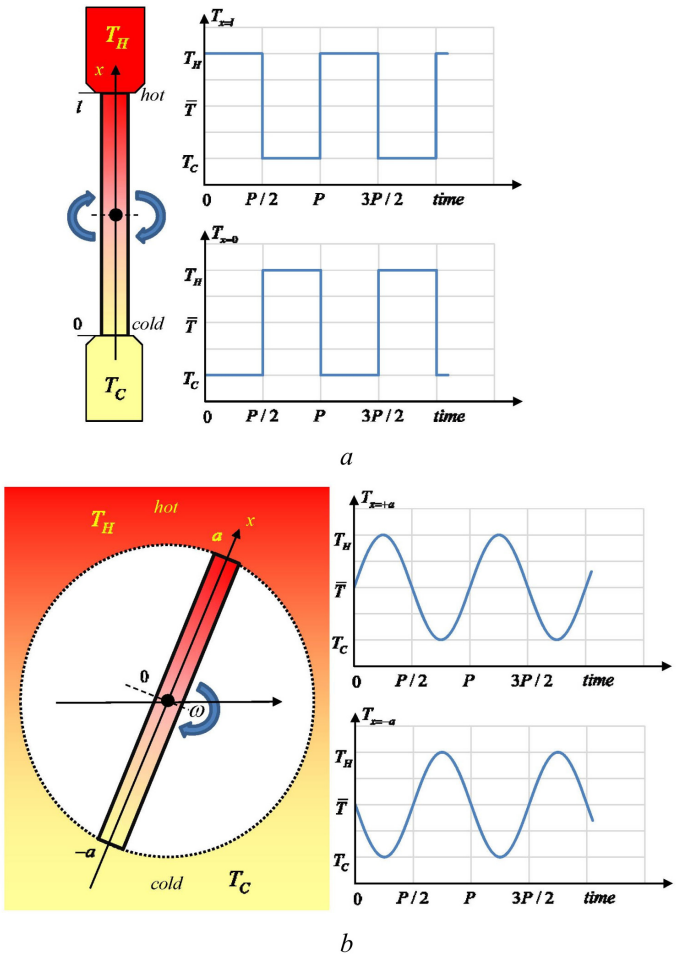

Fig. 1. Schematic sketch of proposed TE devices operating in a) the switching periodic mode (P-mode) and b) the continuous sinusoidal mode (S-mode).

The TE device (Fig. 1*a*, *b*) consists of a single TE conductor with a constant cross section S of length $l = 2a$. Other parts of TE device do not have TE properties. The period of rotation P is fixed.

Performing further analytical calculations for both *P*- and *S*-modes we assume for convenience that a TE conductor is fixed in plane but the temperature at its ends (junctions) varies according to the periodic law specific for each mode.

The heat conduction equation for the TE conductor in TE devices has the standard form [14]

$$c_v \rho_0 \frac{\partial T}{\partial t} = \kappa \frac{\partial^2 T}{\partial x^2} + \rho j^2, \qquad (1)$$

where t is the time, x is the coordinate along TE conductor, $T(x,t)$ is the temperature of TE conductor, $j(t)$ is the current density in TE conductor, $\rho = 1/\sigma$ is the specific resistivity, κ is the thermal conductivity, c_v is the specific heat, ρ_0 is the bulk density, and $\chi = \kappa / c_v \rho_0$ is the thermal diffusivity.

For *P*-mode (Fig. 1*a*) the boundary conditions are as follows

$$\begin{aligned} T(x,t)\big|_{x=0} &= \overline{T} - T_0\theta(t) \\ T(x,t)\big|_{x=l} &= \overline{T} + T_0\theta(t) \end{aligned}, \tag{2}$$

where $\overline{T}$ is the external mean temperature, T_0 is the amplitude of variation of the external temperature, the function $\theta(t)$ is set to -1 in the even half-periods and in the odd ones it is equal to $+1$

$$\theta(t) = \begin{cases} +1, & nP < t < (n+1/2)P \\ -1, & (n+1/2)P < t < (n+1)P \end{cases}. \tag{3}$$

S-mode (Fig 1*b*) corresponds to the case when the temperature of the ends (junctions) of TE conductor varies continuously according to sine wave, therefore the boundary conditions in *S*-mode are

$$T\left(x,t\right)\big|_{x=\pm a} = \overline{T} \pm T_0 \sin\left(\omega t\right), \tag{4}$$

where $\omega = P/2\pi$ is the angular frequency of temperature change, $\overline{T}$ and T_0 have the same meanings as in *P*-mode.

Thus, during the period the TE conductor in P- and S-modes has the maximum temperature at the hot end (junction) $T_H = \overline{T} + T_0$ and minimal at cold end (junction) $T_C = \overline{T} - T_0$.

The current that flows through the TE conductor in cooling regime is set to

$$\begin{aligned} j &= j_0\theta(t), && (P-\text{mode}) \\ j &= j_0 \sin\left(\frac{2\pi}{P}t\right). && (S-\text{mode}) \end{aligned} \tag{5}$$

In the power generation regime the TE conductor current is calculated according to Seebeck's law $j \sim \alpha\Delta T$, where α is the thermo power or the Seebeck coefficient, we assume it to be temperature independent

$$\begin{aligned} j &= \alpha\Delta T, \quad \Delta T = 2T_0, && (\text{P}-\text{mode}) \\ j &= \alpha\Delta T, \quad \Delta T = 2T_0 \sin\left(\frac{2\pi}{P}t\right). && (\text{S}-\text{mode}) \end{aligned} \tag{6}$$

where $2T_0 = \Delta T$ is the maximum temperature difference between the hot and cold ends (junctions).

The equation (1) with the boundary conditions (2) or (4) and the relations for the TE conductor current (5) or (6) in the periodic steady state are solved analytically in the following sections.

2. Temperature distribution and heat fluxes in the switching periodic mode (*P*-mode)

2.1. The temperature distribution in *P*-mode

The solution of the equation (1) with the boundary conditions (2) for *P*-mode was analytically calculated using the method described in [30, Chapter 15].

First, we represent $T(x,t)$ in the following form

$$T(x,t) = \overline{T} + \frac{\rho j^2}{2\kappa}x(l-x) + \tilde{T}(x,t). \tag{7}$$

Then (1) gives the equation for $\tilde{T}(x,t)$

$$\frac{\partial\tilde{T}}{\partial t} = \chi\frac{\partial^2\tilde{T}}{\partial x} \tag{8}$$

and the boundary conditions (2) become

$$\left.\tilde{T}(x,t)\right|_{x=0} = -T_0\theta(t),$$
$$\left.\tilde{T}(x,t)\right|_{x=l} = +T_0\theta(t). \tag{9}$$

Next, according to [30] we write $\tilde{T}(x,t)$ in the form of a series

$$\tilde{T}(x,t) = \sum_{k=1}^{\infty} T_k(t)\sin\frac{k\pi}{l}x\,. \tag{10}$$

Substituting $\tilde{T}(x,t)$ (10) in Eq. (8), integrating by parts twice and using the boundary conditions (9) we obtain the following relation for $T_k(t)$

$$\frac{dT_k}{dt} + \chi\left(\frac{k\pi}{l}\right)T_k = -\chi\frac{2\pi k}{l^2}T_0\theta(t)\left[1+(-1)^k\right]. \tag{11}$$

The solution of the ordinary differential equation (11) is as follows [31-33]

$$T_k(t) = T_0 e^{-A_k t} - \chi\frac{2\pi k}{l^2}\left[1+(-1)^k\right]e^{-A_k t}\int_0^t \theta(t)e^{A_k t}dt\,, \tag{12}$$

where

$$A_k = \chi\left(\frac{k\pi}{l}\right)^2. \tag{13}$$

At longer times when the periodic steady state is reached, the first transient term has to disappear.

Let $t = mP + \tau$ where $0 < \tau < P/2$ and $m >> 1$, i.e. the time τ is measured from the beginning of the period and at that time the left junction ($x = 0$) is cold and the right one ($x = l$) is hot (see Fig. 1*a*). Then, according to (3), the integral in (12) is divided into three terms, which represent the sum of odd ($\theta(t) = +1$) and even ($\theta(t) = -1$) half-periods, and the third term, which depends on τ

$$\int_0^t \theta(t)e^{A_k t}dt = \sum_{n=0}^{m}\int_{nP}^{\left(n+\frac{1}{2}\right)P} e^{A_k t}dt + -\sum_{n=0}^{m}\int_{\left(n+\frac{1}{2}\right)P}^{(n+1)P} e^{A_k t}dt + \int_{(m+1)P}^{(m+1)P+\tau} e^{A_k t}dt\,. \tag{14}$$

Calculating integrals in the first and second terms of (14) and considering $e^{-mA_k} << 1$ at $m >> 1$, we obtain geometric progressions. The sums of the above progressions we use in (12) to get the final formulae

$$T_k(\tau) = -T_0\frac{2}{k\pi}\left[1+(-1)^k\right] + 2T_0\frac{2}{k\pi}\left[1+(-1)^k\right]\frac{e^{-A_k t}}{1+e^{A_k\frac{P}{2}}}. \tag{15}$$

Substituting now (15) in (1) and considering that

$$\sum_{k=1}^{\infty}\frac{1}{k}\sin\frac{k\pi}{l}x = \frac{\pi}{2}\left(1-\frac{x}{l}\right), \tag{16}$$

we obtain

$$\tilde{T}(x,\tau) = -T_0\left(1-2\frac{x}{l}\right) + T_0\sum_{k=1}^{\infty}N_k e^{-A_k\tau}\sin\frac{k\pi}{l}x\,, \tag{17}$$

where

$$N_k = \frac{4}{k\pi}\cdot\frac{1+(-1)^k}{1-e^{A_k\frac{P}{2}}}. \tag{18}$$

Finally, the solution (1) with the boundary conditions (3) for *P*-mode has the form

$$T(x,\tau)=\overline{T}+\frac{\rho j^2}{2\kappa}x(l-x)-T_0\left(1-2\frac{x}{l}\right)+T_0\sum_{k=1}^{\infty}N_k e^{-A_k\tau}\sin\frac{k\pi}{l}x, \qquad (19)$$

where τ belongs to $[0\ldots P/2]$.

Fig. 2 shows the temperature distribution along the TE conductor in *P*-mode at different times.

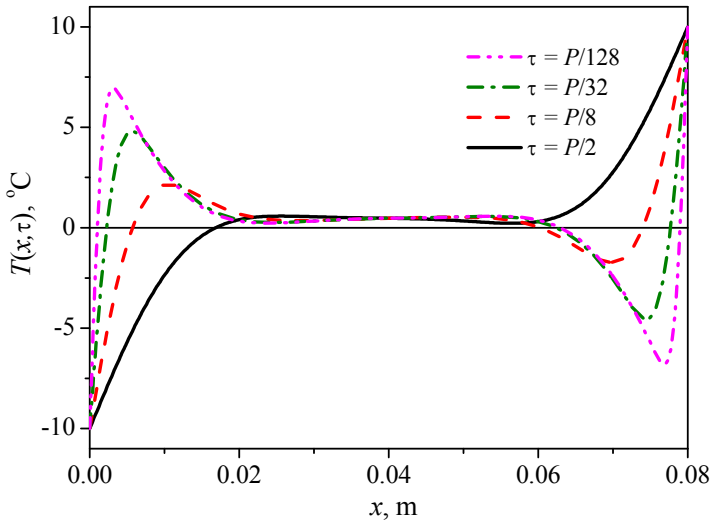

Fig. 2. Temperature distribution of TE conductor in P-mode at different times measured from the beginning of the period $P/128...P/2$. External temperatures: $\overline{T}=0°C$, $T_0=10°C$, TE conductor length $l=0.08\,m$, TE material parameters $\kappa=1.7\,W/mK$, $\chi=1.2\cdot10^{-6}\,m^2/s$, current density $j=0.1\cdot10^6\,A/m^2$ and rotation period $P=1s$.

At $t=P,\ 2P,\ 3P,\ldots$ the temperature of TE conductor edges is changing instantly. Then after this leap the TE conductor starts warming up, it is clearly seen from Fig. 2, but there is still part of TE conductor with the temperature $T(x,\tau)<\overline{T}$. Eventually, the size of this part decreases and its temperature increases.

Selected TE conductor and operational parameters show the case when temperature in the middle of the TE conductor is stable, i.e. heat waves do not enter deeply the TE conductor. It is similar to permafrost, when a periodic variation of the temperature on Earth's surface does not affect the temperature at a certain depth.

It should be noted also that the temperature in the middle of TE conductor is slightly higher than $\overline{T}$ because of the emitted Joule heat. When no current flows the temperature in the center of TE conductor, of course, would be equal to $\overline{T}$.

2.2. Power generation efficiency in *P*-mode

The power generation efficiency η of TE device in P-mode depends on the heat flux coming into the hot junction and coming out of the cold junction of the TE conductor (at $x=0$ and $x=l$ respectively) [14]. The heat flux density q_x is the sum of the flux densities created by the temperature distribution $\sim\partial T/\partial x$ and the Peltier heat flux $\Pi\mathbf{j}$, where $\Pi=\alpha T$ is the Peltier coefficient (we assume that the thermoEMF or the Seebeck coefficient α is temperature independent).

$$q_x=-\kappa\frac{\partial T}{\partial x}-\alpha Tj\ . \qquad (20)$$

We find the heat flux at cold $\dot{Q}_C$ and hot $\dot{Q}_H$ junctions using (19)

$$\dot{Q}_C = q_x S\big|_{x=0} = -\frac{\rho J^2}{2}\frac{l}{S} - \kappa\frac{2T_0}{l}S - \kappa T_0 S\sum_{k=1}^{\infty}\frac{k\pi}{l}N_k e^{-A_k\tau} + \alpha T_c J\,, \tag{21}$$

$$\dot{Q}_H = q_x S\big|_{x=l} = -\frac{\rho J^2}{2}\frac{l}{S} - \kappa\frac{2T_0}{l}S - \kappa T_0 S\sum_{k=1}^{\infty}(-1)^k\frac{k\pi}{l}N_k e^{-A_k\tau} + \alpha T_H J\,. \tag{22}$$

Here S is the cross section of TE conductor, J is the current flows through TE conductor. J is governed by the ε generated according to the Seebeck effect $\varepsilon = \alpha(T_H - T_C)$ and by connected in series the TE conductor resistance $r = \rho l / S$ and the load resistance R:

$$J = \alpha\frac{T_H - T_C}{r + R} = \alpha\frac{2T}{r(1+\Omega)}, \qquad \Omega = \frac{r}{R}\,. \tag{23}$$

The signs of the Peltier heat terms in (21) and (22) are selected in the way that the flux positive direction is from the hot to cold junction i.e. the heat flux coming to the hot junction ($x = l$) and coming out of the cold ($x = 0$) junction is set to be positive.

The heat coming out of the hot Q_H and coming to the cold Q_C junctions depends on time, therefore to get the efficiency η, we have to integrate Q_H and Q_C for a certain time, such time for *P*-mode is $P/2$ – half of the period:

$$Q_H = \int_0^{P/2}\dot{Q}_H d\tau, \qquad Q_C = \int_0^{P/2}\dot{Q}_C d\tau\,. \tag{24}$$

Substituting in (24) the expressions for $\dot{Q}_H$ (21) and $\dot{Q}_C$ (22) we find

$$\left.\begin{aligned}\frac{1}{P/2}Q_C &= \frac{1}{2}rJ^2 + \frac{2T_0}{l}S\kappa_e + \alpha T_c J\\ \frac{1}{P/2}Q_H &= -\frac{1}{2}rJ^2 + \frac{2T_0}{l}S\kappa_e + \alpha T_H J\end{aligned}\right\}, \tag{25}$$

where the renormalized thermal conductivity is

$$\kappa_e = \kappa\left[1 + \frac{4\mu_0^2}{\pi}\sum_{k=1}^{\infty}\frac{1+(-1)^k}{(k\pi)^2}th\left(A_k\frac{P}{4}\right)\right] \tag{26}$$

and

$$\mu_0^2 = l^2\frac{1}{P\chi}\,. \tag{27}$$

Comparing the relations (25) and (26) for *P*-mode and the formulae for the stationary steady state [14], one can realize that they differ only in the thermal conductivity value. The efficiency η in the stationary steady state depends only on the thermal conductivity κ, but in *P*-mode it depends upon the renormalized thermal conductivity κ_e (26) which is a complex parameter proportional not only to the TE conductor thermal conductivity κ, but also to the length of TE conductor, the switching period P and the thermal diffusivity χ.

Therefore, the corresponding expression for the efficiency $\eta = (Q_H - Q_C)/Q_H$ for *P*-mode is similar to the stationary steady state but it uses the renormalized thermal conductivity κ_e (26). The appropriate calculations can be found for instance in [14] and below is the final expression

$$\eta = \frac{Z_e \Delta T \Omega}{(1+\Omega)^2 \left[1 + \frac{Z_e T_H}{1+\Omega} - \frac{1}{2} \frac{Z_e \Delta T}{(1+\Omega)^2} \right]}, \tag{28}$$

where $Z_e = \sigma\alpha^2 / \kappa_e$ is a dimensionless TE figure of merit renormalized using (26).

As in the stationary steady state [14], the maximum efficiency η in *P*-mode is achieved at the optimal ratio $\Omega_{opt} = R / r = \sqrt{1 + Z_e \overline{T}}$. Using Ω_{opt} in (28) we find the value of maximal efficiency $\eta_{\max}$ for *P*-mode that depends only on T_H, T_C and Z_e

$$\eta_{\max} = \frac{\Delta T}{T_H} \frac{\sqrt{1 + Z_e \overline{T}} - 1}{\sqrt{1 + Z_e \overline{T}} - \frac{T_C}{T_H}} . \tag{29}$$

The maximum efficiency $\eta_{\max}$ is a monotonically increasing function of Z_e, thus higher Z_e and, accordingly, lower κ_e yields a better $\eta_{\max}$ value.

The renormalized thermal conductivity κ_e in *P*-mode (26) is always greater than κ, $\kappa_e > \kappa$, thus the efficiency in *P*-mode (28) is always less than the efficiency in the stationary steady state. In the case, when $\chi P \pi^2 / 4l > 3$, the hyperbolic tangent in (26) is nearly one and considering $\sum_{k=1}^{\infty} \left[\left(1 + (-1)^k\right) \Big/ (k\pi)^2 \right] = 1/12$ we get the approximated expression for the renormalized thermal conductivity

$$\kappa_e \approx \kappa \left(1 + \frac{1}{3} {\mu_0}^2 \right). \tag{30}$$

To have the efficiency of TE device in P-mode as high as possible, we need $\kappa_e \to \kappa$ or $\mu_0^2 \to 0$ (30). The latter means higher χ values or shorter lengths l of the TE conductor. In other words, for half of the period the TE conductor has to be warmed almost as the TE conductor in the stationary steady state.

2.3. Cooling in *P*-mode

Calculations for the cooling regime in *P*-mode are similar to those for the efficiency, except that it must be borne in mind that the current is determined by (5) $J = J_0 \theta(t)$ rather than by the Seebeck effect. The optimal current J_{opt} will minimize the cooling temperature or maximize the coefficient of performance K.

The heat fluxes $\dot{Q}_C$ and $\dot{Q}_H$ in *P*-mode cooling regime differ from (21) and (22) only by the signs of the Peltier heat term because the current in the TE conductor flows in the direction opposite to power generation regime.

$$\left.\begin{aligned} \frac{1}{P/2} Q_C &= \frac{1}{2} r J^2 + \frac{2T_0}{l} S\kappa_e - \alpha T_C J \\ \frac{1}{P/2} Q_H &= -\frac{1}{2} r J^2 + \frac{2T_0}{l} S\kappa_e - \alpha T_H J \end{aligned}\right\}. \tag{31}$$

In cooling regime, we have to follow variations of the effective (normalized) thermal conductivity $\kappa_e(\tau)$ to find the time when the lowest possible cooling temperature can be reached. $\kappa_e(\tau)$ depends on the time τ as follows

$$\kappa_e(\tau) = \kappa\left[1 + \frac{1}{2}\sum_{k=1}^{\infty} k\pi N_k e^{-A_k\tau}\right]. \tag{32}$$

It should be noted that $\kappa_e(\tau)$ in contrast to κ_e (26) does not use the factor μ_0^2 (27).

Next, as in the stationary steady state, the condition $\partial\dot{Q}_C / \partial J = 0$ for the current gives

$$J_{opt} = \frac{\alpha T_C}{\rho l} S = \frac{\alpha T_C}{r}. \tag{33}$$

Note that in contrast to the stationary steady state, the thermo conductivity $\kappa_e(\tau)$ (32) depends on the time τ, however, it does not affect the value of the optimal current J_{opt}.

The expression for the heat flux at the cold junction at the optimum current is equal to

$$\frac{1}{S}\dot{Q}_C = -\frac{1}{2}\frac{\alpha^2 T_C^2}{\rho l} + \frac{2T_0}{l}\kappa_e(\tau) \tag{34}$$

In the stationary steady state, the minimum cooling temperature $T_C^{\min}$ is found from the condition $\dot{Q}_C = 0$. In P-mode the condition $\dot{Q}_C = 0$ is only possible at certain times. Assuming $\dot{Q}_C = 0$ (34) we get

$$T_C^{\min} = 2\overline{T}\frac{\sqrt{1 + Z_e(\tau)\overline{T}} - 1}{Z_e(\tau)\overline{T}}, \tag{35}$$

where the renormalized figure of merit $Z_e(\tau) = \sigma\alpha^2 / \kappa_e(\tau)$ depends on the time τ.

The only difference between $T_C^{\min}(\tau)$ (35) and the expression for $T_C^{\min}$ in the stationary steady state is the value of figure of merit. The $T_C^{\min}(\tau)$ (35) uses the renormalized thermal conductivity $\kappa_e(\tau)$ which depends on the time τ and allows optimization of cooling temperature.

The $Z_e(\tau)$ maximum value, i.e. the minimum cooling temperature $T_C^{\min}$ corresponds to the minimum $T_C^{\min}$. As it follows from (32), $\kappa_e(\tau)$ has a minimum at $\tau = P/2$, however, even in this case $\kappa_e(\tau = P/2) > \kappa$ i.e. similar to *P*-mode power generation regime.

Due to the fact that $\kappa_e(\tau) > \kappa$, the coefficient of performance $K = \dot{Q}_C / \left(\dot{Q}_H - \dot{Q}_C\right)$ and the maximum cooling capacity $Q_C^{\max}$ are less than those in the stationary steady state, although at certain values of the thermo conductivity, the switching period and other TE conductor parameters are close to it.

The above conclusions apply only to *P*-mode. Further, we show that the TE device operating in *S*-mode can demonstrate a better performance.

3. Temperature distribution and heat flux in *S*-mode

3.1. The temperature distribution in *S*-mode

The solution of the equation (1) with the boundary conditions (4) for *S*-mode begins from representing $T(x,t)$ in the form

$$T(x,t) = \overline{T} - j_0^2 F\left(\sin 2\omega t - \mu^2\frac{a^2 - x^2}{a^2}\right) + \tilde{T}(x,t), \tag{36}$$

where

$$\mu^2 = a^2 \frac{\omega}{\chi}\ ,\ F = \frac{\rho}{4c_v \rho_0 \omega}. \tag{37}$$

Then (1) gives the equation for $\tilde{T}(x,t)$

$$\frac{\partial \tilde{T}}{\partial t} = \chi \frac{\partial^2 \tilde{T}}{\partial x^2} \tag{38}$$

and the boundary condition (4) becomes

$$\tilde{T}(x,t)\Big|_{x=\pm a} = \pm T_0 \sin(\omega t) + j_0^{\,2}\,\mathrm{F}\sin(2\omega t). \tag{39}$$

The solution of (38) with the boundary conditions can be found in the form

$$\tilde{T}(x,t) = T_0\left(S(x)\sin\omega t + C(x)\cos\omega t\right) + j_0^{\,2}\,\mathrm{F}\left(\tilde{S}(x)\sin 2\omega t + \tilde{C}(x)\cos 2\omega t\right), \tag{40}$$

where

$$\begin{cases} S(x) = S_{cs}\,\mathrm{ch}\left(\frac{\mu}{\sqrt{2}a}x\right)\sin\left(\frac{\mu}{\sqrt{2}a}x\right) + S_{sc}\,\mathrm{sh}\left(\frac{\mu}{\sqrt{2}a}x\right)\cos\left(\frac{\mu}{\sqrt{2}a}x\right), \\ C(x) = S_{sc}\,\mathrm{ch}\left(\frac{\mu}{\sqrt{2}a}x\right)\sin\left(\frac{\mu}{\sqrt{2}a}x\right) - S_{cs}\,\mathrm{sh}\left(\frac{\mu}{\sqrt{2}a}x\right)\cos\left(\frac{\mu}{\sqrt{2}a}x\right), \\ \tilde{S}(x) = \tilde{S}_{cc}\,\mathrm{ch}\left(\frac{\mu}{a}x\right)\cos\left(\frac{\mu}{a}x\right) + \tilde{S}_{ss}\,\mathrm{sh}\left(\frac{\mu}{a}x\right)\sin\left(\frac{\mu}{a}x\right), \\ \tilde{C}(x) = -\tilde{S}_{ss}\,\mathrm{ch}\left(\frac{\mu}{a}x\right)\cos\left(\frac{\mu}{a}x\right) + \tilde{S}_{cc}\,\mathrm{sh}\left(\frac{\mu}{a}x\right)\sin\left(\frac{\mu}{a}x\right). \end{cases} \tag{41}$$

The boundary conditions (39) allow finding coefficients in (41):

$$S_{cs} = \frac{\mathrm{ch}(\mu/\sqrt{2})\sin(\mu/\sqrt{2})}{\mathrm{sh}^2(\mu/\sqrt{2}) + \sin^2(\mu/\sqrt{2})},\ S_{sc} = \frac{\mathrm{sh}(\mu/\sqrt{2})\cos(\mu/\sqrt{2})}{\mathrm{sh}^2(\mu/\sqrt{2}) + \sin^2(\mu/\sqrt{2})},$$
$$\tilde{S}_{ss} = \frac{\mathrm{sh}(\mu)\sin(\mu)}{\mathrm{ch}^2(\mu) - \sin^2(\mu)}, \qquad \tilde{S}_{cc} = \frac{\mathrm{ch}(\mu)\cos(\mu)}{\mathrm{ch}^2(\mu) - \sin^2(\mu)}. \tag{42}$$

Therefore, the solution of (1) with the boundary conditions (4) can be written as

$$T(x,t) = \overline{T} + T_0\left(S(x)\sin\omega t + C(x)\cos\omega t\right) + \\ + j_0^{\,2}\,\mathrm{F}\left(\sin 2\omega t + \mu^2\frac{a^2 - x^2}{a^2} + \tilde{S}(x)\sin 2\omega t + \tilde{C}(x)\cos 2\omega t\right). \tag{43}$$

The solution $T(x,t)$ (43) includes both the terms proportional to $\sin\omega t$, $\cos\omega t$ and those proportional to $\sin 2\omega t$, $\cos 2\omega t$ – double the frequency of the temperature change at the TE conductor ends (junctions). The terms in (43) with $\sin\omega t$ and $\cos\omega t$ owe their origin to the heat flux generated by the temperature difference at the TE conductor ends ($x = \pm a$), their amplitude is proportional to T_0. Such terms describe common temperature waves damping with the distance from TE conductor ends ($x = \pm a$). Parameter μ^2 is a combination of the frequency, the length and the thermal diffusivity of TE conductor which is similar to μ_0^2 in *P*-mode(27).

The double frequency terms $\sin 2\omega t$, $\cos 2\omega t$ in (43) are proportional to the square of the amplitude of the current density amplitude j_0^2. Those terms describe the heat flux, born by the heterogeneity of the temperature distribution due to the Joule heat.

In Fig 3 we present the temperature distribution in the TE conductor which has the same parameters as in Fig. 2 above, but used in *S*-mode.

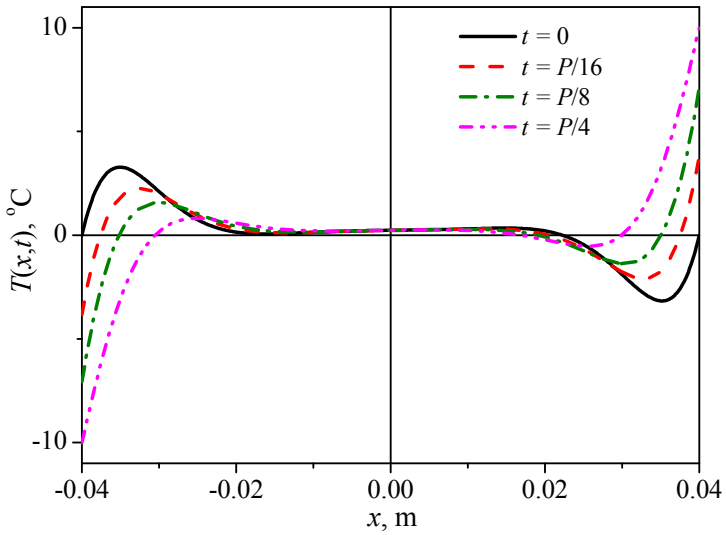

Fig. 3. Temperature distribution of TE conductor in S-mode at different times measured from the beginning of the period: $0...P/16$. External temperatures: $\bar{T} = 0\,°C$, $T_0 = 10\,°C$, TE conductor size $a = 0.04\ m$, TE material parameters $\kappa = 1.7\ W/mK$, $\chi = 1.2 \cdot 10^{-6}\ m^2/s$, current density amplitude $j = 0.1 \cdot 10^6\ A/m^2$ and rotation period $P = 1s$.

Fig. 3 shows that the temperature distribution of TE conductor in *S*-mode is similar to that for *P*-mode. But the temperature at the TE conductor edges in *S*-mode is changed continuously by sine wave in the range $\bar{T} \pm T_0$. In the center of the TE conductor $T(0,t) > \bar{T}$ because of the Joule heat emission.

3.2. Cooling in *S*-mode

Let during the first half-period the TE conductor has the lower end (junction) temperature (see Fig. 1*b*) colder than upper one, i.e. the lower junction is cold one.

Therefore, the heat flux at the cold junction $(x = -a)$ is

$$Q_C = -q_x S\big|_{x=-a} = S\kappa \frac{\partial T}{\partial x}\bigg|_{x=-a} - \alpha T_C(t) j(t) S\,, \tag{44}$$

where the second term is the Peltier heat flux, S is the cross section of TE conductor, $T_C(t) = T(x = -a, t)$.

Substituting in (44) the expression for the temperature distribution from (43) at $x = -a$ we obtain

$$\begin{aligned} \frac{Q_C}{S}\bigg|_{x=-a} &= \kappa T_0 \left(S'(-a)\sin\omega t + C'(-a)\cos\omega t \right) + \\ &+ \kappa j_0^{\,2}\,\mathrm{F}\left(-\frac{2\mu^2}{a} + \tilde{S}'(-a)\sin 2\omega t + \tilde{C}'(-a)\cos 2\omega t \right) - \alpha T_C(t) j(t), \end{aligned} \tag{45}$$

where S', C', S', C' are the derivatives with respect to coordinate at $x = -a$.

At the cold junction according to (4) the temperature will be minimal at $\omega t = \pi/2$. We denote it as T_c. At that moment the heat flux at the cold junction is

$$\frac{Q_C}{S}\bigg|_{\substack{x=-a \\ \omega t=\pi/2}} = \kappa T_0 S'(-a) - \kappa j_0^{\,2}\,\mathrm{F}\left(2\mu^2/a - \tilde{C}'(-a)\right) - \alpha T_C j_0\,. \tag{46}$$

To determine the lowest possible cooling temperature of the cold junction, we have to find the minimum of the heat flux at the cold junction i.e. $Q_C / S \left|_{\substack{x=-a \\ \omega t=\pi/2}}\right.$ as the function of current density amplitude j_0, then to find the optimal current j_0^{opt} we use the condition $\partial Q_C / \partial j_0 = 0$. Further, using j_0^{opt} we calculate the heat flux at the cold junction (46) and finally obtain the minimal cooling temperature $T_C^{\min}$.

The optimal current value j_0^{opt} is

$$j_0^{opt} = \frac{\alpha T_C}{2\mathrm{F}\kappa\left(2\mu^2 / a - \tilde{C}'(-a)\right)}. \tag{47}$$

At the minimal temperature $T_C^{\min}$ the heat flux Q_C of the cold junction at the current density amplitude j_0^{opt} to be equal to zero

$$\left.\frac{Q_C}{S}\right|_{\substack{x=-a \\ \omega t=\pi/2}} = \kappa T_0 S'(-a) - \frac{(\alpha T_C)^2}{4\mathrm{F}\kappa}\frac{1}{\left(2\mu^2 / a - \tilde{C}'(-a)\right)} = 0. \tag{48}$$

Using $T_0 = \overline{T} - T_C$ for (48) we find

$$T_C^2 = 2\overline{T}(\overline{T} - T_C)\left[\frac{2F\kappa^2}{\overline{T}\alpha^2 a^2}\left(2\mu^2 - a\tilde{C}'(-a)\right)aS'(-a)\right]. \tag{49}$$

Let us denote the term in square brackets in (49) $\beta(\mu, Z\overline{T}) / Z\overline{T}$ then using $2F\kappa^2 / \overline{T}\alpha^2 a^2 = 1/2Z\overline{T}\mu^2$ we write the following formulae for the dimensionless parameter $\beta(\mu)$

$$\begin{aligned}\beta(\mu) = \frac{\mu}{2\sqrt{2}}\left(1 + \frac{1}{2\mu}\frac{\mathrm{sh}(\mu)\mathrm{ch}(\mu) + \cos(\mu)\sin(\mu)}{\mathrm{ch}^2(\mu) - \sin^2(\mu)}\right)\times \\ \times \frac{\mathrm{sh}(\mu/\sqrt{2})\mathrm{ch}(\mu/\sqrt{2}) + \sin(\mu/\sqrt{2})\cos(\mu/\sqrt{2})}{\mathrm{sh}^2(\mu/\sqrt{2}) + \sin^2(\mu/\sqrt{2})}\end{aligned} \tag{50}$$

and the equation (49) is rewritten in the form

$$T_C^{\,2} + \frac{\beta(\mu)}{Z\overline{T}}\overline{T}T_C - \frac{\beta(\mu)}{Z\overline{T}}\overline{T}^2 = 0. \tag{51}$$

To calculate $T_C^{\min}$ we have to solve the quadratic equation (51), the positive root of (51) gives $T_c^{\min}$

$$T_C^{\min} = \frac{2\overline{T}}{1 + \sqrt{1 + \frac{Z\overline{T}}{\beta(\mu)}}}. \tag{52}$$

Let us compare $T_C^{\min}$ in *S*-mode to the minimal cooling temperature in the stationary steady state T_C^{st} that can be expressed [14] as follows

$$T_C^{st} = \frac{T_H}{\sqrt{1 + Z\overline{T}}}, \tag{53}$$

or using $T_H = 2\overline{T} - T_C$

$$T_C^{st} = \frac{2\overline{T}}{1 + \sqrt{1 + Z\overline{T}}}. \tag{54}$$

Relations (52) and (54) have the similar form that allows rewriting the expression for $T_c^{\min}$

$$T_C^{\min} = \frac{2\overline{T}}{1+\sqrt{1+Z_e\overline{T}}}, \tag{55}$$

where $Z_e\overline{T}$ is the renormalized figure of merit

$$Z_e\overline{T} = \frac{Z\overline{T}}{\beta(\mu)}. \tag{56}$$

Thus, *S*-mode calculations are also similar to the stationary steady state. As seen from (55) $T_C^{\min}$ is a monotonically increasing function of the dimensionless parameter $\beta(\mu)/Z\overline{T}$, at large values $\beta(\mu)/Z\overline{T} >> 1$ we obtain $T_C^{\min} \to \overline{T}$, that means no cooling at large $\beta(\mu)/Z\overline{T}$, i.e. the smaller the value $\beta(\mu)/Z\overline{T}$, the lower $T_C^{\min}$.

Also we can state that the higher TE figure of merit $Z\overline{T}$ means better cooling in *S*-mode (50) and opposite, when $Z\overline{T} \to 0$, $\beta(\mu)/Z\overline{T} \to \infty$ and the cooling is impossible. Further, note that (50) и (52) show that $T_C^{\min}$ depends only on the single dimensionless parameter – μ.

Let examine the ratio of minimal temperatures in *S*-mode and in the stationary steady state

$$\frac{T_C^{\min}}{T_C^{st}} = \frac{1+\sqrt{1+Z_e\overline{T}}}{1+\sqrt{1+Z\overline{T}}} = \frac{1+\sqrt{1+Z\overline{T}/\beta(\mu)}}{1+\sqrt{1+Z\overline{T}}}. \tag{57}$$

When the figure of merit $Z\overline{T}$ is fixed, the ratio (57) depends only on the single parameter $\beta(\mu)$. The function $\beta(\mu)$ has one minimum and it is invariant relative to $Z\overline{T}$. The minimum is at $\mu \approx 1.53$ and accordingly $\beta \approx 0.76 < 1$ i.e. the TE device in S-mode will deliver deeper cooling at certain times than in the stationary steady state (see Fig. 4).

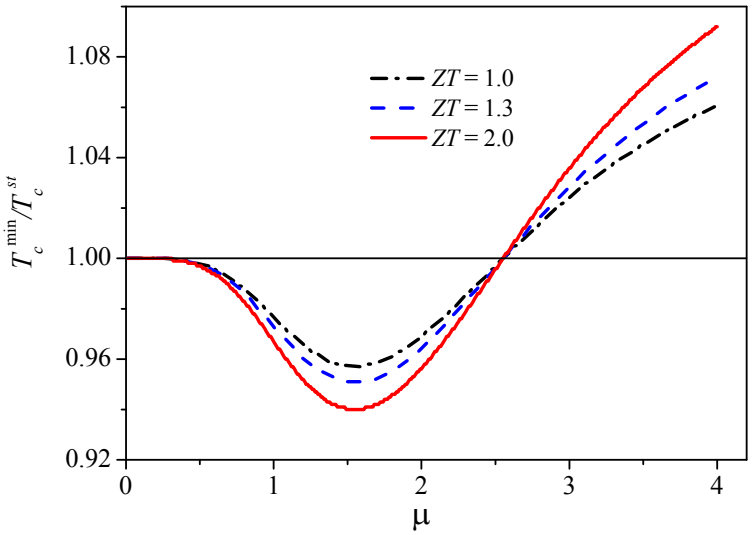

Fig. 4. Ratio of minimal temperatures T_c^{min}/T_c^{st} *for S-mode and stationary steady state on* μ *for* $Z\overline{T} = 1.0, 1.4, 2.0$.

As an example, for the TE device in *S*-mode with the TE conductor made of Bi_2Te_3 [34] (the temperature diffusivity $\chi \approx 1.2 \cdot 10^{-6}$ m^2/s) we choose the length of the TE conductor $2a = 1.5$ mm and the rotation period $P \approx 1.15$ s that gives optimal $\mu_{\min} \approx 1.53$.

For TE device operating in *S*-mode with the above parameters, we calculated $T(x,t)$, measured from the beginning of the period – Fig. 5.

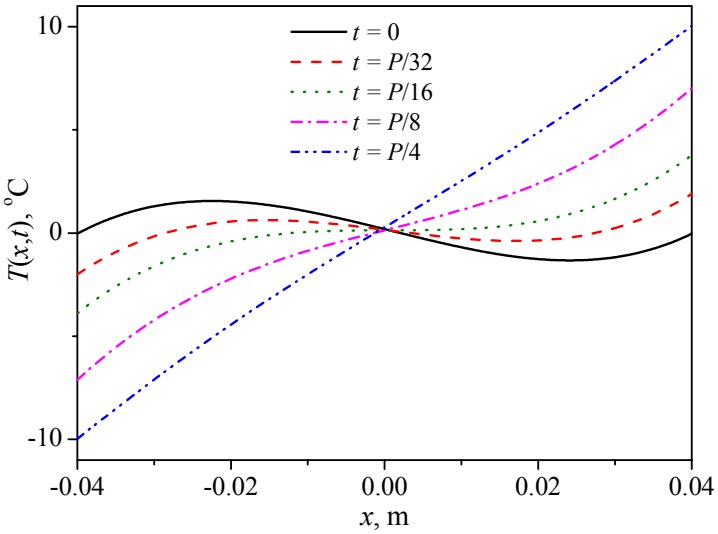

Fig. 5. Temperature distribution of TE conductor in S-mode at different times measured from the beginning of the period: $0...P/32$. *External temperatures:* $\overline{T} = 0°C$, $T_0 = 10°C$, *TE material dimensionless parameter* $\mu_{min} \approx 1.53$, *TE conductor size* $a = 0.04\,m$.

Comparison of Fig. 3 and Fig. 5 shows that exactly at a critical value of the dimensional parameter equal to $\mu_{min} \approx 1.53$ the coordinate dependence of $T(x,t)$ at time moment $P/4$ becomes linear, the heat penetrates to the middle of the leg and, thus, its entire volume is fully operated.

For *S*-mode at optimal $\beta(\mu) \approx 0.76$ the minimal achievable cooling temperature can be expressed as

$$T_c^{\min} \approx \frac{2\overline{T}}{1+\sqrt{1+1.3Z\overline{T}}}. \tag{58}$$

In other words, using the TE material with $ZT = 1$ in S-mode, we get cooling as of material with $ZT = 1.3$ in the stationary steady state. The TE material with $ZT = 1.3$ in *S*-mode corresponds to $ZT = 1.7$ in the stationary steady state.

4. Discussion and conclusions

The paper describes two types of proposed TE device that operate in periodic steady state modes: *P*-mode – the switching periodic mode and *S*-mode – the continuous sinusoidal mode.

In common, the efficiency of TE device is related to the rate of entropy production or particularly to the volume integral of the divergence of the entropy flux density $\mathbf{s} = \mathbf{q}/T$, $B = \int_V div(\mathbf{s})dV$. Finally, the efficiency can be written in the form

$$\eta = \eta_c \frac{1}{1+\frac{BT_H}{A}}, \tag{59}$$

where A is the work performed by the TE power generator.

Thus, the higher entropy production rate, the lower the efficiency of TE device in the power generation regime. Transient regimes, having some additional spatial inhomogeneity of the temperature distribution, naturally lead to the additional entropy production B and, as a consequence, the efficiency has to be even lower.

But the relation (59) that binds the efficiency and the entropy production is derived for the stationary steady state. Therefore, to predict what could be the efficiency in transient, pulsed or periodic modes is almost impossible in advance. Generally, the article discusses the possible benefits of TE device usage in transient modes, particularly periodic modes.

S-mode was shown to demonstrate deeper cooling at certain times, as compared with the stationary steady state.

The proposed method to calculate analytically parameters of TE devices in periodic *P*- and *S*-modes for the power generation regime or the cooling regime can be generalized to even more complex timing modes. The analytical solution allows applying the optimization technique to find optimal TE device parameters.

Acknowledgments

Authors would like to express their great appreciation to Dr. L.N. Vikhor, Prof. S.Z. Sapozhnikov, and Prof. I.V. Andrianov for their valuable and constructive suggestions during development of this research work.

I.V.Bezsudnov was supported by the Government of the Russian Federation (Grant 074-U01).

Appendix A

Solution of thermal conductivity equation in *P* – mode

Here we cite a solution of temperature distribution problem (1) with the boundary conditions (2) in *P* – mode (see Fig. 1) using a standard method of separation of variables.

As above in the text of the paper, for thermoelement leg in time intervals from nP to $(n+1)P/2$, where P is a period, and $n = 0, 1, ...$ the lower end is cold, and the upper end is hot.

We assume, as before, $l = 2a$, and re-write the thermal conductivity equation (1), the boundary conditions (2), just as substitution of variables, made in (7) in coordinates $x = -a...a$.

Thermal conductivity equation

$$\frac{\partial T}{\partial t} = \chi \frac{\partial^2 T}{\partial x^2} + \frac{\rho}{c_V \rho_0} j^2, \tag{A1}$$

and the boundary conditions

$$T\big|_{x=\pm a} = \overline{T} + T_0 \theta(t). \tag{A2}$$

Substituting

$$T(x,t) = \overline{T} + \frac{\rho j^2}{\kappa}\left(a^2 - x^2\right) + \tilde{T}(x,t), \tag{A3}$$

we obtain

$$\frac{\partial \tilde{T}}{\partial t} = \chi \frac{\partial^2 \tilde{T}}{\partial t^2}, \tag{A4}$$

$$\tilde{T}(x,t)\big|_{x=\pm a} = T_0 \theta(t). \tag{A5}$$

Let us represent the solution of equation (A1) with the boundary conditions (A2) in the form

$$T(x,t)=\overline{T}+\frac{\rho j^2}{\kappa}\left(a^2-x^2\right)+\tilde{T}(x,t)=\overline{T}+\frac{\rho j^2}{\kappa}\left(a^2-x^2\right)+ T_0\sum_{n=1}^{\infty}b_n\left[S_n(x)\sin\left(\frac{2\pi}{P}nt\right)+C_n(x)\cos\left(\frac{2\pi}{P}nt\right)\right], \tag{A6}$$

where

$$C_n(x)=\frac{1}{\Omega_n}\left[B_n\,\mathrm{ch}(\lambda_n x)\sin(\lambda_n x)-A_n\,\mathrm{sh}(\lambda_n x)\cos(\lambda_n x)\right],$$
$$S_n(x)=\frac{1}{\Omega_n}\left[A_n\,\mathrm{ch}(\lambda_n x)\sin(\lambda_n x)+B_n\,\mathrm{sh}(\lambda_n x)\cos(\lambda_n x)\right],\quad \lambda_n=\sqrt{n\pi/\chi P}. \tag{A7}$$

Coefficients A_n, B_n and Ω_n are as follows

$$A_n=\mathrm{ch}(\lambda_n a)\sin(\lambda_n a),\qquad B_n=\mathrm{sh}(\lambda_n a)\cos(\lambda_n a),\qquad \Omega_n=A_n^2+B_n^2, \tag{A8}$$

and b_n is coefficient of $\theta(t)$ expansion into a Fourier series.

$$\theta(t)=\sum_{n=1}^{\infty}b_n\sin\left(\frac{2\pi}{P}nt\right),\qquad b_n=\frac{2}{\pi n}\left[1-(-1)^n\right]. \tag{A9}$$

Fig. A1 shows a dependence of temperature $T(x,t)$ along the thermocouple length, obtained both by the Grinberg method [30] (TG), and by the method of separation of variables (TD) stated above. (Parameters of TE device correspond to those given in the paper).

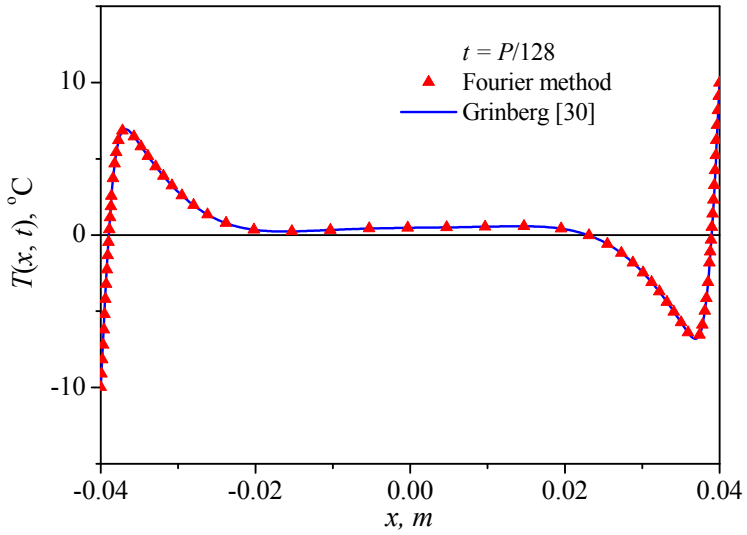

Fig. A1. As an example, temperature distribution along the thermocouple leg is given along thermocouple leg for time moment $t = P/128$, continuous line is solution by the Grinberg method [30], (19) triangles – by the method of separation of variables (A6).

As is evident from Fig. A1, temperature distribution $T(x,t)$ obtained by both methods – the method of separation of variables and the Grinberg method [30] practically coincide. For the calculation of the generation and cooling modules and for their optimization it is necessary to calculate heat fluxes, including the derivatives of temperature $\partial T/\partial x$ on the ends of thermocouple legs $x=\pm a$. For the solution obtained by the method of separation of variables such a derivative cannot be calculated, as long as for $x=\pm a$ formula (A9) gives a divergent series, whereas solution (19) obtained according to [30] at $x=\pm a$ converges, and the derivative can be calculated, see (20)-(22).

Fig. A2 shows a dependence of temperature $T(x,t)$ for different thermal diffusivity values. Coefficients λ_n are inversely proportional to thermal diffusivity (and, hence, thermal conductivity), thus, the higher λ_n, the deeper temperature variations will penetrate into a TE device leg.

Note that dependence 3 in Fig. A2 is given for thermal diffusivity value corresponding to the value of μ_0 (27) equal to 1.53, i.e. the one found in (56). Further thermal diffusivity increase does not change the form of dependence 3 in Fig. A2. With such thermal conductivity value heat fully comes to the middle of thermocouple leg, and the dependence $T(x,P/4)$ becomes fixed.

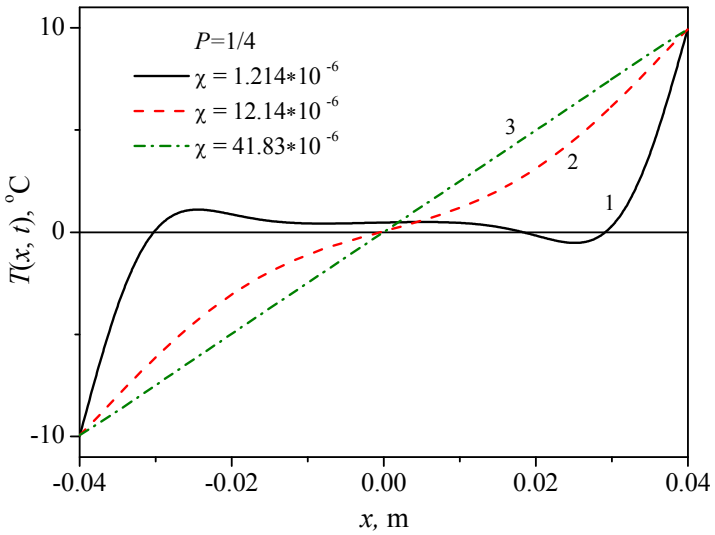

Fig. A2. Temperature distribution at time moment $P/4$ along thermoelement leg at different thermal diffusivity values 1 – $\chi = 1.214 \cdot 10^{-6}\, m^2/s$, 2– $\chi = 12.14 \cdot 10^{-6}\, m^2/s$, 3 – $\chi = 4.183 \cdot 10^{-5}\, m^2/s$.

Fig. A3 gives dependences $T(x,t)$ and $\partial T/\partial x$ at different time points. To calculate the derivative, the solution by the Grinberg method was used [30].

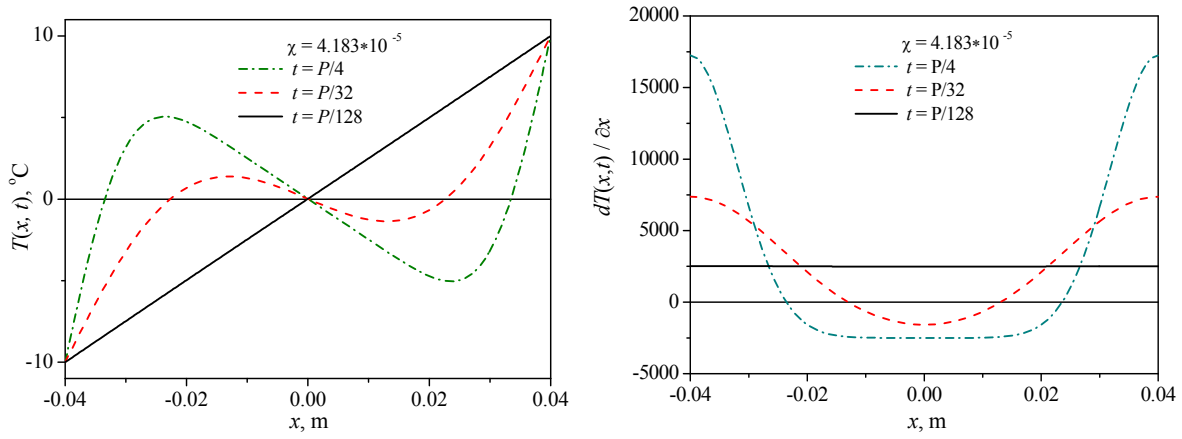

Fig. A3. Dependences of temperature T(x,t) (a) and temperature gradient $\partial T/\partial x$ (b) at time points $P/128$, $P/32$, $P/4$ for $\chi = 4.183 \cdot 10^{-5}\, m^2/s$.

As is seen from Fig. A3, that part of heat flux which is due to temperature gradient $\partial T / \partial x$ ($q_x = -\kappa \cdot \partial T / \partial x + \Pi j_x$) in the middle of thermocouple leg, close to $x = 0$, is much less that the flux on the ends, where there are large heat fluxes entering the hot end and coming into the cold end. In so doing, due to smallness of $\partial T / \partial x\big|_{x=0}$ there is practically no through flux through thermocouple leg.

References

1. T. M. Tritt, *Annual Review of Materials Research*, **41**, 433 (2011).
2. G. J. Snyder, and Eric S. Toberer, *Nature Materials* **7**, 105 (2008).
3. G. S. Nolas, J. Poon, and M. Kanatzidis, *Materials Research Society Bulletin*, **31**, 199 (2006).
4. H. Alam, S. Ramakrishna, *Nano Energy* **2**, 190 (2013).
5. G.S. Nolas, J. Sharp, and J. Goldsmid, *Thermoelectrics. Basic Principles and New Materials Developments*, Springer Series in Materials Science **45-VIII** (Springer-Verlag, Berlin, 2001), p.293.
6. X.F. Zheng, C.X. Liu, Y.Y. Yan, and Q. Wang, *Renewable and Sustainable Energy Reviews* **32,** 486 (2014).
7. *New Materials for Thermoelectric Applications: Theory and Experiment*, NATO Science for Peace and Security Series B: Physics and Biophysics, edited by V. Zlatic and A. Hewson (Springer, New York, 2013) p.273.
8. Properties and Applications of Thermoelectric Materials. The Search for New Materials for Thermoelectric Devices. *Proceedings of the NATO Advanced Research Workshop on Properties and Application of Thermoelectric Materials*, Hvar, Croatia, 21-26 September 2008, edited by V. Zlatic and A. Hewson, NATO Science for Peace and Security Series B: Physics and Biophysics (Springer, New York, 2009), p.340.
9. *Thermoelectric Nanomaterials Materials Design and Applications*. Springer Series in Materials Science, **182-XIX**, edited by K. Koumoto, T. Mori, (Springer, New York, 2013), p.387.
10. L. Weishu, Y. Xiao, C. Gang, and R. Zhifeng, *Nano Energy* **1**, 42 (2012).
11. L. P. Bulat, I. A. Drabkin, V. V. Karatayev V. B. Osvenskii, Yu. N. Parkhomenko, D. A. Pshenay-Severin, and A. I. Sorokin, *Journal of Electronic Materials*, **43**, 2121 (2014).
12. L. P. Bulat, V. B. Osvenskii, and D. A. Pshenai-Severin, *Physics of the Solid State*, **55**, 2442 (2013).
13. A. Snarskii, A. K. Sarychev, I. V. Bezsudnov, and A. N. Lagarkov, *Semiconductors*, 46, 659 (2012).
14. H. J. Goldsmid, *Introduction to Thermoelectricity*, Springer Series in Materials Science, **121**, (Springer, Berlin, 2009), p. 242.
15. Q. Zhou, Z. Bian, and A Shakouri, *J. Phys. D: Appl. Phys*. **40**, 4376 (2007).
16. G. J. Snyder, J.-P. Fleurial, T. Caillat, R. Yang, and G. Chen, *J. Appl. Phys*., **92**, 1564, (2002).
17. Yu. I. Dudarev, M. Z. Maksimov, *Technical Physics*, **43**, 737 (1998).
18. Chakraborty, K. C. Ng, *International Journal of Heat and Mass Transfer*, **49**, 1845 (2006).
19. R. Yanga, G. Chena, A. R. Kumarb, G. J. Snyder, and J.-P. Fleurial, *Energy Conversion and Management*, **46**, 1407 (2005).
20. J. N. Mao, H. X. Chen, H. Jia, and X.L. Qian, *Journal of Applied Physics*, **112**, 014514 (2012).
21. L. S. Stilbans, N. A. Fedorovich, *Sov. Phys.—Tech. Phys*. **3,** 460 (1958).
22. J. E. Parrott, *Solid State Electron*. **1,** 135 (1960).

23. V. A. Naer, *Journal of Engineering Physics*, **8**, 340 (1965).
24. E.K. Iordanishvili, *Thermoelectric Power Sources*, (Publ. Sov. Radio, Moscow, 1968), p.110
25. G. J. Snyder, J. P. Fleurial, T. Caillat, R. Yang, and G. Chen, *J. Appl. Phys*. **92,** 1564 (2002).
26. G. E. Hoyos, K. R. Rao, and D. Jerger, *Energy Convers*. **17,** 45 (1977).
27. K. Landecker, A.W. Findlay, *Solid State Electron*. **3,** 239 (1961).
28. T. Thonhauser, G.D. Mahan, L. Zikatanov, and J. Roe, *Appl. Phys*. Lett. **85,** 3247 (2004).
29. R. L. Field, H. A. Blum, *Energy Conversion*, **19-3**, 159 (1979).
30. G. A. Grinberg, *Selected Problems of Mathematical Theory of Electric and Magnetic Phenomena*. (Publ, Ac. of Sci. USSR, Moscow, 1948), p. 727.
31. R. Haberman, *Elementary Applied Partial Differential Equations with Fourier Series and Boundary Value Problems* (Englewood Cliffs, NJ: Prentice-Hall, 1998) p 215.
32. D. Zwillinger, Handbook of Differential Equations (3rd edition), (Academic Press, Boston, 1997) p.828.
33. D. Polyanin, V. F. Zaitsev, Handbook of Exact Solutions for Ordinary Differential Equations (2nd edition), (Chapman & Hall/CRC Press, Boca Raton, 2003), p.816.
34. Thermoelectrics Handbook. Macro to Nano, edited by D.M. Rowe (CRC Press, 2005) p.1014.

Submitted 11.09.14

M.O.Haluschak[1], O.S.Krynytsky[1], D.M.Freik[2]

[1]Ivano-Frankivsk National Technical University of Oil and Gas,
15, Karpatska Str., Ivano-Frankivsk, 76001, Ukraine;
[2]Institute of Physics and Chemistry, Vasyl Stefanyk Precarpathian National University,
57, Shevchenko St., Ivano-Frankivsk, 76018, Ukraine

THERMOELECTRICITY OF SOLID SOLUTIONS BASED ON LEAD TELLURIDE

A review of works dealing with the problems of obtaining and research on a set of thermoelectric properties of solid solutions based on lead telluride and chalcogenide compounds of other periodic table elements holding good prospects for medium temperature range (500-850) K is made. Chemical compositions, processing factors and temperature ranges whereby the materials have optimal parameters, namely the electric conductivity (σ), the Seebeck coefficient (S), the thermal conductivity (χ), as well as the specific thermoelectric power ($S^2\sigma$), the thermoelectric figure of merit ($Z= S^2\sigma/\chi$) and the dimensionless thermoelectric figure of merit (ZT) are indicated.

Key words: thermoelectric device, periodic steady state, figure of merit, power generation, cooling

Introduction

Possibilities of direct thermal into electric energy conversion have long attracted the attention of researchers and developers of various kinds of equipment. In recent years, thermoelectric effects have found expanding applications. On their basis, thermoelectric generators unique in their parameters have been created that are used in space, under water and in terrestrial (hard-to-reach for service) equipment; generators with nuclear heat sources have been designed. Thermoelectric cooling finds ever-widening application as well. Small overall dimensions, practically unlimited operational life, high reliability of thermoelectric coolers are decisive for their use in instrument making, electronics, medicine and biology [1]. Moreover, in recent years the problem of improving the efficiency of thermal into electric energy conversion has assumed particular prominence due to lack of fossil fuels and considerable discharge to the atmosphere of a large amount of deleterious gases that contaminate the environment, destruct the ozone layer and cause global climate changes [1].

The efficiency of using thermoelectric material is primarily determined by its capability of reaching high values of thermoelectric figure of merit Z ($Z = S^2\sigma/\chi$, where S is the Seebeck coefficient, σ is the electric conductivity, χ is the thermal conductivity) [2].

Most of materials based on IV-VI compounds possess high melting points and combine a set of properties that make them suitable for practical application. Thus, for instance, alloys based on *PbTe*, containing $AgSbTe_2$, have high values of $ZT > 1$ both for *n*- and *p*-type [3, 4]. With the advent of modern methods of synthesis and processing, as well as methods for the analysis of microstructure and chemical composition, these materials again became a subject for active studies. The greatest advances in this area have been achieved with the implementation of solid solutions based on *PbTe* with low thermal conductivity coefficients.

This review is an attempt of demonstrating some results of new investigations of *PbTe* based materials.

I. *PbTe-Ag$_2$Te* system alloys

The composite $(PbTe)_{50-x}(Ag_2Te)_{2x/3}$ with x = 0, 1, 2, 3 and 4 (corresponding to *Pb* content 50, 49, 48, 47 and 46 at. %) was obtained as follows [5]. A mixture of *Pb*, *Ag* and *Te* elements of purity 99,999 % or higher was loaded into a quartz ampoule evacuated to $1.33 \cdot 10^{-3}$ Pa and sealed. Then the ampoule was heated to 1273 K (point 1 in Fig. 1) in a vertical programmable tube furnace at a rate of 500 K/h. After holding at this temperature for 6 hours, the ampoule was cooled and then annealed at 973 K (the first annealing, point 2 in Fig. 1) for 2 days with quenching in water. To obtain a homogeneous solid solution, the ampoule was again annealed (second annealing, point 3 in Fig. 1) at 773 K for 3 days.

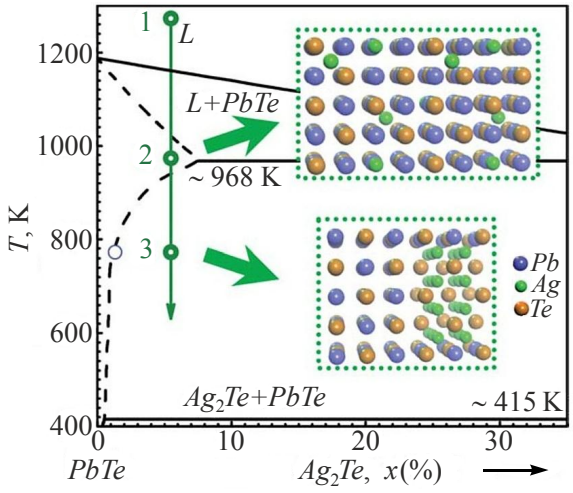

Fig. 1. Phase diagram of PbTe-Ag$_2$Te system and procedures of thermoelectric material preparation [7].

The resulting ingots were crushed and compacted by hot pressing at 700 K for an hour. The samples thus obtained were used as a source material for doping with *Na* of *PbTe*:*Na*/*Ag$_2$Te* alloy. The nominal concentration of *Na* corresponded to composition $[(Na_xPbTe_{1+x})_{0.945}(Ag_2Te)_{0.055}]$ with x = 0…3%. The low-temperature annealing results in *Ag$_2$Te* precipitation in the supersaturated alloy phase. Low thermal conductivity of *PbTe*:*Na*/*Ag$_2$Te* lattice due to the use of *Ag$_2$Te* nanoinclusions and excellent electronic properties to complex structure of valence zone result in $ZT > 1.5$ at high temperatures [5]. Moreover, there are considerable improvements of the average value of *ZT* and thermoelectric figure of merit in the entire temperature range, as compared to similar materials without nanostructures and a complex band structure or with small nanostructures.

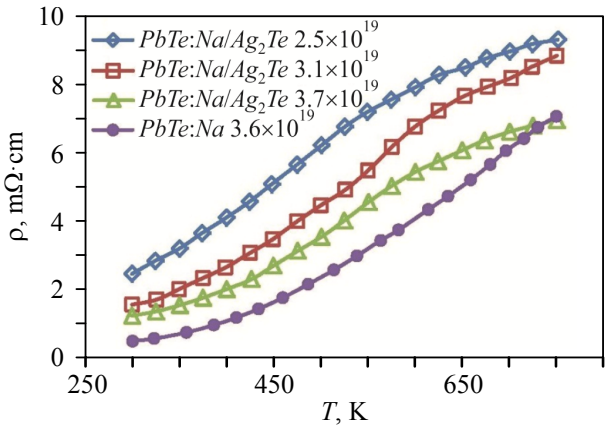

Fig. 2. Temperature dependence of electric resistance for PbTe:Na/Ag2Te and PbTe:Na [5].

The electric resistivity of *PbTe*:*Na*/Ag_2Te nanocomposites is higher than in *PbTe*:*Na* (Fig. 2) at low temperatures, when doping levels are almost the same ($p_H = 3.6 \cdot 10^{19}$ cm^{-3} for *PbTe*:*Na* against $p_H = 3.7 \cdot 10^{19}$ cm^{-3} for *PbTe*:*Na*/Ag_2Te). Similar to *PbTe*:*Na* and (*n-PbTe*), the electric resistivity (ρ) grows faster than is commonly expected for a system with a dominant acoustic scattering ($\rho \propto T^{l\sim1.5}$).

The thermal conductivity (χ) is reduced approximately by 50% in the entire measured temperature range due to Ag_2Te nanoinclusions (Fig. 3). The observed reduction of χ is only partly due to the presence of nanoinclusions. The electric conductivity is reduced, hence the electron component of thermal conductivity (χ_E) is reduced, contributing to reduction of χ.

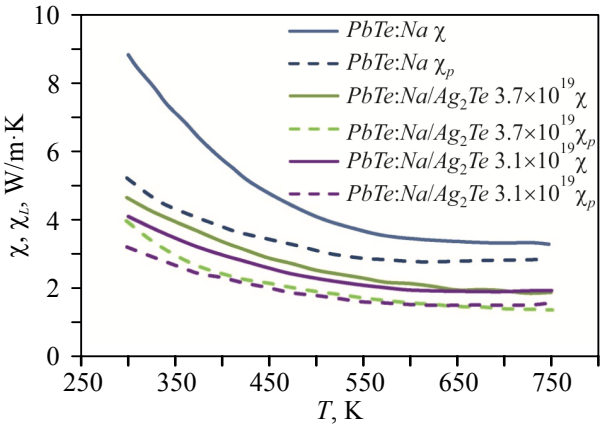

Fig. 3. Temperature dependences of total (χ) and lattice (χ_L) thermal conductivity for PbTe:Na/Ag_2Te alloy as compared to PbTe:Na [7].

II. *PbTe*-Sb_2Te_3 solid solutions

In order to obtain *PbTe*-Sb_2Te_3 solid solutions based on lead telluride (Fig. 4), at first *PbTe* and Sb_2Te_3 compounds were synthesized with the use of lead, tellurium and antimony elements that were loaded into evacuated quartz ampoule and placed into a furnace heated to melting point for 1 hour [6,7].

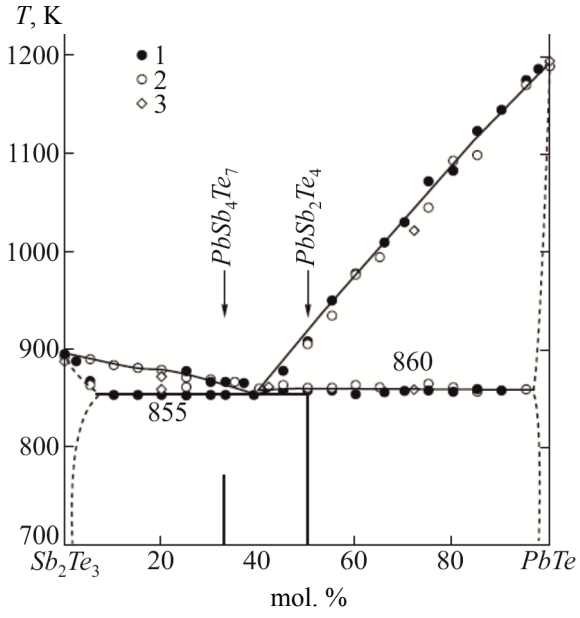

Fig. 4. Phase diagram of PbTe-Sb_2Te_3 system [8].

Following that, the obtained alloys were mixed in proper stoichiometric ratio and loaded into evacuated quartz ampoules that were placed into a furnace and melted at 1250 K for 1 hour with subsequent cooling at a rate of 98 K/h (Fig. 4). The obtained ingots were used for measuring the thermoelectric properties (Fig. 5).

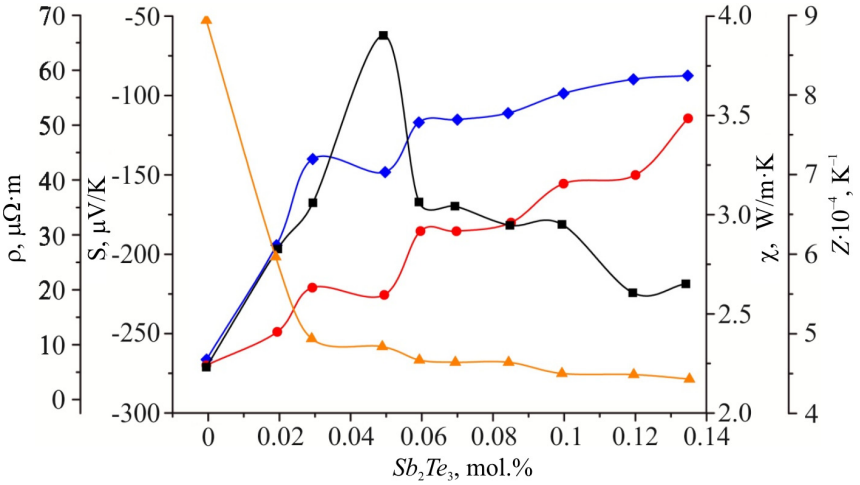

Fig. 5. Dependences of the electric resistivity (ρ – ▲), the Seebeck coefficient (S – ♦), the thermal conductivity (χ – ●), the figure of merit (Z – ■) $(PbTe)_{100-x}(Sb_2Te_3)_x$ on the content of x Sb_2Te_3 [9].

The electric resistivity for *PbTe* as a function of Sb_2Te_3 is first drastically decreased when the amount of Sb_2Te_3 is lower than 0.03 mol. %, and then slowly decreased with increase in Sb_2Te_3 content (Fig. 5 – ▲). The research results show that the type of impact of Sb_2Te_3 as a doping impurity varies due to high pressure and at high temperature [9].

The Seebeck coefficient indicates that all the samples are *n*-type semiconductors (Fig.5 – ♦).

Similar to other doping impurities, total thermal conductivity is increased with increase in Sb_2Te_3 content (Fig. 5 – ●). In so doing, the electron thermal conductivity is increased quickly, and lattice thermal conductivity is continuously reduced with increase in Sb_2Te_3 content for doping with 0.135 mol. % Sb_2Te_3. A reduction in total thermal conductivity as compared to pure *PbTe* is mainly due to a reduction in lattice thermal conductivity, which may be caused by the following factors: atom and ion impurities related to Sb_2Te_3 have a large atomic number which has a greater impact on phonon scattering as compared to other doping impurities; due to effect caused by "softening" of phonons that also reduce lattice thermal conductivity [9].

The thermoelectric figure of merit *Z* for *PbTe* doped with Sb_2Te_3, calculated from the measured values, is increased and then slowly decreased with increase in Sb_2Te_3 content (Fig.5 – ■). In particular, this figure of merit parameter at room temperature has maximum value ~ 8.7×10^{-4}/K which is about several times higher than in *PbTe* samples doped with *PbI* (2.4×10^{-4}/K) and (2.3×10^{-4}/K) with grain size 0.5 and 0.7 μm, respectively [11].

III. *PbTe-Bi_2Te_3* solid solutions

To obtain *PbTe-*Bi_2Te_3 solid solutions based on lead telluride, at first *PbTe* and Bi_2Te_3 compounds were synthesized from the elements of lead, tellurium and bismuth that were loaded into evacuated quartz ampoule and placed into a furnace heated to melting temperature for 1 hour. Following that, the resulting compounds were mixed in proper stoichiometric ratio and loaded into evacuated quartz ampoules that were placed into furnace and melted at 1250 K for 1 hour with

subsequent cooling at a rate of 98 K/h. The resulting ingots were used for measuring the thermoelectric properties (Fig. 7) [14].

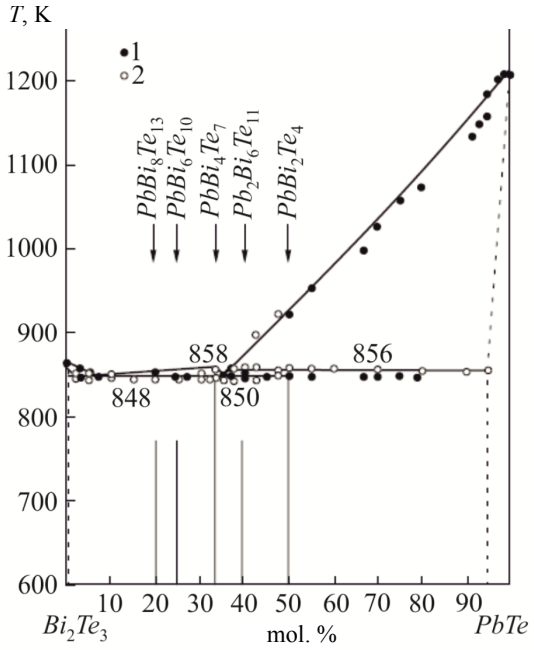

Fig. 6. Phase diagram of PbTe-Bi_2Te_3 system [8].

For $(PbTe)_{100-x}(Bi_2Te_3)_x$ solid solutions (Fig.7 – ▲) it is seen that the electric resistivity is drastically increased at $x \leq 0.3$ and more slowly at $x \geq 0.3$. As compared to the results for Sb_2Te_3 as doping impurity [10], the electric resistivity of *PbTe* is less sensitive to doping impurity Bi_2Te_3. The difference of electric resistivity from the composition can be due to different ionic radii of these atoms. The ionic radii of *Pb*, *Bi* and *Sb* are 1.26, 1.2 and 1.0 Å, respectively [11]. The difference between the ionic radii of *Pb* and *Sb* is greater than between *Pb* and *Bi*, so chemical internal stress as a result of *Sb* substitution for *Pb* is higher than *Bi* substitution for *Pb* with the same concentration of impurity atoms. Moreover, chemical internal stresses should grow with impurity increase.

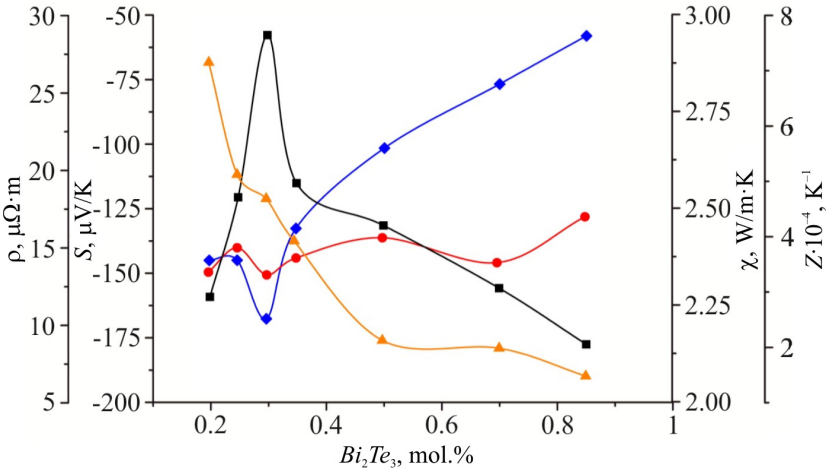

Fig. 7. Dependences of the resistivity (ρ – ▲), the Seebeck coefficient (S – ♦), the thermal conductivity (χ – ●), the figure of merit (Z – ■) $(PbTe)_{100-x}(Bi_2Te_3)_x$ on the content of x Bi_2Te_3 [14].

From the dependence of the Seebeck coefficient on the content of *x* (Fig.7 – ♦) it is seen that all $(PbTe)_{100-x}(Bi_2Te_3)_x$ samples have *n*-type conductivity. The Seebeck coefficient in its absolute value is

almost unchanged at $x \leq 0.3$ and has sharp maximum at $x = 0.3$, and then is reduced at $x \geq 0.35$ with increase in x (Fig.7 – ♦). Sharp maxima of the Seebeck coefficient observed for $(PbTe)_{100-x}(Bi_2Te_3)_x$ resemble a behaviour that takes place for metals, intermetallic compounds and heavily doped semiconductors [14]. This is due to the energy dependence on the density of electron states close to the Fermi energy [14].

Total thermal conductivity coefficient χ is retained almost constant and is ~ 2.30 W/K·m (Fig. 7 – ■) which is in agreement with the literature data [15]. Lattice thermal conductivity is linearly reduced, whereas carrier thermal conductivity is linearly increased with increase in x. These results show that thermal conductivity coefficient of $(PbTe)_{100-x}(Bi_2Te_3)_x$, is mainly lattice. Different values of lattice thermal conductivity for *PbTe* doped with Bi_2Te_3 and Sb_2Te_3 also can be due to different ion radii of *Bi* and *Sb* which results in greater crystal lattice deformation and increased phonon scattering. This can be mainly responsible for the fact that lattice thermal conductivity is reduced. Moreover, effect of phonon scattering of heavy impurity atoms should be stronger compared to lighter impurity atoms, so lattice thermal conductivity is much lower than in *PbTe* which is contained in other doping impurities with small grain size [9].

Thermoelectric figure of merit Z for $(PbTe)_{100-x}(Bi_2Te_3)_x$ samples at room temperature first is increased and then decreased with increase in x (рис.7 – ■). In particular, at room temperature maximum Z_{max} value is 7.63×10^{-4} K^{-1} which is several fold greater than the literature data for *PbTe* samples doped with PbI_2 with small grain size [9]. The resulting high Z value is attributable to considerable Seebeck coefficient and low thermal conductivity. The Seebeck coefficient value 167.2 μV/K at $x = 0.3$ is due to electron topological transition as a result of doping Bi_2Te_3 with high mobility (1212 V·cm^2/s).

IV. *PbTe-PbS* solid solutions

Samples of *PbTe-PbS* system (Fig. 8) with *PbS* content (4, 8, 16, 30, 50 mol. %) were synthesized using *PbTe* and *PbS* as the source materials that were obtained from high-purity elements (*Pb*, *Te* and *S*) whose ratio corresponded to stoichiometric content of *PbTe* and *PbS*. Synthesis took place in evacuated to $1.33\cdot10^{-2}$ Pa quartz ampoules at a temperature of 1373 K. The samples were turned over several times in liquid state and cooled to room temperature [16].

PbTe-PbS solid solutions with 8 mol.% *PbS* are unique in that they can be obtained in two forms, namely solid solution and nanostructured material. Fig. 9 shows TEM image of *PbTe-PbS* solid solution (8% mol.% *PbS*) prepared by melt quenching. Single-phase solid solution was then heated to high temperature of two-phase region of pseudo-binary phase diagram [19] where nucleation and

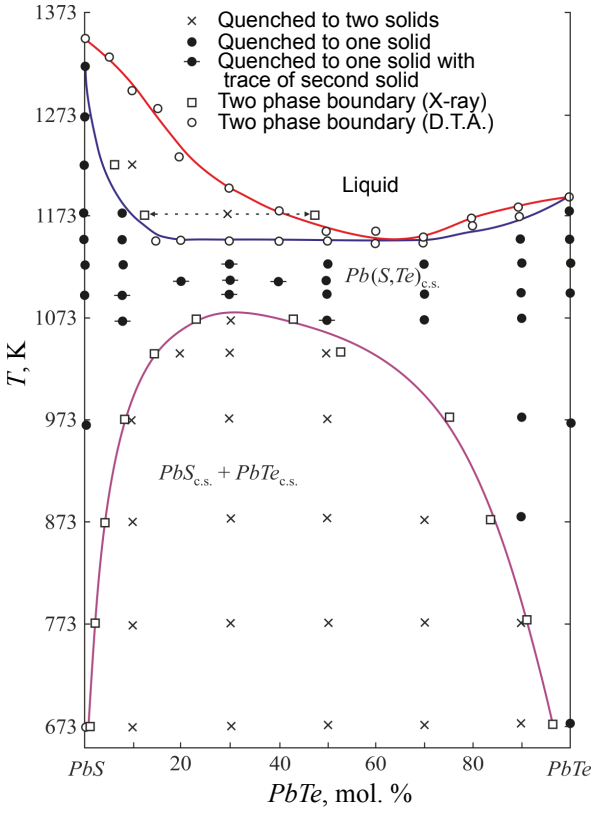

Fig. 8. Phase diagram of PbTe-PbS system [17].

particle growth occurs between 400 K and 500 K. This creates thermodynamically stable nanosize *PbS* particles settling in *PbTe* matrix. At settling of *PbS* nanoparticles, the electron and thermal transport undergo considerable changes [19]. Increase in electron mobility, as well as carrier concentration testify to reduction of electron scattering on the ionized impurities. Formation of thermodynamically stable and sequential *PbS* nanostructures contributes to lattice thermal conductivity decrease by 60% (Fig. 9) [20]. This confirms that nanosize particles in the bulk thermoelectric materials are extremely efficient in reducing lattice thermal conductivity, thus contributing to thermoelectric power increase [20].

In *PbTe-PbS* system, apart from nucleation and growth processes, there is spinodal decomposition which is another ideal mechanism of phonon scattering by nanoparticles on phase boundaries [21]. Hence, the composition and structure, as well as the size and distribution of nanoinclusions, can be controlled due to rational choice of cooling rate and thermal treatment after sysnthesis.

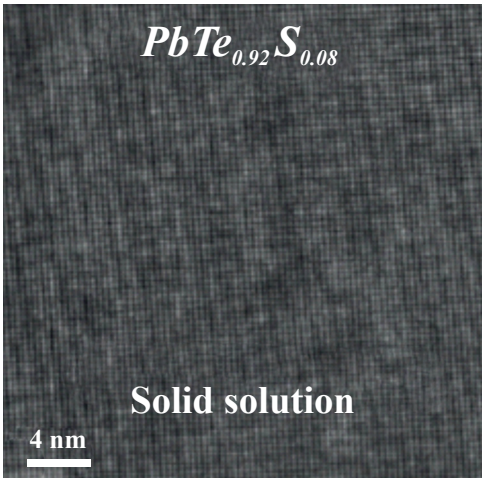

a)

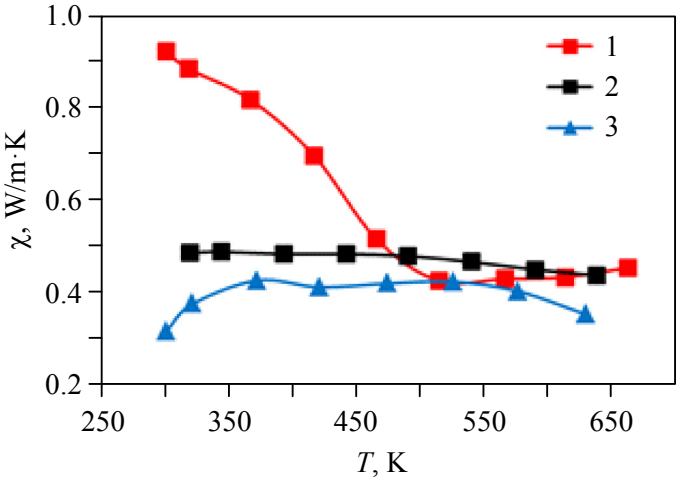

b)

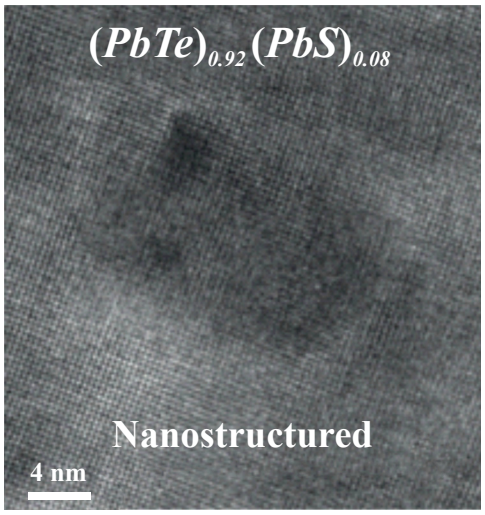

c)

Fig. 9. Temperature dependence of lattice thermal conductivity for samples of PbTe-PbS solid solution (8 mol.% PbS): a, c – TEM result, b – thermal conductivity: first heating (1); cooling after the first heating (2); after sample annealing (3) [18].

Three scale components have been revealed for *PbTe-PbS* system (30 mol.% *PbS*), namely point defects of solid solution (atomic scale), nanoparticles (nanodimensional) and semicoherent phase boundaries with regularly distributed misfit dislocations (Fig. 10) [21].

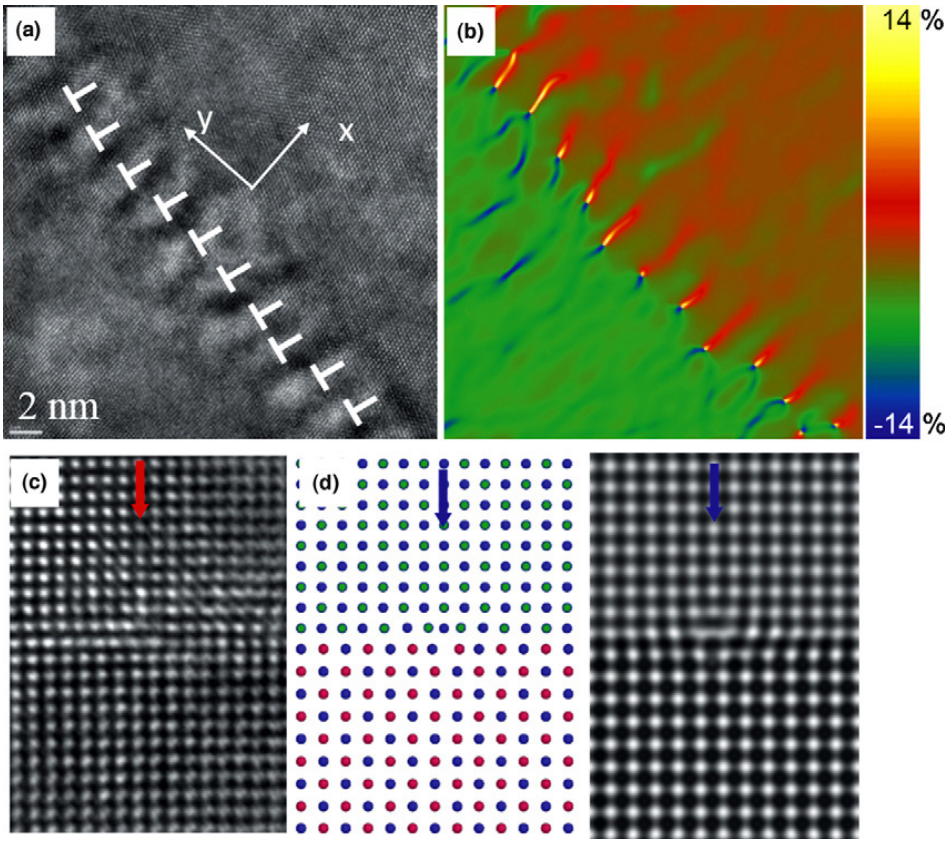

Fig. 10.
(a) – image of lattice of $PbTe_{0.7}S_{0.3}$ sample on one Moire fringe boundary;
(b) – image of dislocation centres (high intensity red lines);
(c) – image of lattice including one sharp centre of dislocation with the Burgers vector 1/2 [1 0 0];
(d) – atomic simulation of dislocations between PbTe/PbS [18].

V. *PbTe-PbS* solid solutions doped with *Bi* and *Sb*

Material was prepared from *Pb*, *Bi*, *Te* and *S* (*Pb*, *Sb*, *Te* and *S*) elements with purity 99.99% mixed in a proper molar ratio in quartz tubes and sealed in vacuum $3 \cdot 10^{-3}$ Pa [22]. Later on the samples were heated to 1273 K for 12 hours and quickly cooled to 873 K and held for another 72 hours, following which they were quenched in liquid nitrogen. The samples were made in a ball planetary mill and compacted by spark plasma sintering (SPS) at 853 K for 5 minutes under pressure of 50 MPa.

Thermoelectric properties and figure of merit of *Bi*-doped $(Bi_xPb_{1-x}Te)_{0.88}(PbS)_{0.12}$ samples with $x = 0$, 0.001, 0.003, and 0.005 are shown in Fig. 11. The resistivity of all samples is increased with a rise in temperature over the entire measurement range. As is shown in Fig. 11, *a*, the undoped sample $(PbTe)_{0.88}(PbS)_{0.12}$ has high electric resistivity from $1.98 \cdot 10^{-5}$ Ohm at 300 K and $1.37 \cdot 10^{-4}$ Ohm at 773 K [23]. It is apparently due to intergrain boundary resistance and considerable *PbS* content. Nevertheless, this results in evident increase of the Seebeck coefficient and thermal conductivity reduction. The electric resistance of *Bi*-doped samples is considerably reduced with increase in *Bi* content as compared the undoped sample.

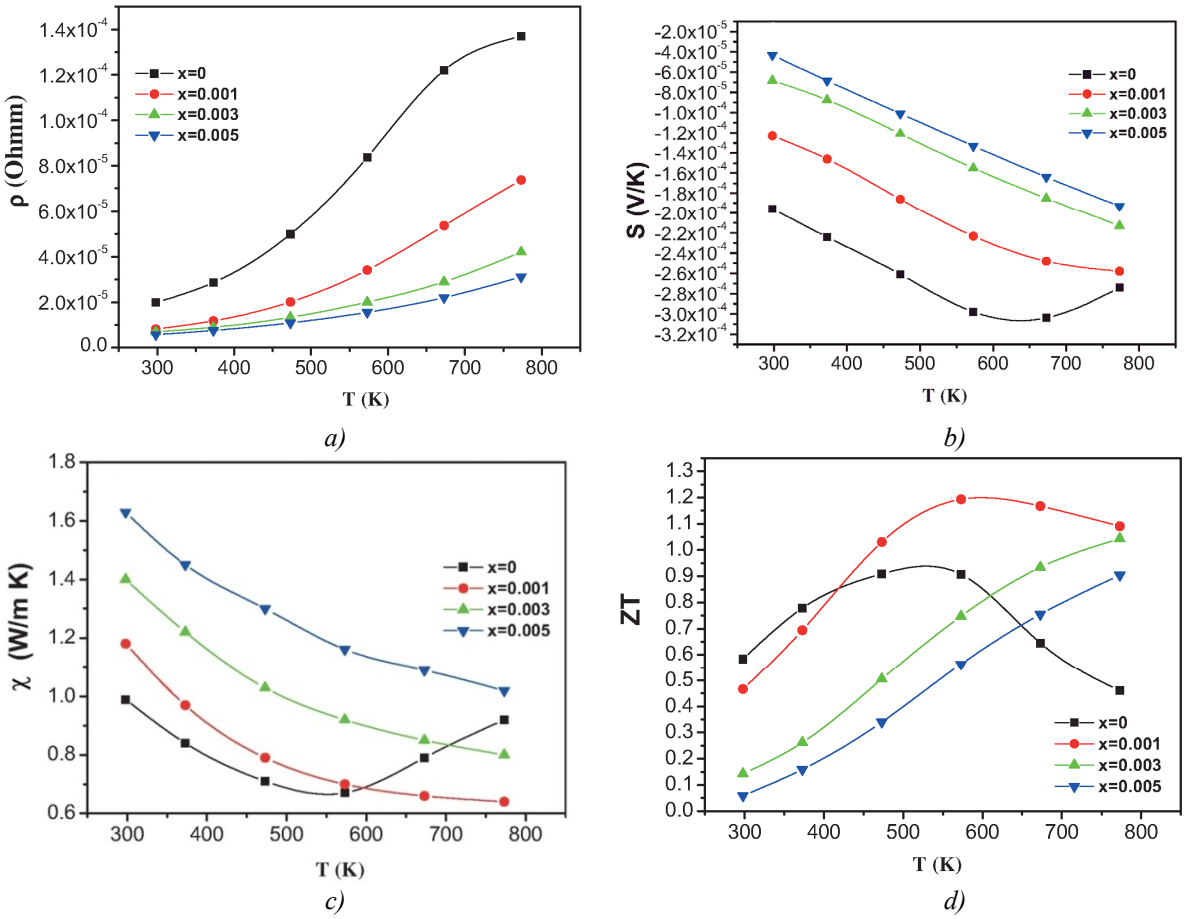

Fig. 11. Temperature dependences of the electric resistivity (ρ – a), the Seebeck coefficient (S – b), total thermal conductivity (χ – c), the value of ZT (d) for doped samples $(Bi_xPb_{1-x}Te)Bi_{0.88}(PbS)_{0.12}$ *(x = 0, 0.001, 0.003, 0.005) [22].*

The Seebeck coefficients of the investigated solid solutions are negative over the entire temperature range, which indicates to dominant *n*-type carriers (electrons) (Fig. 11, *b*). The absolute values of the Seebeck coefficients for all the samples are increased with a rise in temperature (Fig. 11, *b*).

Total thermal conductivity coefficients for the investigated samples $(Bi_xPb_{1-x}Te)_{0.88}(PbS)_{0.12}$ with x = 0, 0.001, 0.003 and 0.005 are shown in Fig. 11, *c*. Total thermal conductivity for the undoped sample $(PbTe)_{0.88}(PbS)_{0.12}$ is reduced from 0.99 to 0.67 W/m·K with a rise in temperature from 300 to 573 K, and is increased with a rise in temperature in the range of 573 to 773 K (Fig. 11, *c*). Increase in total thermal conductivity at high temperature can be related to increase in lattice thermal conductivity that dominates over total thermal conductivity for the undoped sample. Growing lattice thermal conductivity can be due to anharmonic phonon excitation or partial decomposition of nanostructures at high temperatures.

The figure of merit *ZT* for the investigated samples $(Bi_xPb_{1-x}Te)_{0.88}(PbS)_{0.12}$ with $x = 0$, 0.001, 0.003 and 0.005 over the entire temperature range is shown in Fig. 11, *d*. Sample $(Bi_xPb_{1-x}Te)_{0.88}(PbS)_{0.12}$ with $x = 0.001$ shows the highest $ZT = 1.20$ with 573 K, which is much higher than 0.91 for the undoped $(Bi_xPb_{1-x}Te)_{0.88}(PbS)_{0.12}$ at 473 K.

The electrical properties of synthesized and doped samples $(PbTe)_{0.88}(PbS)_{0.12}Sb_xPb_{1-x}Te_{0.88}S_{0.12}$ with $x = 0$; 0,002; 0,004; 0,006; 0,008 are given in Fig. 12. The resistivity of all samples is increased with a rise in temperature over the entire measured range. The resistivity of undoped sample

$(PbTe)_{0.88}(PbS)_{0.12}$, (Fig. 12, *a*) is rather high and varies from $1.98 \cdot 10^{-5}$ Ohm at 298 K to $1.37 \cdot 10^{-4}$ Ohm at 773 K. This is due to high resistance of intergrain boundaries and high content of *PbS* in a sample prepared by spark-plasma sintering. The resistivity of *Sb*-doped sample is reduced considerably with increase in *Sb* content as compared to undoped sample. Resistivity reduction of *Sb*-doped $(PbTe)_{0.88}(PbS)_{0.12}$ is attributable to substitution of Sb^{3+} ions for Pb^{2+} ions, since *Sb* is an efficient electron donor [24].

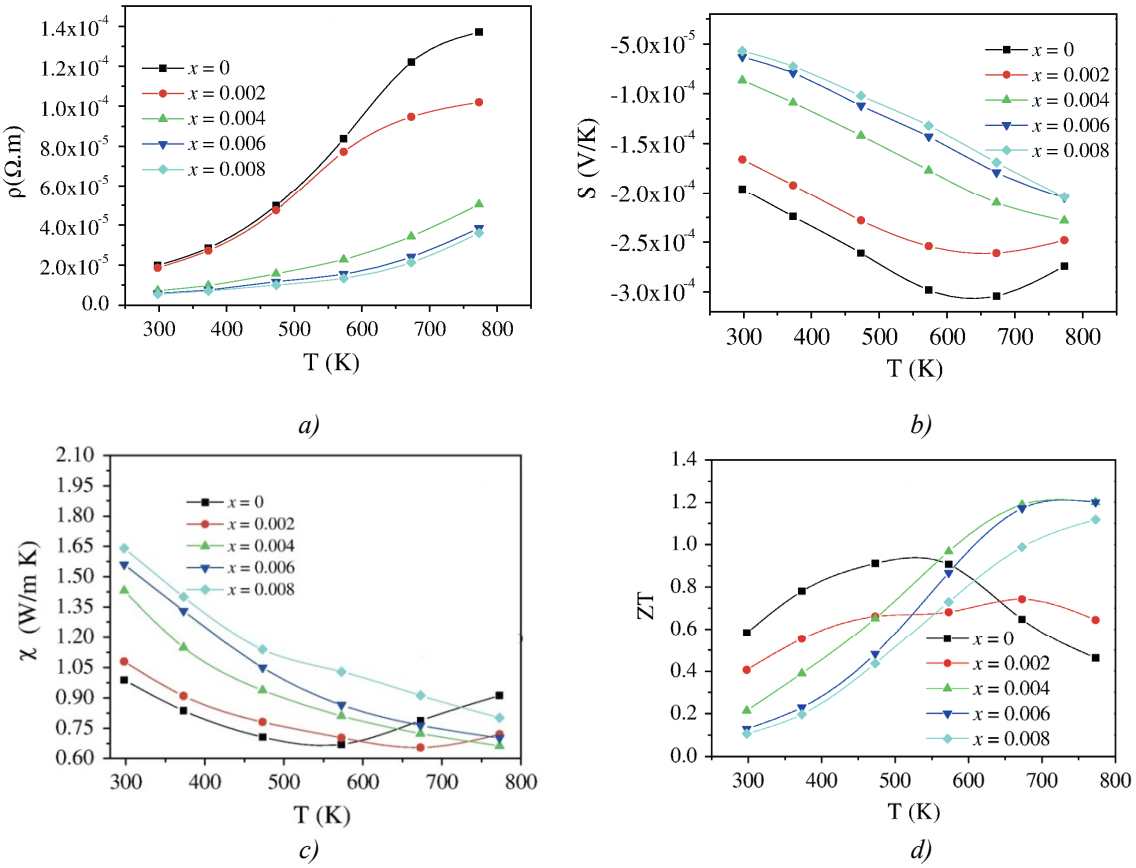

Fig. 12. Temperature dependences of the electric resistivity (ρ - a), the Seebeck coefficient (S - b), thermal conductivity (χ - c), the value of ZT (d) for doped samples $Sb_xPb_{1-x}Te_{0.88}S_{0.12}$ (x = 0, 0.002 0.004, 0.006 and 0.008) [25].

The Seebeck coefficients of investigated samples are represented in Fig. 12, *b*. They are negative over the entire temperature range, pointing to dominant *n*-type carriers (electrons). The absolute Seebeck coefficient for all the samples is increased with a rise in temperature. The absolute Seebeck coefficient for undoped sample $(PbTe)_{0.88}(PbS)_{0.12}$ is linearly increased from 196 μV/K at room temperature to 298 μV/K at 573 K, and then is slightly decreased. For doped *Sb* samples it is decreased with increasing *Sb* content from 196 μV/K with $x = 0$ to 57.0 μV/K with $x = 0.008$ at room temperature.

Total thermal conductivity coefficients for the investigated *Sb*-doped $(PbTe)_{0.88}(PbS)_{0.12}$ samples $Sb_xPb_{1-x}Te_{0.88}S_{0.12}$ with $x = 0$, 0.002, 0.004, 0.006, and 0.008, are shown in Fig. 12, *c*. Total thermal conductivity for the undoped sample $(PbTe)_{0.88}(PbS)_{0.12}$ made by SPS is reduced from 0.99 W/m·K to 0.67 W/m·K with a rise in temperature from 298 K to 573 K, and is slightly increased with a rise in temperature from 573 K to 773 K. Thermal conductivity of $Sb_xPb_{1-x}Te_{0.88}S_{0.12}$ is from 1.08W/m·K to 0.654 W/m·K with $x = 0.002$, from 1.43 W/m·K to 0.663 W/m·K with $x = 0.004$, from 1.56 W/m·K for

0.702 W/m·K, with $x = 0.006$, and from 1.64 W/m·K to 0.802 W/m·K with $x = 0.008$ in the temperature range from 298 K and 773 K. Low thermal conductivity coefficients are attributable to small grain size and grain boundaries that formed as a result of grinding in a ball mill. On doping of $(PbTe)_{0.88}(PbS)_{0.12}$ with *Sb*, total thermal conductivity is increased mainly due to increase in electron concentration through *Sb*. The sample of $Sb_xPb_{1-x}Te_{0.88}S_{0.12}$ with $x = 0.004$ shows the highest figure of merit *ZT* 1.20 at 773 K, which is higher than 0.91 for the undoped $(PbTe)_{0.88}(PbS)_{0.12}$ at 473 K.

VI. *PbTe-PbSe* solid solutions

For *PbTe-PbSe* solid solutions comprising *PbSe* the Seebeck coefficients are lower than for *PbTe*, and the Seebeck coefficient is reduced when molar part of *PbSe* is increased (Fig. 13, *b*) Maximum figure of merit values reach $Z = 2.0\times10^{-3}$ K^{-1} which is 30% better than for *PbTe*.

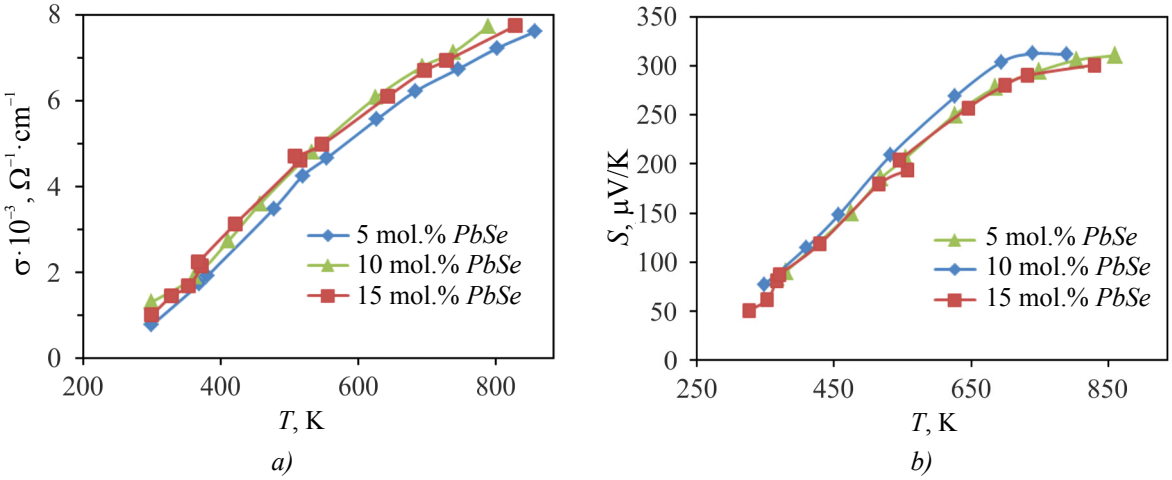

Fig. 13. Temperature dependences of electric conductivity (σ - a), the Seebeck coefficient (S - b) for p-type PbTe-PbSe [26].

The main contribution to figure of merit enhancement is not related to thermal conductivity reduction, but most probably to higher carrier concentration values at elevated temperatures as compared to *PbTe*. The electric properties, hence the thermoelectric figure of merit, is strongly dependent on carrier concentration. The electric resistivity grows with increase in *PbSe* content. This comes as no surprise, since scattering in this system is known to be considerable [26]. The thermoelectric figure of merit is identical for alloys comprising from 5 to 15 mol% *PbSe*. This is the result of equilibration of two competing processes, namely thermal conductivity reduction and electric resistivity increase. Maximum figure of merit is shown by compounds with *PbSe* content from 5 to 15 mol %.

VII. *PbTe-CaTe* (*BaTe*) systems

Ingots (10 g) of *PbTe-CaTe* [0.5-8 mol.% *CaTe*] doped with Na_2Te (1 mol.%) were synthesized by mixing in proper ratios of high purity source components *Pb*, *Ca*, *Te* and Na_2Te in carbon-coated quartz ampoules. The ampoules were sealed in vacuum $3\cdot10^{-3}$ Pa and heated to 1323 K for 15 hours, and then held for 10 hours. Following that, the samples were slowly cooled to 873 K at a rate of 11 K/h and then cooled to room temperature for 15 hours. The test sample of composition *PbTe*-Na_2Te (1 mol.%) was manufactured by the above procedure in a hermetically sealed ampoule with a similar heating profile.

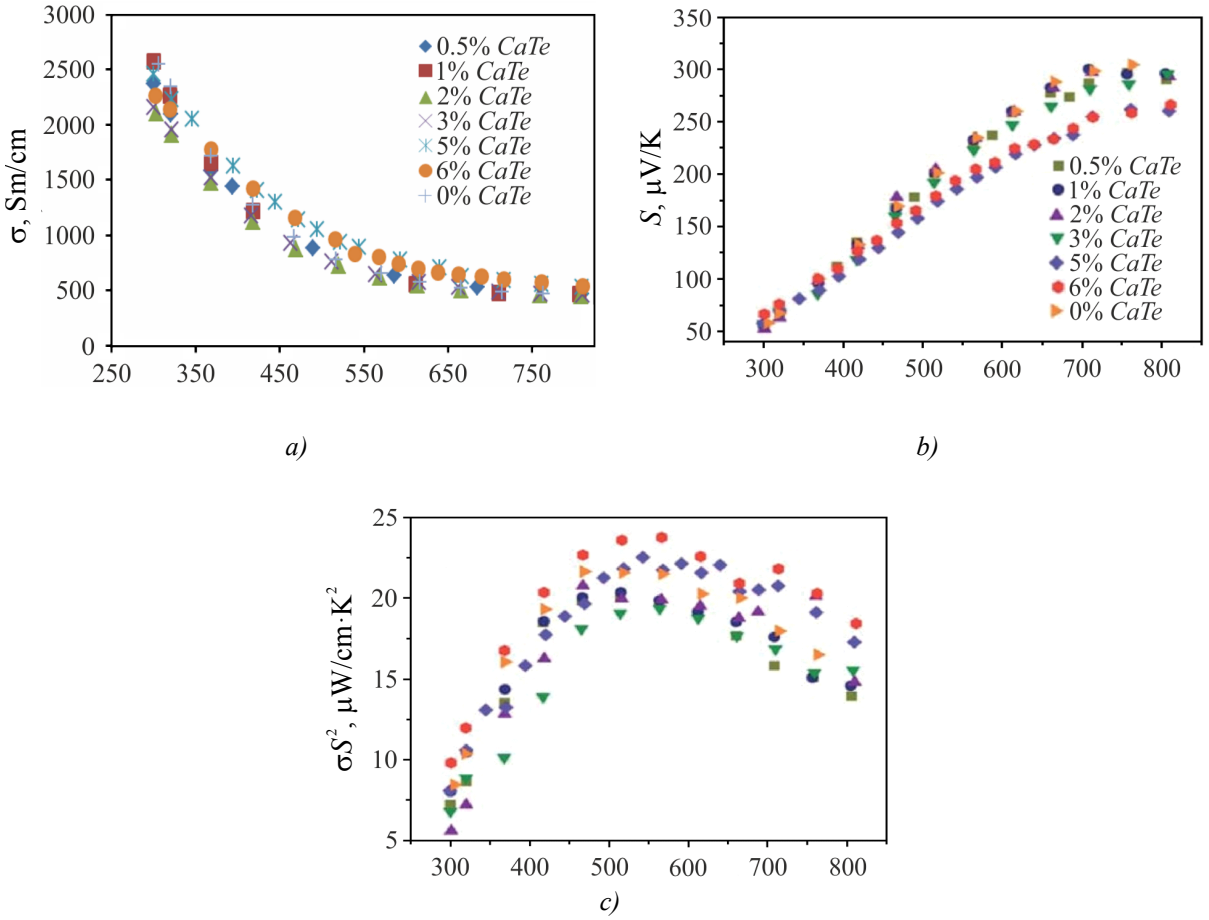

Fig. 14. Temperature dependences of the electric conductivity (σ - a), the Seebeck coefficient (S - b), power factor ($S^2\sigma$ - c) of PbTe-CaTe samples doped with 1 mol.% Na_2Te and PbTe-Na_2Te test sample (1 mol.%) [28].

For all samples of *PbTe-CaTe* doped with 1% Na_2Te, σ is reduced with a rise in temperature, which is indicative of degenerate conductivity for the entire measurement range (300-815 K) (Fig. 14, *a*). As a rule, samples with 6 mol.% *CaTe* had a conductivity from 2240 $S \cdot cm^{-1}$ at room temperature that dropped to 260 $S \cdot cm^{-1}$ at 810 K. Samples including 5 mol.% and 6 mol.% *CaTe* have a higher electric conductivity as compared to others at a higher temperature (450-800 K). The Seebeck coefficients for *PbTe-CaTe* alloys have very similar values, thus, for instance, for *PbTe-CaTe* samples doped with 1 mol.% Na_2Te $S = 57\ \mu V\ K^{-1}$, (Fig. 14, *b*). This is consistent with the theory of the contribution of carriers from the zone of heavy holes already at room temperature due to very high *p*-type doping level.

The value of power factor ($S^2\sigma$) of *PbTe-CaTe* samples doped with 1% Na_2Te and the test sample without *CaTe* as a function of temperature is given in Fig. 14, *c*. The highest value of power factor was 10 $\mu W \cdot cm^{-1} \cdot K^{-2}$ for a sample that comprises 6 mol.% *CaTe* and rises to maximum (24 $\mu W \cdot cm^{-1} \cdot K^{-2}$) at a temperature close to 565 K and at 810 K has the value of 19 $\mu W \cdot cm^{-1} \cdot K^{-2}$. High values of power factor at high temperatures are observed for 5 mol.% and 6 mol.% *CaTe*. This is attributable to a reduction of hole scattering at high temperatures.

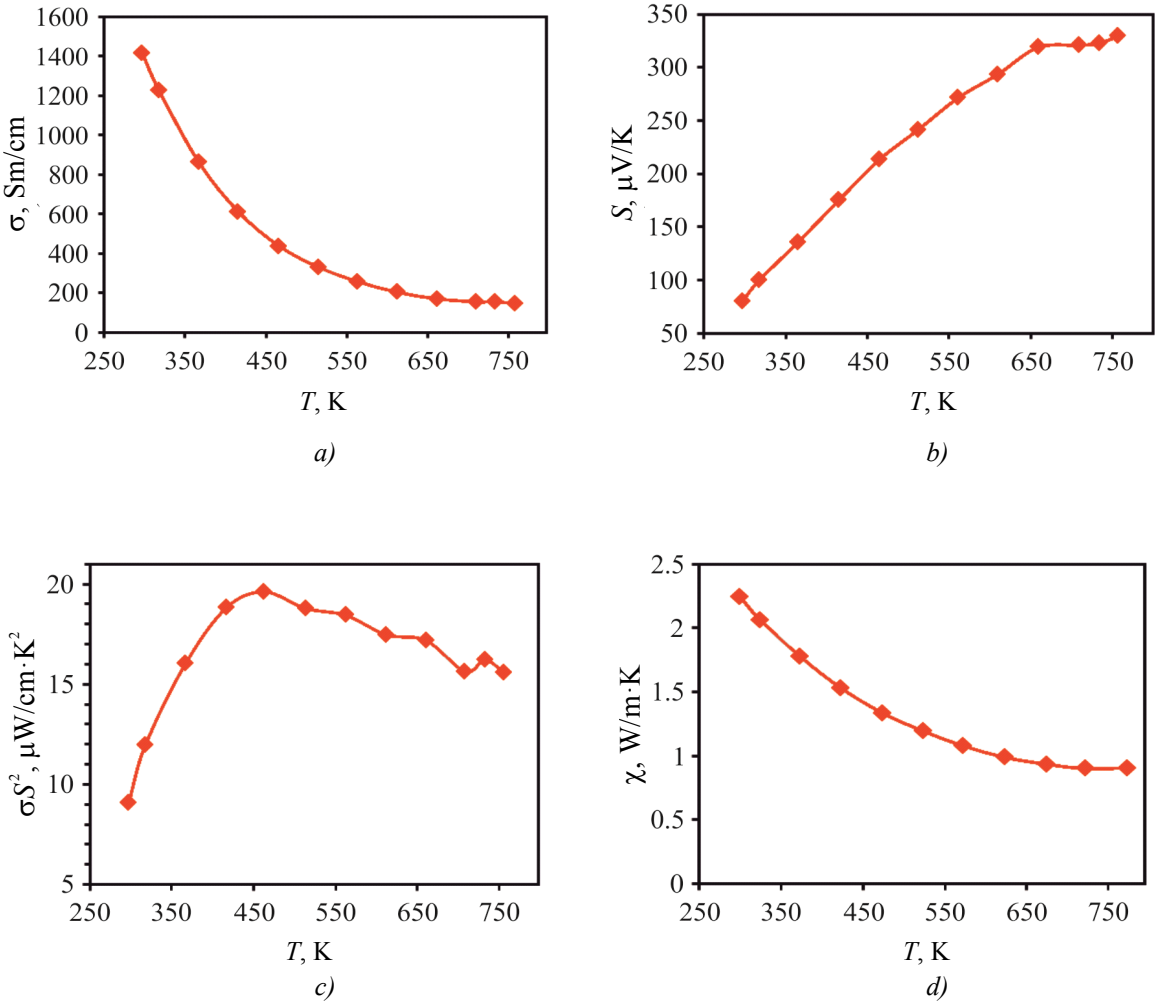

Fig. 15. Temperature dependence of the electric conductivity (σ – a), the Seebeck coefficient (S – b), power factor ($S^2\sigma$ – c) and total thermal conductivity (χ – d) of PbTe-BaTe (3 mol.% BaTe) with the impurity of 1 mol.% Na_2Te [28].

Thermoelectric characteristics of *PbTe-BaTe* alloy (3 mol.%) doped with 1% Na_2Te are represented in Fig. 15. The electric conductivity of sample σ = 1410 $S \cdot cm^{-1}$ at room temperature is reduced to σ = 140 $S \cdot cm^{-1}$ at 760 K. The value of the Seebeck coefficient measured at room temperature was S = 80 $\mu V \cdot K^{-1}$ and is increased to S = 330 $\mu V \cdot K^{-1}$ at 760 K (Fig. 15, *b*). The value of power factor at room temperature is 9 μW cm^{-1} K^{-2} and increases to maximum (20 $\mu W \cdot cm^{-1} \cdot K^{-2}$) at temperature 465 K, and at temperature 760 K it is16 $\mu W \cdot cm^{-1} \cdot K^{-2}$.

Fig. 16, *a* represents the temperature dependence of total thermal conductivity χ of various samples of *PbTe-CaTe* doped with 1% Na_2Te and the test sample. It is clearly seen that introduction of *CaTe* reduces χ. As a rule, at room temperature χ=2.98 $W \cdot m^{-1} \cdot K^{-1}$ was observed in a sample that comprises 6 mol. % *CaTe* and is reduced to 1.05 $W \cdot m^{-1} \cdot K^{-1}$ at 825 K.

Fig. 17, *a* represents the temperature dependences of *ZT* for different samples of *PbTe-CaTe* doped with 1 mol. % Na_2Te and a test sample that has no *CaTe*. The highest *ZT* 1.5 was achieved at 765 K for the sample with 6 mol.% *CaTe* which is 55% higher than in the test *p*-type *PbTe*. The sample with 5 mol.% *CaTe* also shows high value of *ZT* = 1.45 at 715 K. Samples with the content of (0.5-3) mol.% *CaTe* have *ZT* value in the range from 1.2 to 1.3 at (685-760) K.

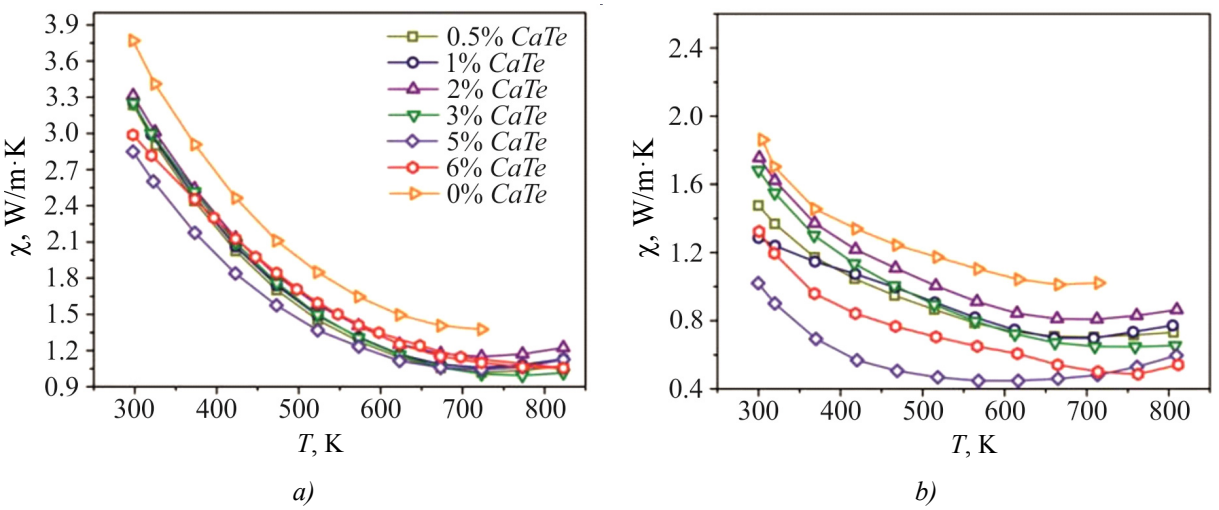

Fig. 16. Temperature dependences of total (χ - a) and lattice thermal conductivity (χ_{lat} - b) of PbTe-CaTe samples doped with 1 mol. % Na_2Te and test sample of composition PbTe-Na_2Te (1 mol.%) [28].

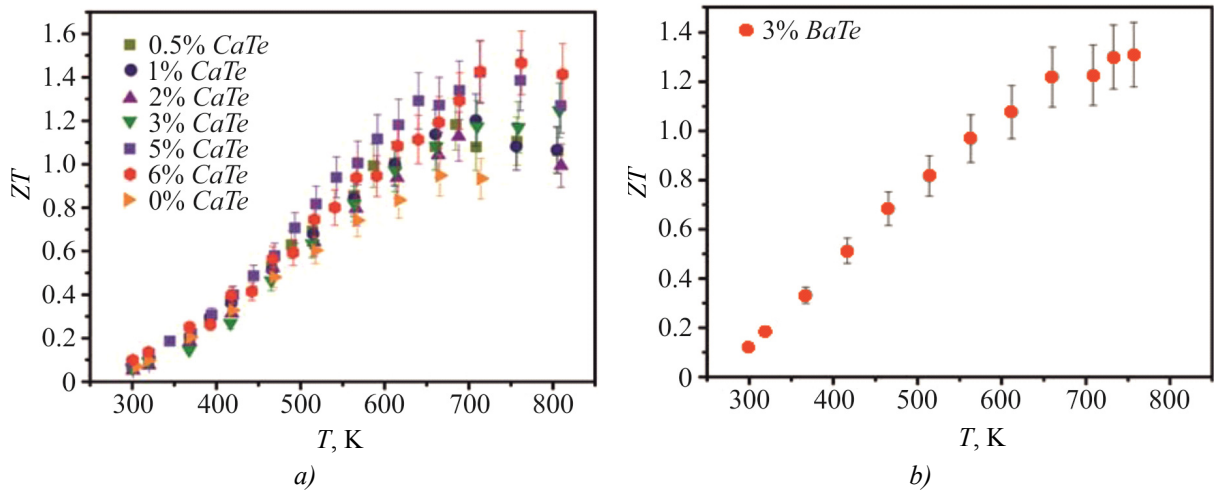

Fig. 17. Temperature dependences of thermoelectric figure of merit (ZT) for (a) PbTe- CaTe samples doped with 1 mol. % Na_2Te and (b) PbTe- BaTe (3 mol. % BaTe) doped with 1% Na_2Te [28].

With increasing concentration of *CaTe*, *ZT* maximum is displaced from 685 K to 765 K, which is due to higher hole concentration in these samples. For the sample of *PbTe-BaTe* (3 mol.% *BaTe*) doped with Na_2Te (1 mol.%) $ZT = 1.3$ was achieved at 760 K (Fig. 17, *b*).

Conclusions

1. Characteristics and analysis of the thermoelectric properties of solid solutions obtained on the basis of lead telluride and chalcogenide compounds of other elements of the periodic table are presented.
2. It is established that *PbTe-*Ag_2Te_3 alloys have low lattice thermal conductivity through the presence of Ag_2Te_3 nanoinclusions and excellent electronic properties due to complex structure of valence band yielding $ZT > 1.5$ at high temperatures.
3. It is shown that for solid solutions based on *PbTe-*Sb_2Te_3 and *PbTe-*Bi_2Te_3 the thermoelectric properties depend on the content of Sb_2Te_3(Bi_2Te_3), and it is established that the optimal content is 0.03 mol.% Sb_2Te_3 and 0.3 mol.% Bi_2Te_3, respectively.

4. The *PbTe-PbS* solid solutions with 8 mol.% *PbS* are unique in that they can be obtained in two forms, namely solid solution and nanostructured material which together with spinodal decomposition scatter phonons on phase boundaries and thus reduce the thermal conductivity.
5. In *PbTe-PbSe* solid solutions, the Seebeck coefficients are lower than in pure *PbTe*, and maximum figure of merit values $Z = 2.0\times10^{-3}$ K^{-1}, which is possible due to high values of carrier concentration.
6. Samples of *PbTe-CaTe* (*BaTe*) systems with the content of 5 mol.% *CaTe* show high value of ZT = 1.45 at 715 K, and samples with 3 mol.% *BaTe* have the value of *ZT* = 1.3 at 760K.

The work was performed in conformity with the scientific projects of the Ministry of Education and Science of Ukraine (registration number 0113U000185) and NATO's Public Diplomacy Division as part of program "Science for the Sake of Peace" (NUKR, SEPP 984536).

References

1. L.E. Bell, Cooling, Heating, Generating Power, and Recovering Waste Heat with Thermoelectric Systems, *Science* **321**(5895), 1457 (2008).
2. V.M. Shperun, D.M. Freik, and R.I. Zapukhlyak, *Thermoelectricity of Lead Telluride and its Analogs* (Ivano-Frankivsk: Plai, 2000), 250 p.
3. J.P. Heremans, V. Jovovic, E.S. Toberer, A. Saramat, K. Kurosaki, A. Charoenphakdee, S. Yamanaka, and G.J. Snyder, Enhancement of Thermoelectric Efficiency in *PbTe* by Distortion of the Electronic Density of States, *Science* **321**(5888), 554 (2008).
4. K.F. Hsu, S. Loo, Fu Guo, W. Chen, J.S. Dyck, C. Uher, T. Hogan, E.K. Polychroniadis, and M.G. Kanatzidis, Cubic $AgPb_mSbTe_{2+m}$: Bulk Thermoelectric Materials with High Figure of Merit, *Science* **303**(5659), 818 (2004).
5. Y. Pei, N.A. Heinz, A. LaLonde, and G.J. Snyder, Combination of Large Nanostructures and Complex Band Structure for High Performance Thermoelectric Lead Telluride, *Energy Environ. Sci.* **4**, 3640–3645 (2011).
6. O.G. Karpinskii, L.E. Shelimova, E.S. Avilov, M.A. Kretova, and V.S. Zemskov, X-ray Diffraction Study of Mixed-Layer Compounds in the *PbTe*-Bi_2Te_3 System, *Inorganic Materials* **38**(1), 17–24 (2002).
7. T. Sua, P. Zhua, H. Maa, G. Rend, J. Guoa, Y. Imai, and X. Jia, Electrical Transport and Thermoelectric Properties of *PbTe* Doped with Sb_2Te_3 Prepared by High-Pressure and High-Temperature, *J. Alloys and Compounds* **422**, 328–331 (2006).
8. N.V. Chandra Shekar, D.A. Polvani, J.F. Meng, and J.V. Badding, Improved Thermoelectric Properties due to Electronic Topological Transition under High Pressure, *Physica B* **358**, 14–18 (2005).
9. K.Kishimoto, K.Yamamoto, and T.Koyanagi, Influences of Potential Barrier Scattering on the Thermoelectric Properties of Sintered n-Type PbTe with a Small Grain Size, *Jpn. J. Appl. Phys*. **42**, 501–508 (2003).
10. P.W. Zhu, Y. Imai, Y. Isoda, Y. Shinohara, X. P.Jia, and G.T. Zou, *Mater. Transact*. **46**, 1810–1813 (2005).
11. G.B. Bokii, *Crystal Chemistry* (Nauka: Moscow, 1971), 139 p.
12. P. Zhua, Y. Imai, Y. Isoda, Y. Shinohara, X. Jia, and G. Zou, Composition Dependent Thermoelectric Properties of *PbTe* Doped with Bi_2Te_3, *J. Alloys and Compounds* **420**, 233–236 (2006).

13. E.S. Itskevich, L.M. Kashirskaya, and V.F. Kraidenov, Anomalies in the Low-Temperature Thermoelectric Power of *p-*Bi_2Te_3 and *Te* Associated with Topological Electronic Transitions under Pressure, *Semiconductors* **31**, 276–278 (1997).
14. Y.M. Blanter, M.I. Kaganov, A.V. Pantsulaya, and A.A. Varlamov, The Theory of Electronic Topological Transitions, *Phys. Rep*. **245**, 160–257 (1994).
15. S.N. Girard, K. Schmidt-Rohr, T.C. Chasapis, E. Hatzikraniotis, B. Njegic, E.M. Levin, A. Rawal, K.M. Paraskevopoulos, and M.G. Kanatzidis, Analysis of Phase Separation in High Performance *PbTe-PbS* Thermoelectric Materials, *Adv. Funct. Mater*. **23**(6), 747–757 (2013).
16. M.S. Darrow, W.B. White, and R. Roy, Micro-Indentation Hardness Variation as a Function of Composition for Polycrystalline Solutions in the Systems *PbS*/*PbTe*, *PbSe*/*PbTe*, and *PbS*/*PbSe*, *J. Materials Science* **4**, 313-319 (1969).
17. J. He, M.G. Kanatzidis, and V.P. Dravid, High Performance Bulk Thermoelectrics via a Panoscopic Approach, *Materials Today* **16**(5), 166-176 (2013).
18. S.N. Girard, J. He, C. Li, S. Moses, G. Wang, C. Uher, V.P. Dravid, and M.G. Kanatzidis, In Situ Nanostructure Generation and Evolution within a Bulk Thermoelectric Material to Reduce Lattice Thermal Conductivity, *Nano Lett.* **10**(8), 2825 (2010).
19. J. He, S.N. Girard, M.G. Kanatzidis, and V.P. Dravid, Microstructure-Lattice Thermal Conductivity Correlation in Nanostructured $PbTe_{0.7}S_{0.3}$ Thermoelectric Materials, *Adv. Funct. Mater*. **20**(5), 764 (2010).
20. X.X. Li, J.Q. Li, F.S. Liu, W.Q. Ao, H.T. Li, and L.C. Pan, Enhanced Thermoelectric Properties of $(PbTe)_{0.88}(PbS)_{0.12}$ Composites by Bi Doping, *J.Alloys and Compounds* **547**, 86–90 (2013).
21. J. Androulakis, C.H. Lin, H.J. Kong, C. Uher, C.I. Wu, T. Hogan, B.A. Cook, T. Caillat, K.M. Paraskevopoulos, and M.G. Kanatzidis, Spinodal Decomposition and Nucleation and Growth as a Means to Bulk Nanostructured Thermoelectrics: Enhanced Performance in $Pb_{1-x}Sn_xTe$-*PbS*, *J. Am. Chem. Soc.* **129**, 9780–9788 (2007).
22. W. Liu, X.F. Tang, H. Li, K. Yin, J. Sharp, X.Y. Zhou, and C. Uher, Enhanced Thermoelectric Properties of *n*-type $Mg_{2.16}(Si_{0.4}Sn_{0.6})_{1-y}Sb_y$ due to Nano-Sized *Sn*-rich Precipitates and an Optimized Electron Concentration, *J. Mater. Chem*. **22**, 13653 (2012).
23. J.Q. Li, X.X. Li, F.S. Liu, W.Q. Ao, and H.T. Li, Enhanced Thermoelectric Properties of $(PbTe)_{0.88}(PbS)_{0.12}$ Composites by *Sb* Doping, J. *Electronic Materials*, **42**(3), 2013.
24. I. Kudman, Thermoelectric Properties of *p*-type *PbTe-PbSe* Alloys, *J. Materials Science* **7**, 1027-1029 (1972).
25. D.L. Partin, C.M. Thrush, and B.M. Clemens, Lead Strontium Telluride and Lead Barium Telluride Grown by Molecular-Beam Epitaxy, *J.Vac.Sci.Technol*. **B 5**, 686 (1987).
26. K. Biswas, J. He, G. Wang, S.-H. Lo, C. Uher, V.P. Dravid, and M.G. Kanatzidis, High Thermoelectric Figure of Merit in Nanostructured *p*-type *PbTe-MTe* (*M* = *Ca*, *Ba*), *Energy Environ. Sci.* **4,** 4675–4684 (2011).

Submitted 22.07.14

V.A.Romaka[1,2], P.Rogl[3], Yu.V.Stadnyk[4], L.P.Romaka[4], R.O.Korzh[2], D. Kaczorowski[5], V.Ya. Krayovskyy[2], A.M. Horyn[4]

[1]Ya. Pidstryhach Institute for Applied Problems of Mechanics and Mathematics National Academy of Sciences of Ukraine, 3-b Naukova St., Lviv, 79060, Ukraine;
[2]National University "Lvivska Polytechnika", 12 S.Bandera St., Lviv, 79013,Ukraine;
[3]Universität Wien, Währinger St. 42, A-1090, Wien, Österreich;
[4]Ivan Franko National University of Lviv, 6 Kyryla and Mefodiya St., 79005, Lviv, Ukraine;
[5]W.Trzebiatowski Institute of Low Temperature and Structural Research Polish Academy of Sciences, 2 Okolna St., Wroclaw, 50-950 Poland

PECULIARITIES OF STRUCTURAL, ENERGY AND KINETIC CHARACRERISTICS OF $VFe_{1-x}Ti_xSb$ THERMOELECTRIC MATERIAL

The crystalline and electronic structures, the temperature and concentration dependences of the electric resistivity and the Seebeck coefficient of $VFe_{1-x}Ti_xSb$ thermoelectric material have been studied in the ranges of $T = 4.2 - 400$ K and $N_A^{Ti} \approx 9.5 \cdot 10^{19}$ cm^{-3} ($x = 0.005$) – $3.9 \cdot 10^{21}$ cm^{-3} ($x = 0.15$).The mechanism of simultaneous generation of defects of donor and acceptor nature was established. They change the compensation degree of semiconductor material and determine mechanism of conduction.

Key words: electronic structure, electric resistivity, Seebeck coefficient.

Introduction

As is known, parameter optimization of thermoelectric materials to obtain maximum values of thermoelectric figure of merit depends on a number of factors, in particular, carrier concentration (doping degree), scattering mechanisms, thermal conductivity, selection of crystallographic orientation, etc. [1]. The respective doping of intermetallic semiconductors, in particular, *n-ZrNiSn*, *n-TiNiSn*, *n-HfNiSn* and *n-VFeSb* (*MgAgAs* structural type, $F\bar{4}3m$ space group), allows obtaining simultaneously high values of electric conductivity, the Seebeck coefficient and low values of thermal conductivity coefficient, assuring high efficiency of thermal into electric energy conversion and making them most studied new thermoelectric materials [2-6].

In this work, that contributes to further study of the effect of heavy doping (N_A,$N_D \sim 10^{19} \div 10^{21}$ cm^{-3}) of this class of semiconductors on their structural, energy, electrophysical and magnetic properties [2], we determine conditions for the origination of maximum thermoelectric power factor Z^* ($Z^* = \alpha^2 \cdot \sigma$, where α is the Seebeck coefficient, σ is the electric conductivity) on doping of *n-VFeSb* with *Ti* atoms introduced into the compound by substitution for *Fe* atoms. The investigation also showed that obtaining a positive result, for instance, high Z^* values, without insight into deep processes in material structure and electric conductivity mechanisms, is, as a rule, of casual nature and will prevent from developing high-performance materials for thermal into electric energy conversion.

Investigation procedures

The object to be investigated included crystalline structure, electron density distribution (DOS), the kinetic and energy characteristics of $VFe_{1-x}Ti_xSb$. The samples were synthesized in the laboratory of Institute for Physical Chemistry, Vienna University. The X-ray structural analysis with employment of Fullprof program [7] was used to obtain the values of crystal lattice periods. The data arrays obtained by the powder method (diffractometer Guinier-Huber image plate system) were used for the calculation of structural characteristics. The chemical and phase compositions of samples were controlled by scanning electron microscope (SEM, Zeiss Supra 55VP) and microprobe analyzer (EPMA, energy-dispersive X-ray analyzer). The electronic structure calculations were performed by the Korringa-Kohn-Rostoker (KKR) method in coherent potential approximation (CPA) and local density approximation (LDA) [8]. For the calculations use was made of lattice constant values on *k*-net of size 10×10×10 and parametrization type of Moruzzi-Janak-Williams exchange-correlation potential [9]. The width of energy window covered by the loop is 16 eV. The number of energy values for the calculation of DOS was 1000. The temperature and concentration dependences of the electrical resistivity (ρ) and the Seebeck coefficient (α) of $VFe_{1-x}Ti_xSb$ samples were measured with respect to copper in the ranges: $T = 4.2 - 400$ K, $N_A^{Ti} \approx 9.5 \cdot 10^{19}$ cm^{-3} ($x = 0.005$)–$3.9 \cdot 10^{21}$ cm^{-3} ($x = 0.15$).

Research on the electrokinetic and energy characteristics of $VFe_{1-x}Ti_xSb$

The initial testing of $VFe_{1-x}Ti_xSb$ samples for their homogeneity, the presence of uncontrolled phases and the fact of dissolution of impurity atoms in the matrix of *VFeSb* compound performed with the aid of X-ray phase and structural analyses, revealed no traces of other phases, except for the basic one. In turn, the values of unit cell period increased, which is reasonable, since the atomic radius of *Ti* (r_{Ti} = 0.145 nm) is larger than that of *Fe* (r_{Fe} = 0.127 nm). The results of testing served the basis for further electrokinetic research.

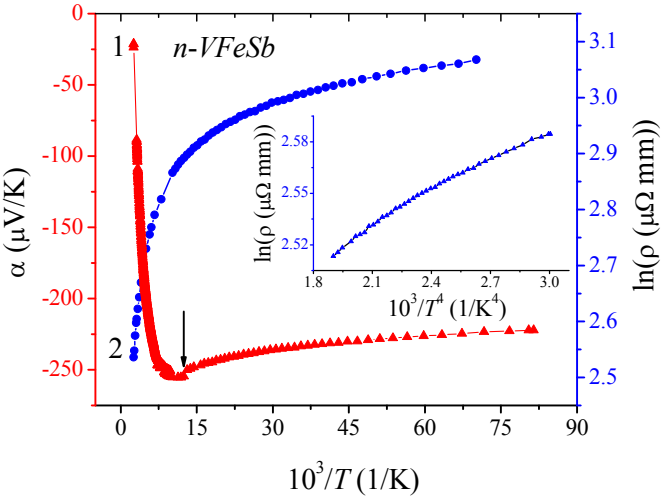

Fig. 1. Temperature dependences of the electric resistivity ln(ρ(1/T) (1) and the Seebeck coefficient α(1/T) (2) of n-VFeSb. Inset: dependence ln(ρ(1/T)$^{1/4}$) in the range of T = 12 – 80 K.

Taking into account that the object of study is $VFe_{1-x}Ti_xSb$ solid solution, it is reasonable to start from the analysis of characteristics of basic *n-VFeSb* semiconductor, and Fig. 1 shows the temperature dependences of the electric resistivity $\ln\rho(1/T)$ and the Seebeck coefficient $\alpha(1/T)$. It is seen that in

the range of $T = 4.2 - 80$ K we have hopping conduction of activation nature with a variable jump length (*vrh*) ε_3^ρ [10], as indicated by the linear dependence $\ln(\rho(1/T)^{1/4})$ (inset in Fig. 1).

In turn, the negative values of the Seebeck coefficient speak for electrons as the majority charge carriers. With a rise in temperature ($T > 80$ K), the activation conduction changes into band (metallic) conduction determined by free electrons, and the Fermi level ε_F goes from the impurity donor band to conduction band. Under such conditions, the values of $\rho(T)$ increase with a rise in temperature due to scattering mechanisms (Fig. 2*a*, curve 1).

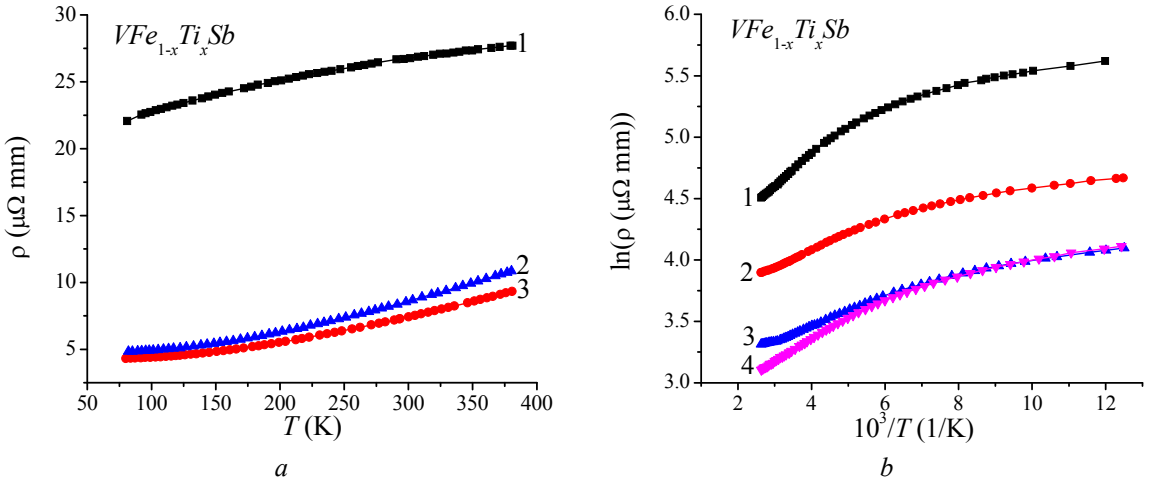

Fig. 2. Temperature dependences of the electric resistivity ρ of $VFe_{1-x}Ti_xSb$: a) 1 – x = 0, 2 – x = 0.01, 3 – x = 0.02, b) 1 – x = 0.03, 2 – x = 0.05, 3 – x = 0.10, 4 – x = 0.15.

In transient region from the activation to band conduction (arrow in Fig. 1) we managed to determine the activation energy from the Fermi level ε_F to conduction band $\varepsilon_1^\rho = 1.6$ meV. On the other hand, the fact that hopping conduction is defining up to 80 K, and between the conduction band and impurity band there is a small energy gap, is indicative of considerable impurity band width (~7 meV).

Introduction of *Ti* atoms into *VFeSb* compound by substitution for *Fe* atoms must generate in a crystal structural defects of acceptor nature, since *Ti* ($3d^2 4s^2$) has four 3*d*-electrons less than *Fe* ($3d^6 4s^2$). Figs. 2-4 show the temperature and concentration dependences of the electric resistivity and the Seebeck coefficient of $VFe_{1-x}Ti_xSb$. As long as in *n-VFeSb* the Fermi level ε_F is in conduction band, doping of semiconductor with the lowest concentrations of *Ti* acceptor impurity must lead to a reduction of free electrons concentration, and the Fermi level ε_F must drift to the band bottom. As is seen from Fig. 2*a*, in the concentration range of $VFe_{1-x}Ti_xSb$, $0 \le x \le 0.02$, the semiconductor has still nonactivation, metallic type of conduction, indicating to location of the Fermi level in conduction band. However, surprising is the fact that at fixed temperature in the same concentration range the values of $\rho(x)$ are reduced (Fig. 3*a*).

For instance, at $T = 160$ K the values of $\rho(x = 0) = 24.28$ μΩ·m are reduced to $\rho(x = 0.005) = 5.11$ μOhm·m and $\rho(x = 0.01) = 4.96$ μΩ·m. That is, by introducing into *n-VFeSb* a huge number of acceptors ($N_A^{Ti} \approx 3.8 \cdot 10^{20}$ cm^{-3}) we not only managed to "draw" the Fermi level ε_F to the energy gap, but, on the contrary, conduction seems to have increased, which in a semiconductor is possible only with increase in the number of free electrons. This result suggests that in $VFe_{1-x}Ti_xSb$

crystal, simultaneously with acceptors, donors are generated by the mechanism which is unknown so far. Another variant of such ρ(*x*) behaviour is assumption on the liquidation of semiconductor material state.

At the concentrations $N_A^{Ti} \approx 5.7\cdot10^{20}$–$1.9\cdot10^{21}$ cm^{-3} ($x = 0.03$–0.15) the temperature dependences of electric resistivity of $VFe_{1-x}Ti_xSb$ expectedly acquire semiconductor nature (Fig. 2*b*) indicating that the Fermi level ε_F has left conduction band for the energy gap. This result confirms the acceptor nature of structural defects that originate in $VFe_{1-x}Ti_xSb$ crystal, which accounts for a drastic increase in ρ(*x*) values (Fig. 3*a*). At the same time, the nature of change in the values of the Seebeck coefficient α(*x*) (Figs. 3*b*, 4) testifies that the Fermi level is now located near the valence band, since the Seebeck coefficient values are now positive.

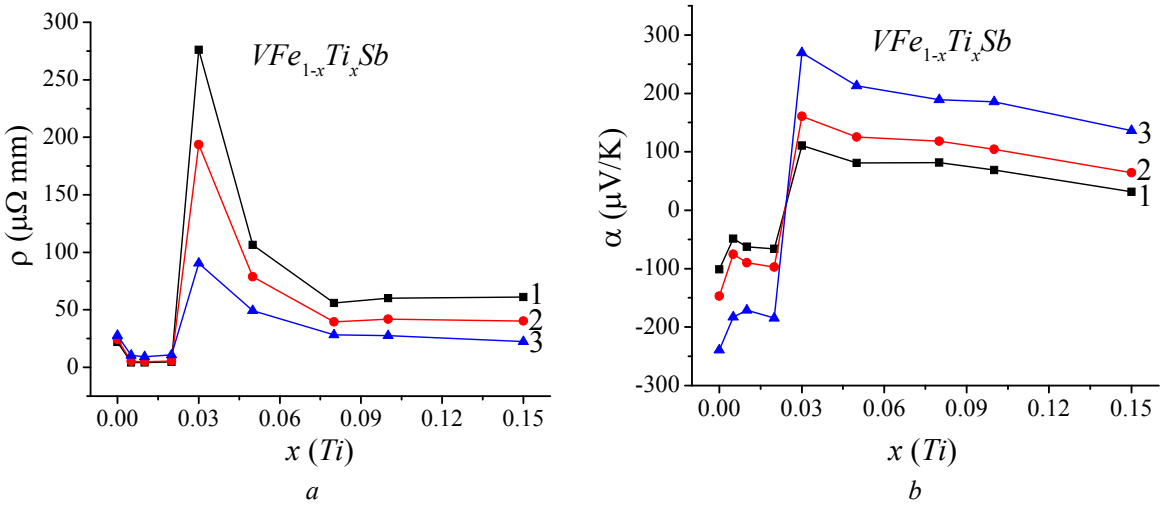

Fig. 3. Change in the values of the electric resistivity ρ(x) (a)and the Seebeck coefficient α(x) (b) of $VFe_{1-x}Ti_xSb$ at different temperatures: 1 – T = 80 K, 2 – T = 160 K, 3 – T = 380 K.

From the activation areas of $\ln\rho(1/T)$ dependences (Fig. 2*b*) we calculated the values of activation energies from the Fermi level ε_F to percolation level of conduction band (valence band) ε_1^ρ and electron jumps ε_3^ρ along the states with the energies close to the Fermi level, and from the activation areas of $\alpha(1/T)$ dependences (Fig. 4) – the values of activation energies ε_1^α and ε_3^α that yield, respectively, the values of modulation amplitude of intermittent energy bands and small-scale fluctuation of heavily doped and strongly compensated semiconductor (Fig. 5) [2, 10]. It is clear that the higher is compensation degree, the larger is modulation amplitude [10].

Recall that compensation degree shows the ratio between the number of ionized donors and acceptors: the closer are their values, the higher is compensation degree, and with full compensation the number of acceptors and donors is equal. In the case of *n-VFeSb* the amplitude value of large-scale fluctuation is $\varepsilon_1^\alpha = 41.5$ meV, and the depth of potential well $\varepsilon_3^\alpha = 0.2$ meV.

Substitution in *VFeSb* compound of the smallest in the experiment number of *Fe* atoms for *Ti* ($x = 0.005$) atoms is expectedly accompanied by a drastic increase in semiconductor degree of compensation, which points to growth of dependence $\varepsilon_1^\alpha(x)$ on the area $VFe_{1-x}Ti_xSb$, $x = 0$–0.005 (Fig. 5*a*). However, further introduction of acceptor impurity into a semiconductor which is still *n*-type ($\alpha(x) < 0$), when the Fermi level ε_F is still in conduction band, is unexpectedly attended by the same drastic decrease in the values of modulation amplitude of continuous energy bands $\varepsilon_1^\alpha(x)$.

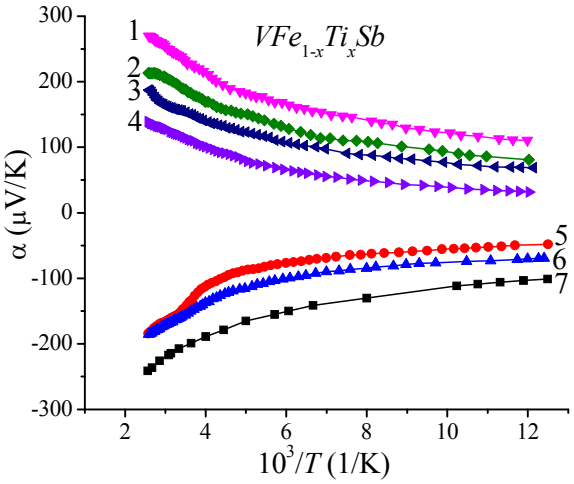

Fig. 4. Temperature dependences of the Seebeck coefficient α(1/T) of $VFe_{1-x}Ti_xSb$: 1 – x = 0.03, 2 – x = 0.05, 3 – x = 0.10, 4 – x = 0.15, 5 – x = 0.005, 6 – x = 0.02, 7 – x = 0.

Such a decrease in the values $\varepsilon_1^{\alpha}(x)$ on the area of concentrations $0.005 < x < 0.03$ is possible only when, simultaneously with acceptors, donors are generated in a crystal by the mechanism which is so far unknown. In so doing, in the concentration area $0.005 < x < 0.03$ the rate of generation of donors in $VFe_{1-x}Ti_xSb$ seems to be higher compared to acceptors. A similar conclusion was also made on the basis of $\rho(x)$ behaviour in the same concentration area, when on introducing into n-type semiconductor of acceptor impurity the values of $\rho(x)$ were not increased, as expected, but reduced (Fig. 3*a*). The concentration limits of uncontrolled donors can be estimated as N_D: $3.6 \cdot 10^{20}$ cm^{-3} ($x = 0.02$) < N_D < $5.7 \cdot 10^{20}$ cm^{-3} ($x = 0.03$). Another variant of such behaviour $\varepsilon_1^{\alpha}(x)$ in the concentration area $0.005 < x < 0.03$ is the assumption of liquidation of semiconductor material state.

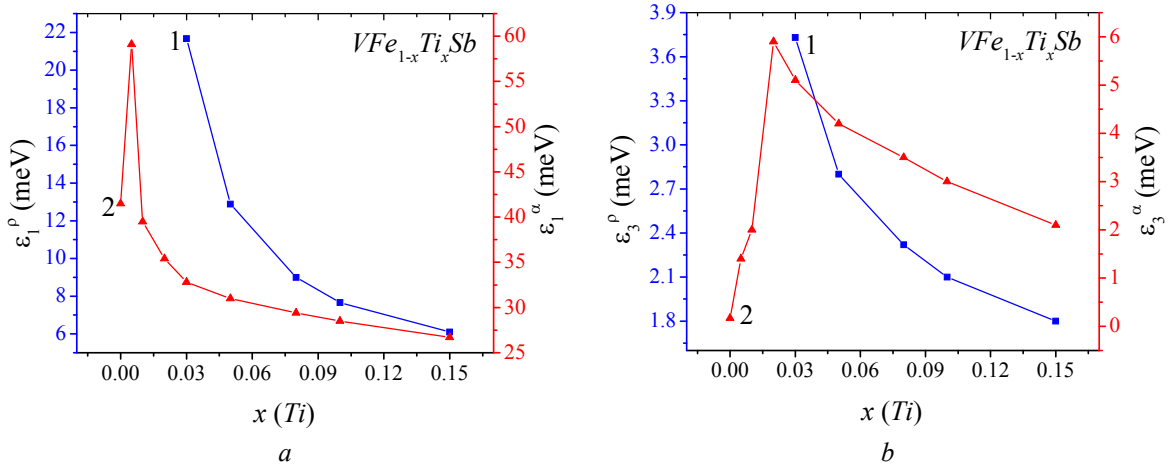

Fig. 5. Change in the values of activation energies (1) and (2) (a) and (1) and (2) (b) of $VFe_{1-x}Ti_xSb$.

The conductivity of $VFe_{1-x}Ti_xSb$, $0.03 \le x \le 0.15$ is of semiconductor nature, and the value of $\alpha(x) > 0$, pointing to a change in the type of majority carriers from electrons to holes. Thus, the rate and concentration of generated acceptors exceeds the rate and concentration of donors. As a result, the compensation degree is reduced, as indicated by the decay of dependence $\varepsilon_1^{\alpha}(x)$ (Fig. 5*a*).

At the concentrations of *Ti* impurity, when material shows semiconductor properties, the fact of drift of the Fermi level ε_F to valence band shows the nature of change in the values of activation

energy $\varepsilon_1^{\rho}(x)$ from the Fermi level ε_F to valence band edge (Fig. 5*a*). It is seen that the energy gap between the Fermi level and valence band edge is reduced from $\varepsilon_1^{\rho}(x=0.03)=21.7$ meV to $\varepsilon_1^{\rho}(x=0.15)=6.1$ meV, and the concentration of *Ti* impurity proved to be insufficient for valence band to be crossed by the Fermi level.

Predicted is behaviour of hopping conduction activation energy $\varepsilon_3^{\rho}(x)$ in $VFe_{1-x}Ti_xSb$, $0.03 \le x \le 0.15$. The fact that the values of energy $\varepsilon_3^{\rho}(x)$ are drastically reduced is related to increased overlapping of acceptor wave functions due to their large concentration ($N_A^{Ti} \approx 3.9\cdot10^{21}$ cm^{-3} ($x = 0.15$)). On the contrary, the depth of potential well of small-scale fluctuation which is proportional to ε_3^{α}, starts to be reduced only after crossing by the Fermi level of the mid band gap, which agrees with the pattern of change in the values of continuous energy modulation amplitude $\varepsilon_1^{\alpha}(x)$.

Thermoelectric power factor of $VFe_{1-x}Ti_xSb$

Fig. 6 represents a change in the values of thermoelectric power factor $Z^*(x)$ from which it is seen that in the concentration range $0 < x < 0.03$ the values of $Z^*(x)$ in $VFe_{1-x}Ti_xSb$ are greater than in the undoped semiconductor *VFeSb*. From Fig. 6 it also follows that when crossing the Fermi level and conduction band percolation level, when the values of the Seebeck coefficient are still high, and the values of the electric conductivity of $VFe_{1-x}Ti_xSb$ are already high, on the dependences $Z^*(x)$ there are extremes at all investigated temperatures, which corresponds to criterion of achievement of maximum values of thermoelectric power factor Z^* [2].

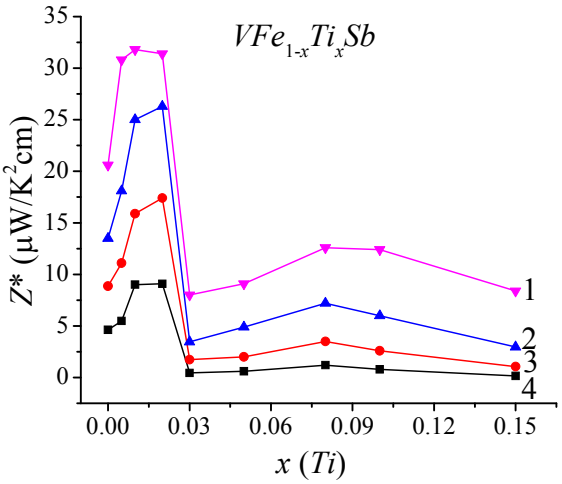

Fig. 6. Change in the values of thermoelectric power factor Z of $VFe_{1-x}Ti_xSb$: 1 – T = 380 K; 2 – T = 250 K; 3 – T = 160 K; 4 – T = 80 K.*

Thus, on the basis of the results of electrokinetic studies presented here it can be asserted that the obtained solid solution $VFe_{1-x}Ti_xSb$ is a promising thermoelectric material. However, the level of investigations performed did not allow clear identification of electric conductivity mechanisms, which makes it impossible to predict the kinetic characteristics of $VFe_{1-x}Ti_xSb$ and to develop the technology of thermoelectric material production with high efficiency of thermal into electric energy conversion. This gave an impetus to in-depth study of spatial arrangement of atoms in $VFe_{1-x}Ti_xSb$ and of semiconductor electron structure.

Refinement of crystalline and electronic structures of $VFe_{1-x}Ti_xSb$

First and foremost, it is necessary to understand what determines the electron type of conduction of *VFeSb* compound. A microprobe analysis of the surface of *VFeSb* samples revealed 1% deficit of *Sb* atoms. A similar result was obtained in [11], which is attributable to the presence of structural defects in the form of vacancies in position 4*b* of *Sb* atoms. The refinement of *VFeSb* crystalline structure by virtue of low concentration of structural defects prevented from the identification of vacancies: the models of crystalline structure were in the limits of error both for the variant of 100% occupation by atoms of their positions, and for the variant of existence of ~ 1% vacancies of *Sb* atoms. Based on the ordered model of structure *VFeSb*, where all the atoms occupy positions in conformity with *MgAgAs* structural type, and the occupation degree is 100%, the value of crystal lattice period $a(x)$ was calculated (Fig. 7*a*).

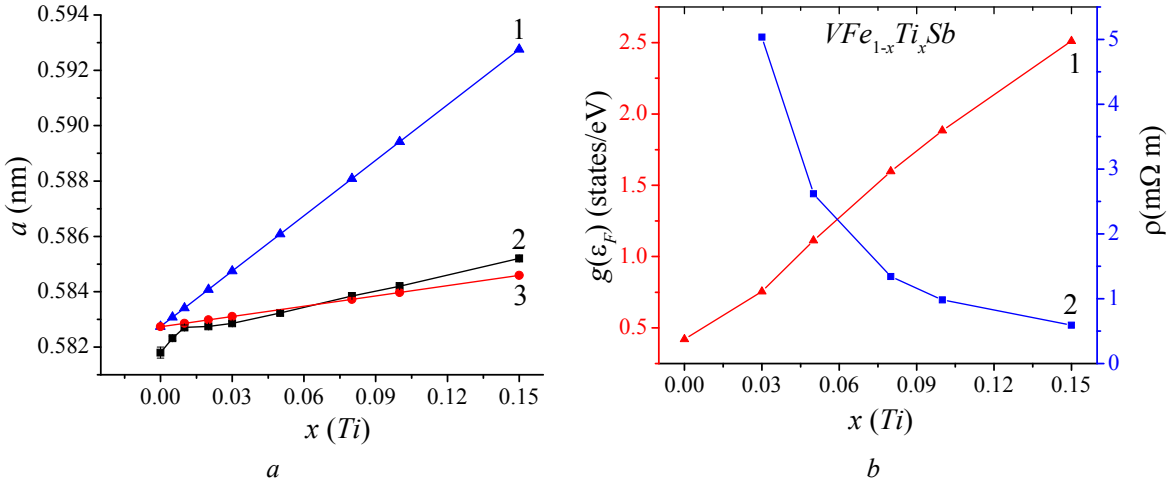

Fig. 7. Change in the values of crystal lattice period a(x) (a) and calculated DOS values on the Fermi level $g(\varepsilon_F)$ and the electric resistivity ρ(x) (b) of $VFe_{1-x}Ti_xSb$: a) 1 – calculation with Ti atoms substituted for Fe; 2 – experimental results, 3 – calculation with Ti atoms substituted for V; b) 1 – $g(\varepsilon_F)$, 2 – ρ(x).

It turned out that the values of period obtained from the experiment are lower than calculated ones, namely $a_{exp} = 0.5818$ nm and $a_{calc} = 0.5827$ nm. The question arises: what is the reason for this difference? If it is remembered that microprobe analysis revealed *Sb* deficit of ~ 1% [11], as well as the assumption that this can be manifestation of vacancies in position 4*b* of *Sb* atoms, then the difference in the values of *VFeSb* lattice period can serve a weighty argument for this assumption.

On the other hand, the assumption as to the presence in *VFeSb* structure of vacancies in 4*b* position which is equivalent to generation of donors looks logical, being consistent with the above results of kinetic research of *n-VFeSb* that pointed to the existence in semiconductor of donors of unknown origin. Thus, the negative values of the Seebeck coefficient of *VFeSb* and the presence of hopping mechanism of charge transport along the impurity donor band formed by defects is another argument for the assumption of the presence of vacancies in position (4*b*) of *Sb* atoms.

Taking into account that the atomic radius of *Ti* (r_{Ti} = 0.145 nm) is larger than that of *Fe* (r_{Fe} = 0.127 nm), it is reasonable to increase the values of crystal lattice period $a(x)$ of $VFe_{1-x}Ti_xSb$ with increasing the content of *Ti* (Fig. 7*a*, curve 2). Based on the assumption that doping of *n-VFeSb* with *Ti* atoms is accompanied by ordering of crystalline structure, and impurity atoms of *Ti* displace *Fe* atoms from crystallographic position 4*c*, a change in $a(x)$ values was calculated(Fig. 7*a*, curve 1). In the calculations we assumed that the initial structure *VFeSb* is ordered.

Comparison of two dependences, i.e. a change in the values of unit cell period $a(x)$ obtained experimentally and calculated for the case of substitution of *Fe* atoms by *Ti*, shows that the rate of change in the values $a(x)$, obtained experimentally, in the concentration area $0 \le x \le 0.01$ coincides with the rate of change in $a(x)$, obtained by calculation (similar slope of dependences 1 and 2 in Fig. 7*a*). Such consistency of $a(x)$ behaviour indicates that in *VFeSb* compound in this area *Fe* atoms are mainly displaced by *Ti* atoms.

At the same time, the nature of change in the calculated values of $a(x)$ in case of substitution of *Fe* atoms by *Ti* atoms in the concentration range $x > 0.01$ is basically different from the experimental results (Fig. 7*a*, curve 1). As long as the atomic radius of *Sb* ($r_{Sb} = 0.159$ nm) is the largest in *VFeSb* compound, increase in the values of $a(x)$ is only possible with replacement by *Ti* atoms of smaller atoms, namely either *Fe*, or *V* atoms ($r_V = 0.135$ nm), or these atoms simultaneously in different ratios. The result of calculation of a change in $a(x)$ values in concentration area $x > 0.01$ for the case when *Ti* atoms would replace only *V* atoms (Fig. 7*a*, curve 3), is close to the experimental results, however, does not coincide with it.

Thus, structural investigations allow asserting that in different concentration ranges *Ti* atoms simultaneously in different ratios occupy crystallographic positions of *Fe* and *V* atoms: in the concentration range $0 \le x \le 0.01$ *Ti* atoms to a larger extent occupy position of *Fe* atoms, and in the range $x > 0.01$ – position of *V* atoms.

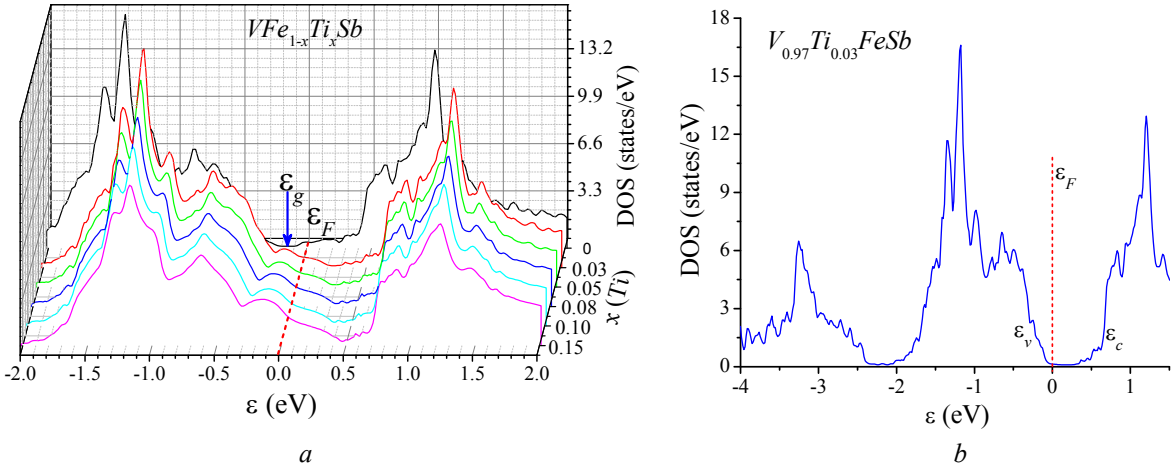

Fig. 8. Calculation of the electron density of states DOS for variants of ordered structure $VFe_{1-x}Ti_xSb$ (a) and $V_{0.97}Ti^{0.03}FeSb$ (b).

For a deeper insight into physical processes in a realized solid solution, the electron structure was calculated for both extreme cases, namely substitution in *VFeSb* compound of *Fe* and *V* atoms by *Ti* (Fig. 8). Thus, calculation of electron state density on the Fermi level $g(\varepsilon_F)$ for the case of substitution in *VFeSb* compound of *Fe* atoms by *Ti* shows that the values of $g(\varepsilon_F)$ increase only in the concentration range of $VFe_{1-x}Ti_xSb$, $0 \le x \le 0.15$, and the values of resistivity $\rho(x)$ calculated on this basis are reduced, which is typical of metal (Fig. 7*b*). This result, as is shown by the calculation of density of electron states DOS (Fig. 8*a*), is due to energy gap disappearance in the case of introduction into *VFeSb* compound of already the lowest concentration of *Ti* impurity ($x = 0.005$) by substitution of *Fe* atoms.

It is worth mentioning that the temperature and concentration dependence of electrical resistivity is studied in the range $0 \le x \le 0.02$, when conductivity has metallic type, and adding supposedly acceptor *Ti* impurity into *n*-type semiconductor *n-VFeSb* was unexpectedly accompanied

by a reduction of resistivity values. Exactly this result, namely increase in DOS on the Fermi level $g(\varepsilon_F)$ and, as a consequence, electric resistivity reduction, is provided by electron structure calculations for the case of substitution in *VFeSb* compound of *Fe* atoms by *Ti*. Hence, the analysis performed allows asserting that on introducing into *VFeSb* compound of *Ti* atoms in concentration area $0 \le x \le 0.02$ the latter to a larger extent displace *Fe* atoms, which is accompanied by energy gap disappearance, and the resulting material $Fe_{1-x}Ti_xSb$ is metal.

On the other hand, calculation of the electron density of states DOS for another extreme case has shown that substitution in *VFeSb* compound of *V* atoms by *Ti* atoms for atomic concentration an order higher ($x = 0.03$) does not destruct the semiconductor state of $V_{0.97}Ti_{0.03}FeSb$, and the Fermi level ε_F is in a forbidden gap near valence band ceiling (Fig. 8*b*). Exactly this result was revealed by the experimental studies of electric resistivity and the Seebeck coefficient at $x \ge 0.03$, when a change in resistivity values with temperature was of activation nature, and the Seebeck coefficient values were positive.

Thus, the analysis performed makes it possible to assert that on introducing into *VFeSb* compound of *Ti* atoms in concentration area $x \ge 0.03$, the latter to a larger extent displace *V* atoms, which is attended by the appearance of forbidden gap and generation in a crystal of acceptor-nature structural defects and the resulting material is a semiconductor. As long as studies of $VFe_{1-x}Ti_xSb$ have shown a simultaneous occupation by *Ti* atoms of positions of *V* and *Fe* atoms in different ratios depending on impurity concentration, to establish the exact proportion of such substitution is so far problematic.

Conclusions

Investigation of the process of introducing into *VFeSb* compound of *Ti* atoms has revealed a complex mechanism of a simultaneous substitution in different ratios depending on the concentration of impurity atoms of crystallographic position of *Fe* atoms, as well as *V* atoms. The result obtained makes it possible to predict behaviour of the kinetic characteristics of $VFe_{1-x}Ti_xSb$ and to obtain a material with high efficiency of thermal into electric energy conversion.

The work was performed in the framework of grant of Ministry of Education and Science of Ukraine, № 0112U001279.

References

1. L.I.Anatychuk, *Thermoelements and Thermoelectric Devices* (Kyiv: Naukova Dumka, 1979), 768 p.
2. V.A.Romaka, V.V.Romaka, and Yu.V.Stadnyk, *Intermetallic Semiconductors: Properties and Applications* (Lviv, Lvivska Polytechnika, 2011), 488 p.
3. T.M.Tritt, M.A.Sabramanian, Thermoelectric Materials, Phenomena, and Applications: A Bird's Eye View, *MRS Bulletin* **31**(3), 188-198 (2006).
4. G.S.Nolas, J.Poon, and M.Kanatzidis, Recent Developments in Bulk Thermoelectric Materials, *MRS Bulletin* **31**(3), 199-205 (2006).
5. V.V.Romaka, P.Rogl, L.Romaka, Yu.Stadnyk, A.Grytsiv, O.Lakh, and V.Krajovsky, Peculiarites of Structural Disorder in *Zr*- and *Hf*- Containing Heusler and Half-heusler Stannides, *Intermetallics* **35**, 45-52 (2013).
6. V.V.Romaka, L.Romaka, Yu.Stadnyk, V.Gvozdetskii, R.Gladyshevskii, N.Skryabina, N.Melnychenko, V.Hlukhyy, and T.Fässler, Interaction of Vanadium with Iron and Antimony at 870 and 1070 K, *Eur. J. Inorg. Chem*. 2012 (5), 2588–2595 (2012).

7. T.Roisnel, J.Rodriguez-Carvajal, WinPLOTR: a Windows Tool for Powder Diffraction Patterns Analysis, *Mater. Sci. Forum, Proc. EPDIC7* **378-381**, 118–123 (2001).
8. M.Schruter, H.Ebert, H.Akai, P.Entel, E.Hoffmann, and G.G.Reddy, First-Principles Investigations of Atomic Disorder Effects on Magnetic and Structural Instabilities in Transition-Metal Alloys, *Phys. Rev. B* **52**, 188-209 (1995).
9. V.L.Moruzzi, J.F.Janak, and A.R.Williams, *Calculated Electronic Properties of Metals* (NY: Pergamon Press, 1978), 348 p.
10. B.I.Shklovsky, A.L.Efros, *Electronic Properties of Doped Semiconductors* (Moscow: Nauka, 1979), 416 p.
11. Chenguang Fu, Hanhui Xie, Yintu Liu, T.J.Zhu, Jian Xie, X.B.Zhao, Thermoelectric Properties of *FeVSb* half-Heusler Compounds by Levitation Melting and Spark Plasma Sintering, *Intermetallics* 32, 39-43 (2013).

Submitted 02.10.14

I.I. Sanduleac

I.I. Sanduleac

Technical University of Moldova
168, Stefan cel Mare Ave.,
Chisinau, MD-2004, Moldova

THERMOELECTRIC POWER FACTOR OF TTT_2I_3 QUASI-ONE-DIMENSIONAL CRYSTALS IN THE 3D PHYSICAL MODEL

Tetrathiotetracene – Iodide organic crystals (TTT_2I_3) are very promising materials for thermoelectric applications. Due to their pronounced quasi-one-dimensionality, the density of states is increased in the direction of molecular chains and, respectively, the Seebeck coefficient is also increased. In addition, partial compensation of two main electron-phonon interactions leads to significant increase of carriers' mobility, ensuring high values of electrical conductivity. However, the mobility is diminished by the scattering on impurities and by the interchain interaction. Theoretically, it was predicted a power factor values up to 0.03 W/m·K^2 for crystals with increased purity. Initially, the estimations were performed in the frame of a simplified one-dimensional (1D) model, neglecting the weak interchain interaction. Further investigations have shown that for ultra-pure crystals this interaction becomes important and the calculations should be performed in the frame of a more realistic 3D model. In this paper, the electrical conductivity, Seebeck coefficient and the power factor for TTT_2I_3 organic crystals are presented in a 3D model. Also, the criteria of applicability of the simplified 1D model are estimated.

Key words: thermoelectricity, tetrathiotetracene iodide, interchain interaction, three-dimensional crystal model.

Introduction

In recent years, increasing attention has been paid to a search for new nanostructured thermoelectric materials, especially of organic type, with improved figure of merit *ZT*. The design and development of high-efficient thermoelectric devices which will be able to provide widespread conversion of low level heat into electricity and vice versa, represent a promising challenge for scientists. A big figure of merit requires that the given material have low thermal conductivity, increased electrical conductivity and high Seebeck coefficient. Different compounds with complex crystalline structure, like clathrates and skutterudites were reported to have very good thermoelectric figure of merit: $ZT \sim 1 \div 1.5$ at $T = 800 \div 1000$ K [1 - 3]. In these materials, the atoms are loosely bonded and the phonon scattering is increased, which leads to the diminution of thermal conductivity. In the same time, the electrical conductivity practically does not change. The Zintl compounds with large elementary cell, $Yb_{14}MnSb_{11}$, $Yb_{11}GaSb_9$, $Ca_{11}GaSb_9$ and $SrZnSb_2$, were reported to have low thermal conductivity due to the high fraction of low-velocity acoustical phonon modes [4].

High density of electronic states (DOS) may be achieved in low-dimensional systems, like superlattices, nanowires and quantum dots: while the system size decreases, the electronic DOS splits and becomes narrow [5]. This fact leads to very good thermoelectric properties: in Bi_2Te_3/Sb_2Te_3 superlattices $ZT \sim 2.5$ and in superlattices with quantum dots *PbTe*/*PbSe*, $ZT \sim 3$ at 600 K have measured [6, 7].

Nanostructured organic materials have the priority to join together the properties of low-dimensional system and those of multi-component material with much more diverse and complicated interactions. Also, their diverse properties are well tunable through molecular chemistry and doping procedures. Very interesting investigations are provided in last years, revealing promising results: in poly (3, 4-ethylenedioxythiophene) (PEDOT), a maximum $ZT = 0.42$ has been achieved by minimizing the total dopant volume [8]. The 2,7-Dialkyl [1] benzothieno [3,2-b] [1] benzothiophene derivatives have shown huge carrier mobility [10]. The implementation of organic nanostructured materials in the industry of thermoelectric devices has very good prospects, so as the production technology is not expensive and these materials are friendly with environment [9]. Theoretical investigations of thermoelectric properties of quasi-one-dimensional organic crystals of TTT_2I_3 [11, 16, 18] have demonstrated that the latter may be promising candidates for thermoelectric applications.

The aim of this paper is to model the electrical conductivity, Seebeck coefficient and the power factor of TTT_2I_3 organic crystals in the frame of a more complete 3D physical model and to determine the criteria, when the simpler 1D model may be used. Also, the possibilities to increase the thermoelectric figure of merit are analyzed.

Three-dimensional crystal model for TTT_2I_3 organic crystals

The basic structure of TTT_2I_3 organic crystal is primarily determined by the *TTT* molecules. The orthorhombic crystal structure consists of segregate donor *TTT* and acceptor iodine stacks. The interplanar distance of *TTT* molecules in stacks is identical and equals 3.32 Å, ensuring significant overlap of π-wave functions along stacks and an electrical conductivity of band type in this direction. The sulfur-sulfur distance on adjacent *TTT* molecules is 3.73 Å. This short sulfur contact provides a small interchain interaction which will be taken into account in this paper. The overlap of wave functions in transversal direction is small and the electrical conductivity is of hopping type. Parallel to the longitudinal ***b*** direction the iodine atoms lie in 4 columns per unit cell projection area [12, 13]. The elementary cell is very near to a parallelepiped. A Cartesian coordinate system is considered with the *x*-axis lying in the ***b*** direction and *y*, *z* – in the ***a*** and ***c*** directions, respectively.

The charge transport is of *p*-type: two *TTT* molecules give one electron to iodine chain. The last one has very low electrical conductivity. In the *x* direction, the overlap of HOMO of *TTT* molecules generates a narrow conduction band (~ 25 k_0T_0, T_0 is the room temperature; the transfer energy in *x*-direction is 0.16 eV). In the transversal directions there are two *TTT* molecules per lattice constant (*a* and *c*). The transfer energies in the *y* and *z* directions, w_2 and w_3, are estimated on the base of experimental measurements of the electrical conductivity in the transversal and longitudinal directions. Two parameters are introduced, d_1 and d_2, as it follows: $d_1 = w_2/w_1 = \sigma_{yy}/\sigma_{xx}$ and $d_2 = w_3/w_1 = \sigma_{zz}/\sigma_{xx}$. The internal structure of TTT_2I_3 crystals is strong quasi-one-dimensional ($d_1 \approx d_2 = 0.013$). Due to the property to allow non-stoichiometric compounds, the optimization of iodine content which determines the holes concentration, will generate more efficient TTT_2I_3 – based devices with improved thermoelectric figure of merit, *ZT* [12, 14].

The Hamiltonian of the system was described earlier [15, 16] for the 2D case. Now it has the form:

$$H = \sum_{\boldsymbol{k}} E(\boldsymbol{k}) a_{\boldsymbol{k}}^{+} a_{\boldsymbol{k}} + \sum_{\boldsymbol{q}} \hbar\omega_{\boldsymbol{q}} b_{\boldsymbol{q}}^{+} b_{\boldsymbol{q}} + \sum_{\boldsymbol{k},\boldsymbol{q}} A(\boldsymbol{k},\boldsymbol{q}) a_{\boldsymbol{k}}^{+} a_{\boldsymbol{k}+\boldsymbol{q}} (b_{\boldsymbol{q}} + b_{-\boldsymbol{q}}^{+}) + \sum_{n,j} IV_0 a_j^{+} a_j \delta(\boldsymbol{r}_n - \boldsymbol{r}_j). \quad (1)$$

Here the first term is for carriers (holes) in the tight binding and nearest neighbors' approximations. The energy of carrier measured from the extremum of the band has the form:

$$E(\boldsymbol{k}) = -2w_1\cos(k_x b) - 2w_2\cos(k_y a) - 2w_3\cos(k_z c), \tag{2}$$

where k_x, k_y, k_z are the projections of the quasi-wave vector $\boldsymbol{k}$.

The second term in (1) is the energy of longitudinal acoustic phonons:

$$\omega_{\boldsymbol{q}}^2 = \omega_1^2\sin^2(q_x b/2) + \omega_2^2\sin^2(q_y a/2) + \omega_3^2\sin^2(q_z c/2), \tag{3}$$

where ω_1, ω_2 and ω_3 are limit frequencies in the *x, y* and *z* directions, (q_x, q_y, q_z) are the projections of the quasi-wave vector $\boldsymbol{q}$, $\omega_2 \approx \omega_3 << \omega_1$.

As it was mentioned in [17], the cross transversal vibrations have negligible small effect and the simple 1D phononic spectrum is sufficient enough to describe thermoelectric properties.

The third term in (1) describes the electron-phonon interaction. It contains two main mechanisms. The first is determined by the variation of transfer integrals with respect to the intermolecular distances (the mechanism of the deformation potential). The second mechanism is similar to that of polaron: the lattice vibrations lead to the variation of the polarization energy of molecules surrounding the charge carrier.

The square module of the matrix element of electron-phonon interaction has the form:

$$\begin{aligned}|A(\boldsymbol{k},\boldsymbol{q})|^2 = 2\hbar/(NM\omega_{\boldsymbol{q}})\{w_1'^2[\sin(k_x b) - \sin(k_x - q_x, b) + \gamma_1\sin(q_x b)]^2 + \\ w_2'^2[\sin(k_y a) - \sin(k_y - q_y, a) + \gamma_2\sin(q_y a)]^2\} + w_3'^2[\sin(k_z c) - \sin(k_z - q_z, c) + \gamma_3\sin(q_z c)]^2\}.\end{aligned} \tag{4}$$

Here γ_1, γ_2 and γ_3 are the parameters describing the ratio of amplitudes of polaron-type interaction to the deformation potential one in the *x*, *y* and *z* directions [15], w_1', w_2' and w_3' are the derivatives of transfer energies with respect to intermolecular distance.

The last term in (1) describes the scattering of charge carriers on impurity centers, which are considered point-like, electric neutral and randomly distributed; *I* is the energy of interaction of a hole with the impurity center, V_0 is the volume of interaction region. The summation is provided on all the impurity centers in the base region of the crystal.

Transport phenomena

The scattering probability takes the form [15]:

$$W(\boldsymbol{k},\boldsymbol{k}') = 2\pi k_0 T/(\hbar^2\omega_q|A(\boldsymbol{k}+\boldsymbol{q},\boldsymbol{q})|^2)\delta[\varepsilon(k_x+q_x) - \varepsilon(k_x)], \tag{5}$$

where delta-function contains two main approximations – the scattering processes on phonons are considered elastic at room temperature and the energies w_2 and w_3 are neglected in comparison with w_1. The linearized kinetic equation is solved analytically and the expression for electrical conductivity takes the form:

$$\sigma_{xx}(0) = -\frac{8e^2w_1^2a^2}{k_0TV\hbar^2}\sum_{\boldsymbol{k}}\sin^2(k_x b)n_{\boldsymbol{k}}(1-n_{\boldsymbol{k}})/\sum_{\boldsymbol{k}'}W(\boldsymbol{k},\boldsymbol{k}')[1 - v_x(k_x')/v_x(k_x)], \tag{6}$$

where $v_x(k)$ is the projection of carrier velocity on *x* direction. The quasi-wave vector $\boldsymbol{k}$ has quasi-continuous spectrum and the summation may be replaced by integration over the entire Brillouin zone. In this order, the transport integrals are defined as:

$$R_n = abc\int_0^{\pi/a}dk_x\int_0^{\pi/b}dk_y\int_0^{\pi/c}dk_z\sin^3(k_x b)n_{\boldsymbol{k}}(1-n_{\boldsymbol{k}})\times \tag{7}$$

$$\frac{[\varepsilon - (1+d_1+d_2)\varepsilon_F]^n}{(1-\gamma_1\cos(k_x b))^2 + \frac{1}{4\sin^2(k_x b)}\{d_1^2[1+\gamma_2^2+2\sin^2(k_y a) - 2\gamma_2\cos(k_y a)] + d_2^2[1+\gamma_3^2+2\sin^2(k_z c) - 2\gamma_3\cos(k_z c)]\} + D_0}.$$

Here $\varepsilon = E(\boldsymbol{k})/2w_1$, $\varepsilon_F = E_F/2w_1$ are the energy of carriers and the Fermi energy in the unities of $2w_1$, $n_{\boldsymbol{k}}$ is the Fermi distribution function for carriers with energy (2), D_0 is the parameter describing the scattering of carriers on impurity centers:

$$D_0 = n_{im}^{3D} I^2 V_0^2 \frac{Mv_s^2}{4b^3 acw_1'^2 k_0 T}, \tag{8}$$

where n_{im}^{3D} is the concentration of impurity.

The expression for electrical conductivity takes the form:

$$\sigma_{xx} = \sigma_0 R_0, \text{ where } \sigma_0 = \frac{2e^2 w_1^3 v_{s1}^2 Mr}{\pi^3 abc\hbar (k_0 T)^2 w_1'^2}, \tag{9}$$

here $r = 4$ is the number of molecular chains through the transversal section of the elementary cell, v_{s1} is the sound velocity along the chains, M is the mass of TTT molecule and w_1' is the derivative of transfer energy with respect to intermolecular distance.

The Seebeck coefficient and the power factor are defined as:

$$S_{xx} = (k_0 / e)(2w_1 / k_0 T) R_1 / R_0. \tag{10}$$

Results and discussions

Numerical calculations for crystals with different degrees of purity were made in the frame of the 3D and 1D models. The crystal parameters are: $M = 6.5 \cdot 10^5 m_e$ (m_e is the free electron mass), $a = 18.35$ Å, $b = 4.97$ Å, $c = 18.46$ Å, $v_{s1} = 1.5 \cdot 10^3$ m/s, $w_1 = 0.16$ eV, $w_1' = 0.26$ eVÅ^{-1} [18]. The mean polarizability of TTT molecules, $\alpha_0 = 46$ Å^{-3} and this leads to $\gamma_1 = 1.7$. The parameters γ_2 and γ_3 are calculated from the relations $\gamma_2 = \gamma_1 b^5 / (a^5 d)$ and $\gamma_3 = \gamma_1 b^5 / (c^5 d)$. The values of lattice constants a and c are very close so it is possible to approximate $\gamma_2 \approx \gamma_3$.

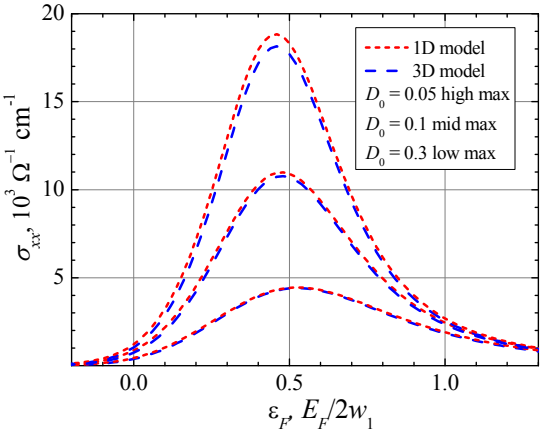

Fig. 1. Electrical conductivity as function of dimensionless Fermi energy for $D_0 = 0.3, 0.1, 0.05$.

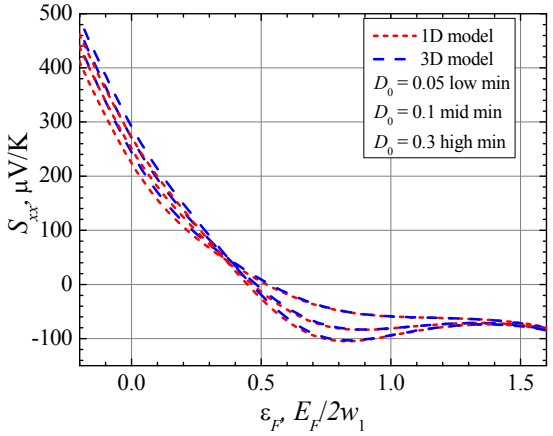

Fig.2. Thermopower S_{xx} as function of dimensionless Fermi energy.

In Fig. 1 the electrical conductivity in the x direction for p-type TTT_2I_3 crystals as function of dimensionless Fermi energy is presented for $D_0 = 0.3, 0.1, 0.05$. One can observe the pronounced quasi-one-dimensionality of the crystal: the influence of interchain interaction on the transport properties along the molecular chains is weak and becomes distinguishable only for high purity level. In the crystals synthesized from gaseous phase ($D_0 = 0.1$) it was reported $\sigma_{xx} \sim 10^4$ Ω^{-1}cm^{-1} [13]. The diminution of impurity center concentration, as it results from theory, leads to the increase of the

electrical conductivity and, consequently, of the power factor P_{xx}. Another way to improve P_{xx} is the optimization of the concentration of holes (by varying the concentration of iodine acceptors) due to the property of the crystal to allow non-stoichiometric compounds.

In Fig. 2 the Seebeck coefficient (S_{xx}) as function on dimensionless Fermi energy at room temperature is presented. For *p*-type crystals, S_{xx} takes positive values. It is observed the reverse situation-in order to increase P_{xx} it is needed to diminish the holes concentration, with respect to the stoichiometric one, since this procedure provides usually high Seebeck coefficient values. Seebeck coefficient is less sensitive to the interchain interaction. Experimentally it was reported $S = 36\ \mu V \cdot K^{-1}$ for crystals with $\sigma = 1200\ \Omega^{-1}cm^{-1}$ [12, 19].

In Fig. 3 the power factor (P_{xx}) as function of dimensionless Fermi energy is presented. The corrections induced by the realistic 3D model are ~10% when $D_0 = 0.05$ and $\varepsilon_F = 0.33$ (or stoichiometric concentration). For experimentally reported crystals with $D_0 = 0.1$ the deviations of the 3D model are smaller and the predictions made in the frame of 1D model are applicable. Recent researches in high conductive PEDOT: PSS/graphene composites have reported a power factor of $45.7\ \mu W \cdot m^{-1} \cdot K^{-2}$ [20].

As it is observed, the interchain interaction becomes important when the crystal purity is increased.

In order to determine the criterion, when the 1D approximation is still possible, new numerical calculations were also made for another set of ultra-pure crystals with $D_0 = 0.04$, 0.03, 0.02 and higher electrical conductivities not obtained yet. In the purest crystal the predicted conductivity achieves quite large values, of the order $3.5\times10^4\ \Omega^{-1}cm^{-1}$, (Fig.4). For stoichiometric crystals $\sigma_{xx} = 16$; 20; and $26\times10^3\ \Omega^{-1}cm^{-1}$ and the relative corrections induced by the new 3D model are: 6%, 7.3% and 9.5%, respectively.

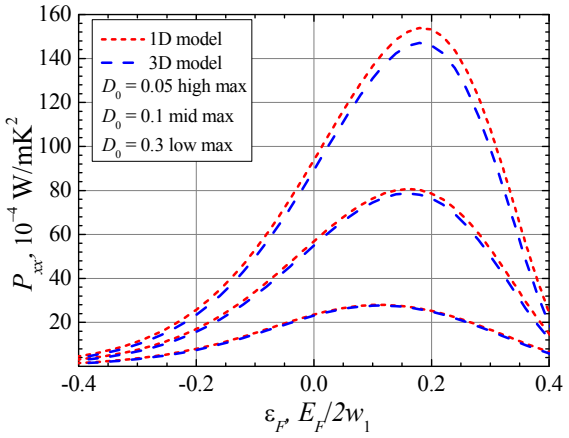

Fig.3. Power factor P_{xx} as function of dimensionless Fermi energy.

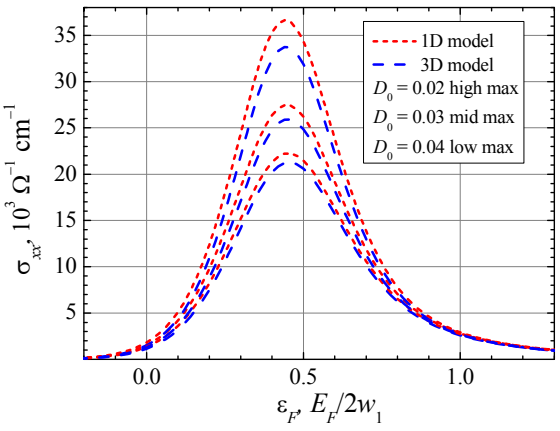

Fig. 4. Electrical conductivity σ_{xx} as function of dimensionless Fermi energy for purer crystals.

In Fig. 5 the Seebeck coefficient is presented as function of dimensionless Fermi energy (ε_F) for ultra-pure crystals. In this case, the differences between 3D and 1D model are more distinguishable, bud remains negligible.

The power factor is presented in Fig. 6. As well as the electrical conductivity, the power factor is sensible to the height of the relaxation time maximum, determined by partial compensation of above mentioned electron-phonon interactions. In the not very pure crystals with high impurity concentrations the relaxation time maximum and the carrier mobility is limited by scattering on impurities and the scattering on the nearest chains may be neglected.

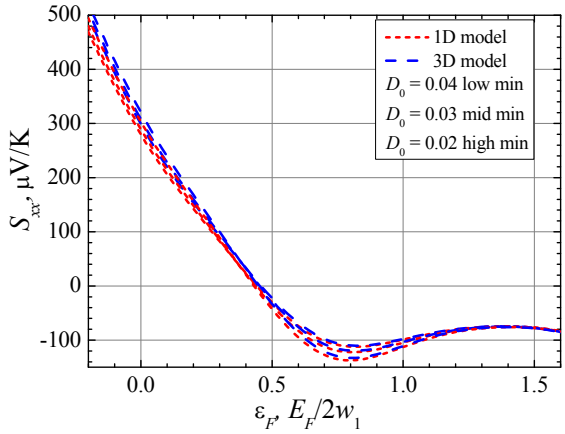

Fig.5. Seebeck coefficient as function of dimensionless Fermi energy for purer crystals.

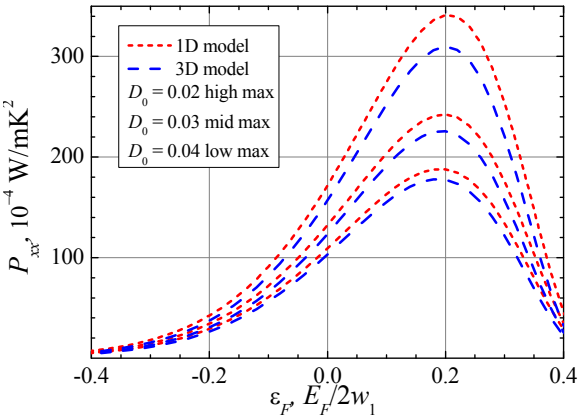

Fig.6. Power factor as function of dimensionless Fermi energy for purer crystals.

In this case the 1D model is a good approximation. In the purer crystals the scattering on the nearest chains begins to limit the height of relaxation time maximum and the mobility. The corrections for P_{xx} made by the new 3D model are: 11%, 13%, and 16%, for D_0 = 0.04, 0.03, 0.02 and stoichiometric crystals with $\varepsilon_F = 0.33$. Thus, for TTT_2I_3 crystals with electrical conductivity $\sigma_{xx} > 3\times10^4$ Ω^{-1}cm^{-1} it is necessary to apply the 3D physical model.

Conclusions

A more realistic 3D physical model for tetrathiotetracene-iodide organic crystals, TTT_2I_3 is developed by taking into account the interaction of nearest neighbors molecular chains. Two series of the parameter D_0 which describes the carrier scattering on impurities, are considered: for less pure and purer crystals. It is shown that the simplified 1D model is applicable for not very pure crystals, while for ultra-pure crystals with electrical conductivity $\sigma_{xx} > 3\times10^4$ Ω^{-1}cm^{-1}, the interchain interaction becomes significant and the 3D model it is needed to be used. When applying this new physical model for stoichiometric crystals, grown from vapor phase [13] with $D_0 = 0.1$, the predicted values for electrical conductivity, Seebeck coefficient and the power factor are: $\sigma_{xx} = 8.3\times10^4$ Ω^{-1}cm^{-1}, $S_{xx} = 68\times10^{-6}$ V/K, $P_{xx} = 39\times10^{-4}$ W/m·K^2. Maximum value of P_{xx} in this case achieves 80×10^{-4} W/m·K^2 or two times higher than in Bi_2Te_3, the widest used commercial material, very good result.

Acknowledgements

The author expresses gratitude to A. Casian for valuable guidance and advices, and acknowledges the financial support of EU Commission FP7 program under the grant no. 308768.

References

1. B. C. Sales, D. Mandrus, R.K. Williams, Filled Skutterudite Antimonides: A New Class of Thermoelectric Materials, *Science* **272**, 1325-1328, 1996.
2. G. S. Nolas, D. T. Morelli, T. M. Tritt, A Phonon-Glass-Electron Crystal Approach to Advanced Thermoelectric Energy Conversion Applications, *Annu. Rev. Mater. Sci.* **29**, 89, 1999.
3. G. S. Nolas, J. L. Cohn, G. A. Slack, S. B. Schujman, Semiconducting Ge clathrates: Promising candidates for thermoelectric applications, *Appl. Phys. Lett.* **73**, 178, 1998.

4. E. S. Toberer, A. F. May, G. J. Snyder, Zintl Chemistry for Designing High Efficiency Thermoelectric Materials, *Chem. Mater.* **22**, 624, 2010.
5. L. D. Hicks, M. S. Dresselhaus, Effect of quantum-well structures on the thermoelectric figure of merit, *Phys. Rev.* **47**, 12727, 1993.
6. R. Venkatasubramanian, E. Siivola, T. Colpitts, B. O'Quinn, Thin-film thermoelectric devices with high room-temperature figures of merit, *Nature* **413**, 597, 2001.
7. T. C. Harman, P. J. Taylor, M. P. Walsh, B. E. LaForge, Quantum Dot Superlattice Thermoelectric Materials and Devices, *Science* **297**, 2229, 2002.
8. G. Kim, L. Shao, K. Zhang, K. P. Pipe, Engineered doping of organic semiconductors for enhanced thermoelectric efficiency, Nat. Mater. **12**, 719, 2013.
9. Q. Zhang, Y. Sun, W. Xu and D. Zhu, Organic Thermoelectric Materials: Emerging Green Energy Materials Converting Heat to Electricity Directly and Efficiently, *Adv. Materials*, **31**, 2014.
10. W. Shi, J. Chen, J. Xi, D. Wang, and Z. Shuai, Search for Organic Thermoelectric Materials with High Mobility: The Case of 2,7-Dialkyl[1]benzothieno[3,2-b][1]benzothiophene Derivatives, *Chem. Mater*. **26**, 2669, 2014.
11. A. I. Casian, I. I. Sanduleac, Organic Thermoelectric Materials: new opportunities, *J. of Thermoelectricity*, **3**, 2013.
12. L. Isett, Magnetic susceptibility, electrical resistivity, and thermoelectric power measurements of *bis*(tetrathiotetracene)-triiodide, *Phys.Rev*. **B18**, 1978.
13. B. Hilti, C. Mayer, Electrical Properties of the Organic Metallic Compound bis (Tetrathiotetracene)-Triiodide, $(TTT)_2I_3$, *Helvetica Chimica Acta*, **61**(40), 501, 1978.
14. G. Kim, L. Shao, K. Zhang, K. P. Pipe, Engineered doping of organic semiconductors for enhanced thermoelectric efficiency, *Nat. Mater*. **12**, 719, 2013.
15. A. I. Casian, I. I. Sanduleac, Effect of Interchain Interaction on Electrical Conductivity in Quasi-One-Dimensional Organic Crystals of Tetrathiotetracene-Iodide, *J. of Nanoelectronics and Optoelectronics*, **7**, 706-711, 2012.
16. I. I. Sanduleac, A. I. Casian, J. Pflaum, Thermoelectric Properties of Nanostructured Tetrathiotetracene Iodide Crystals in a Two-Dimensional Model, *Journal of Nanoelectronics and Optoelectronics,* **9**, 247-252, 2014.
17. I. I. Sanduleac, Effect of 2D phonon spectrum on the electrical conductivity and thermopower of tetrathiotetracene-iodide crystals, *MJPS*, in press, 2014.
18. A. I. Casian, J. G. Stockholm, V. Dusciac and V. Nicic, Low-Dimensional Organic Crystal Tetrathiotetracene–Iodide as Thermoelectric Material: Reality and Prospects, *J. Nanoelectronics and Optoelectronics*, **4**, 95, 2009.
19. P.M. Chaikin, G. Gruner, I.F. Shchegolev and E.B. Yagubskii, Thermoelectric power of $TTT_2I_{3+\delta}$, *Solid State Communications*, **32**, 1211, 1979.
20. D. Yoo, J. Kim, J. H. Kim, Direct synthesis of highly conductive poly(3,4-ethylenedioxythiophene):poly(4-styrenesulfonate) (PEDOT:PSS)/grapheme composites and their applications in energy harvesting systems, *Nano Research*, **7**, Issue 5, 717-730, 2014.

Submitted 29.08.14

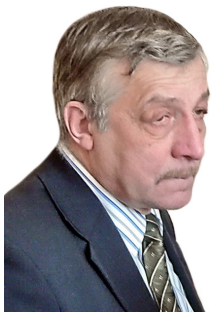

G. A. Arakelov

G. A. Arakelov

State Scientific Center of the Russian Federation
JSC "NPO "Orion",
46/2, Enthuziastov Sh., Moscow, 111123, Russian Federation

SOME PROBLEMS OF THERMOELECTRIC THERMAL STABILIZATION OF MICROBOLOMETRIC ARRAYS OF INFRARED RANGES

Technical features of devices based on uncooled microbolometric arrays of infrared ranges are considered. A thermopile is shown to be the best tool for precision thermal stabilization of microbolometric arrays. Construction criteria for selection of a thermopile for devices with such architecture are defined.

Key words: microbolometric array, thermopile, thermostabilization.

Introduction

Analysis of modern high-technology branches of science and engineering shows that they have been really implemented in many kinds of new enginery. They primarily include developments of systems of deep-space thermal imaging of ballistic missile launches, thermal imaging systems of tank and aircraft fire control, high-precision missile and artillery weapons with laser guidance, antiballistic missile systems, multispectral anti-aircraft complexes, optic and fiber-optic data-transmission systems, developments of laser range finding devices, especially at eye-safe wavelength, etc. The role of optics and infrared equipment in such weapons is fundamental, since precisely optico-electronic systems determine the operational range, energy consumption, weight and dimensions of defence complexes. In some instances the task simply cannot be solved without the use of devices recording the intrinsic thermal radiation of a real target, for instance, with the availability of numerous decoys or radio interferences making radiolocation inefficient. Therefore, of particular importance are fully passive infrared systems that do not radiate and, hence, cannot be detected by means of radioelectronic intelligence and suppression [1].

Infrared radiation photodetectors are the key elements of almost any optico-electronic system. In the majority of cases the efficient operation of these devices requires cooling of their semiconductor photosensitive elements, assuring the advantage of optical generation of charge carriers over heat spreaders [2]. In so doing, one of the most in-demand cooling methods for the above purposes is thermoelectricity enabling to achieve the necessary detectability values of photodetector mainly in the medium-range (3-5 μm) spectral region. At the same time, it should be noted that further development of solid-state photoelectronics engineering in recent years has been largely dependent on mass introduction into equipment of microbolometric arrays (MBA) for infrared range of 8-14 μm [3]. The operating principle of MBA is as follows: optical radiation coming to MBA is absorbed and heats sensitive element that has sufficiently high temperature coefficient of resistance. Resistance change due to heating is converted into voltage, i.e. to recorded signal.

A distinguishing design feature of these devices is, as a rule, the absence of any cooling system and, therefore, thermal imaging module has lower energy consumption, dimensions and mass.

Production of MBA based on vanadium or silicon oxide is considerably cheaper compared to cooled photodetectors. At the same time, using MBA necessitates account of certain factors that predetermines the presence in them of a precision MBA temperature controller based on a single-stage thermopile. However, due to lack of scientific and technical publications on this subject matter there is certain information gap with regard to validity and necessity of using thermopile for the above purpose, as well as the specificity of devices with their application. It is precisely these aspects that the present paper is concerned with.

Technical features of devices

Structurally, MBA are a set of microbridges. Each of them rests on a silicon plate by means of two dielectric supports with a minimal thermal conductivity. Such MBA arrangement assures its higher thermal resistance relative to the substrate. For the same purpose, MBA are mounted in evacuated packages. This prevents leakage from MBA of stored thermal energy of absorbed IR-radiation [3]. Strictly speaking, to be operated, MBA need not be cooled relative to ambient temperature. At the same time, rather rigid requirements are imposed on the stability of MBA operating temperature T_s. These requirements are governed by the optics of a device where it is used, the MBA area, its temperature coefficient of resistance and the value of thermal bonding to substrate, as well as by other factors [4].

Calculations performed by the author show that for MBA based on vanadium film to record a change in observed object temperature (ΔT_{OB}) by $1.5 \cdot 10^{-1}$ K is only possible with the accuracy of its thermal stabilization (ΔT_B) on the level of $\pm\, 5 \cdot 10^{-3}$ K.

The accuracy of temperature control in the range of ± 5–10 mK is governed by the fact that the increment of bolometer temperature ΔT_B with a change in object temperature ΔT_{OB} corresponds to expression:

$$\Delta T_B(\Delta T_{OB}) \approx R_T K_{\Delta\lambda} \mu_{\Delta\lambda} \Delta T_{OB} A_B (\partial M_{\Delta\lambda}/\partial T_{OB})/4F_{\#}^2,$$

where R_T is bolometer thermal resistance, K/W;

$K_{\Delta\lambda}$ is effective value of microbolometer radiation absorptivity in the spectral range of $\Delta\lambda$;

$\mu_{\Delta\lambda}$ is effective value of lens transmission factor in the same range;

A_B is microbolometer area, cm^2;

$M_{\Delta\lambda}$ is power density of object radiation in the range of wavelength $\Delta\lambda$, W/cm^2;

$F_{\#}$ is inverse aperture of the objective.

In the case in hand the values appearing in the expression have the following guide values: $R_T \le 1 \cdot 10^7$ K/W; $K_{\Delta\lambda} \approx 0.7$; $\mu_{\Delta\lambda} \approx 1$; $A_B \approx 3.5 \cdot 10^{-5}$ cm^2; $\partial M_{\Delta\lambda}/\partial T_{OB} \approx 2.6 \cdot 10^{-4}$ $W \cdot cm^{-2} \cdot K^{-1}$ ($\Delta\lambda$ = 8–14 μm); $F_{\#} = 0.7$.

Then, at $\Delta T_{OB} = 0.15$ K the accuracy of thermal stabilization ΔT_B (0.15) $\le 5 \cdot 10^{-3}$ K.

Thermoelectric thermal stabilization of MBA

Generally speaking, thermal stabilization devices are divided into passive and active. Passive devices do not comprise any sources of heat or cold, hence the impossibility of high accuracy of thermal stabilization over a wide range of ambient temperature T_0.

On the contrary, active devices comprise the sources of heat or cold (separately or together). In so doing, depending on the level of T_s active thermal stabilization with change in temperature T_0 from T_0^{min} to T_0^{max} can be of three types.

Low-temperature thermal stabilization, when $T_s<T_0^{min}$, is characterized by the presence of surplus heat and is of limited use in semiconductor instrument making.

Normal thermal stabilization, when $T_0^{min} < T_s < T_0^{max}$, is distinctive in that at different times one needs either to deliver heat or remove it. This method is most widely used at $T_s = 283—298$ K.

High-temperature thermal stabilization when $T_s > T_0^{max}$ requires constant delivery of heat to the desired object.

Due to the fact that for MBA $T_s = 283—298$ K, only normal thermal stabilization is discussed hereinafter. With regard to this factor it must be admitted that thermopile is the best tool for precision thermal stabilization of MBA. Being simultaneously possible source of heat and cold, thermopile offers a variety of technical advantages, including small dimensions, mass, energy consumption and response time, design simplicity, high reliability, noise-free operation, absence of microphonic effect, independence of attitude in space, etc. The above complex of distinctions for thermopile is quite trivial, making it most preferable for the attainment of the above goal [5].

Active normal thermal stabilization by means of a thermopile can be implemented by one of the following methods:

- purely thermoelectric, when heating and cooling are assured by the respective polarity of thermopile supply voltage;
- thermoelectric cooling and electric heating;
- thermoelectric cooling or heating with additional electric heating.

The second method is used for thermal stabilization of objects in a wide temperature range with the value of T_s close but lower than T_0. Energetically it is inferior to the first method and structurally it is more complicated.

The third method is a combination of the above. It is intended for thermal stabilization under conditions typical of the second method with a forced heating mode. Energetically, as compared to other methods, it is less beneficial, and structurally it is similar to the previous one.

Among the methods of active normal thermal stabilization, with common requirements to it, purely thermoelectric method is optimal. This thesis is also valid in the case of MBA devices.

Thermopile selection in such and similar devices is governed both by the given level MBA thermal stabilization and by its geometric dimensions. At the same time, in such devices, as a rule, it is necessary to assure in addition high degree of thermal stabilization uniformity along MBA area ($\le 2\cdot10^{-2}$ K). The same rigid requirement dictates, accordingly, the design and general architecture of thermopile. It is apparent that thermopile should comprise an increased amount of thermoelements with a relatively high packing, i.e. with minimal distances between them. In so doing, on the working site of thermopile a large amount of closely spaced discrete sources of cold or heat is arranged, which objectively contributes to implementation of technical challenge set. Further leveling of the temperature field provides for manufacture of thermopile working site of high thermal conductivity ceramic material, for instance, beryllium oxide or aluminum nitride. In certain cases for the same purpose use is made of a copper plate mounted on thermopile working site.

The necessary accuracy of MBA temperature control is realized by means of appropriate element base and hardware, including temperature sensor. In [4], the results of testing the elaborated system of MBA thermal stabilization based on a single-stage thermopile that provided for selection of T_s in the range of 283–298 K to an accuracy of $\pm 2.5\cdot10^{-3}$ K at $T_0 = 288–303$ K. This data is in good agreement with the above formulated technical requirements to MBA thermal stabilization systems.

Conclusions

The present paper is not intended to be a comprehensive and detailed presentation of all the problems with which the developers of infrared engineering are faced when creating MBA thermal stabilization systems. The author has just indicated some key aspects to be taken into account without fail and plans to continue publications on this subject matter.

References

1. V.P.Ponomarenko, A.M.Filachev, Infrared Engineering and Electronic Optics. Formation of Research Areas (1946-2006) (Moscow: Fizmatkniga, 2006), 336 p.
2. L.I.Anatychuk, L.N.Vikhor, Limits of Thermoelectric Cooling for Photodetectors, *J.Thermoelectricity* 5, 62-68 (2013).
3. A.M.Filachev, I.I.Taubkin, and M.A.Trishenkov, *State-of-the-Art and Main Trends of Current Photoelectronics Development* (Moscow: Fizmatkniga, 2010), 128 p.
4. A.B.Kozlov, Yu.V.Kulikov, V.G.Malyarov, and I.A.Khrebtov, Temperature Stabilization System of Uncooled Microbolometric Array, *Optical Journal* 68(1), 70-73 (2001).
5. G.A.Arakelov, Activity Progress and Prospects for the Development of Thermoelectric Cooling for Photoelectric Semiconductor Radiation Detectors, *Applied Physics* 6, 78-84 (2002).

Submitted 21.10.14

Yu.M. Lobunets

Yu.M. Lobunets

Institute of Thermoelectricity, 1, Nauky Str.,
Chernivtsi, 58029, Ukraine

THE APPLICATION POTENTIAL OF THERMOELECTRICITY IN POWER ENGINEERING

The possibilities of using thermoelectric generators for conversion of transit heat flows in the industrial and power equipment are considered. The efficiency of such a scheme is shown to be 100%. The application potential of such TEG is outlined.

Key words: thermoelectric generator, low-grade heat source.

Introduction

The use of energy of low-grade heat sources is one of the central problems in the development of modern power engineering. Thermal waste from industrial enterprises, as well as natural heat accumulators (atmospheric air, water), are regarded as a significant additional source of energy that allows conserving conventional kinds of fuel whose resources are limited. Thermoelectric energy conversion is considered among possible technologies that allow using low-grade heat sources. It is noteworthy that thermoelectric method of energy conversion has peculiarities which allow raising the question of energy efficiency increase in basically different manner as compared to conventional technologies. I mean the possibilities of TEG application for conversion of transit heat flows into electric energy. The term “transit heat flow” in our case is related to flows in heat-exchange devices available in the majority of industrial and energy technologies. Our construction of heat-exchange type TEG put forward in [1] makes it possible to use a thermoelectric converter as a component of heat-exchange equipment without violating the basic functions of the latter. Part of the heat flowing in the heat exchanger is converted into electric energy. With regard to the fact that only this part of heat is eliminated from the main technological process, and the remaining heat finds useful application, as intended, it can be considered that the efficiency of thermal into electric energy conversion for such a scheme is 100%.

This paper deals with examples of possible use of such schemes, gives an estimate of technical and economic restrictions and application potential of heat-exchange type TEG.

Construction of heat-exchange type TEG

The scheme of the above TEG is similar to that of a plate-type heat exchanger where heat carrier flows exchanging heat are separated by metal plates with channels for passage of liquid formed between them by means of special spacers. The necessary number of plates forms a compact package that assures given power of heat exchanger (Fig.1). In the case of a TEG the function of plates is performed by thermopiles consisting of thermoelectric modules. Thus, a TEG can serve as a heat exchanger where part of heat flow passing between heat carriers is converted into electric energy.

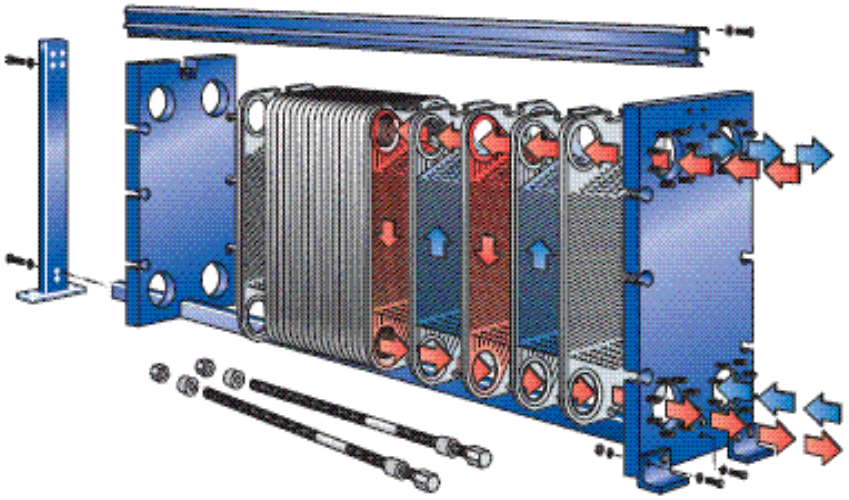

Fig.1. Plate-type heat exchanger [2].

Certainly, additional thermal resistance in the form of thermoelements deteriorates heat exchange characteristics of the device as a result of which its necessary size is increased. However, the device acquires new properties whose advantages can compensate the losses. To reveal the conditions whereby the scheme being analyzed allows achieving efficient solutions, it is necessary to consider technical and economic performance of TEG both from the standpoint of electric energy generator and from the standpoint of heat exchange equipment.

Comparison of characteristics of heat exchanger and its equivalent TEG

By comparison, let us take the simplest and common example, namely water heating in hot water supply system. Standard heat exchanger of AquaFlow heat supply station manufactured by Alfa Laval has the following characteristics [2]:

Table 1

Characteristics of the heat supply station

Thermal power, kW	Hot water flow rate, kg/s	Cold water flow rate, kg/s	Hot water temperature, input/output, °C	Cold water temperature, input/output, °C	Surface area, m^2	Heat-transfer coefficient, W/m^2K
1200	5.5	6.5	110/57	10/55	2.1	5376

The main function of this apparatus is to heat water from 10°C to 55°C in the amount of 23.4 m^3 per hour. For this purpose, about 1200 kW-hour of thermal energy is spent for transit through heat exchanger plates from heating to cooling water. Characteristics of heat-exchange type TEG performing this function will be calculated by a procedure set forth in [3], taking as the input parameters the data listed in Table 1, as well as the following properties of thermoelectric modules:

- thermoelectric figure of merit of thermoelement material - 0.0029 K^{-1};
- thermoelement height - 0.05 cm;
- thermopile size – 50x100 cm;
- the height of channels between thermopiles – 0.5 cm.

The number of thermopiles in TEG will be selected keeping in mind the necessity of heating given water volume from 10°C to 55°C, noting that generator-heat exchanger channels are connected in series. The results of calculations are presented in Fig. 2 from which it is evident that in the case under study heat carrier reaches given temperature with the use of 30 thermopiles. TEG power in this case is equal to 33 kW, that is, about 2.75% of heat flow is converted into electric energy.

Characteristics of TEG according to Table 1 are given in Table 2.

As it follows from comparison of the data in Table 1 and Table 2, due to essential reduction of heat exchange coefficient, the heat exchange surface in TEG has increased approximately 7 fold. However, in reality such a TEG will have the approximate dimensions 50x100x35 cm, which is little different from the dimensions of the substituted heat exchanger. The main point which determines the advisability of using such a TEG is the cost of electric energy produced by it. A preliminary idea of the economic expediency of this scheme can be obtained from the estimation of the unit cost of installed TEG power as compared to other sources of electric energy. As the basis for comparison we will take the data given in [4], Fig.3.

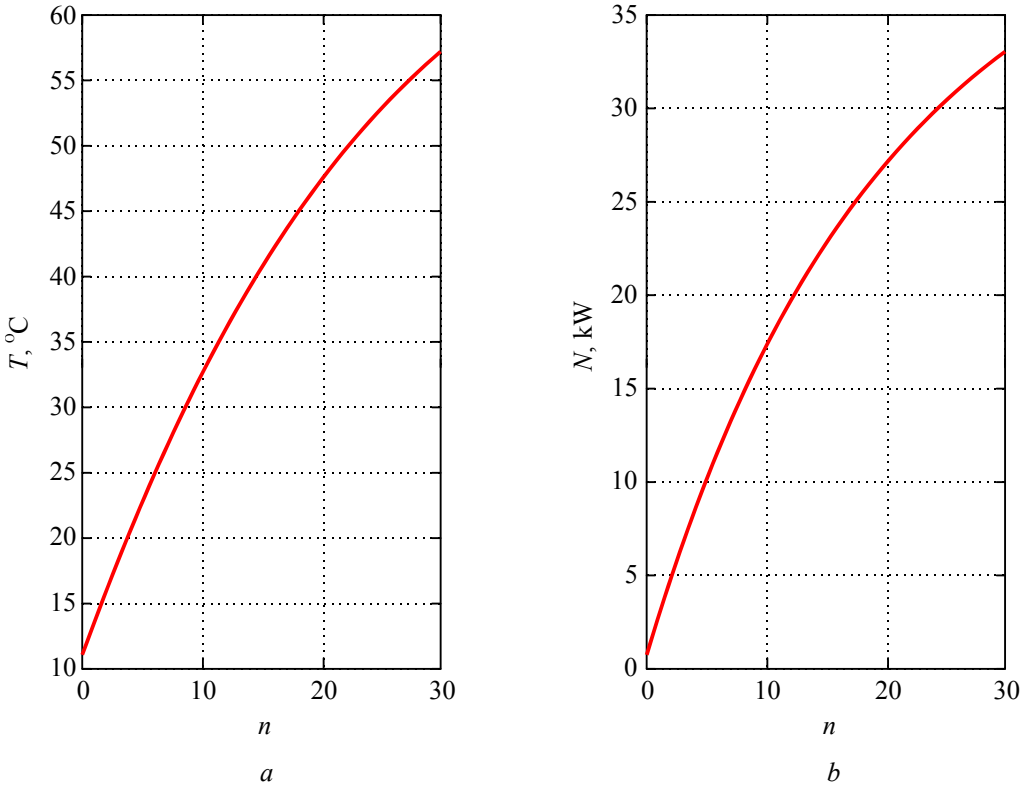

Fig. 2. Dependences of cold water temperature T (a) and TEG power N (b) on the number of thermopiles in TEG, n.

Table 2

Characteristics of TEG

Electric power of TEG, kW	Hot water flow rate, kg/sec	Cold water flow rate, kg/sec	Hot water temperature, input/output, °C	Cold water temperature, input/output, °C	Surface area, m^2	Heat transfer coefficient, W/m^2 °C
33	5.5	6.5	110/64	10/57	15	979

To estimate the cost of TEG, let us consider the cost of its components and the approximate cost of works. Despite the uncertainty of such estimation, it can give certain idea on the order of cost of installed TEG power in kW. Thus, the basic components of TEG are:

Table 3

Basic components of TEG

Name	Cost	Quantity in TEG	Amount
Thermoelectric material	300 $US/kg	50 kg	15000 $US
Ceramic heat spreaders	0.03 $US/cm^2	30 m^2	9000 $US
Connecting plates (copper)	12 $US/kg	120 kg	1440 $US
Metal plates (titanium)	50 $US/kg	27 kg	1350 $US
Heat exchanger spacers	5 $US/pcs	32 pcs	160 $US
			27 450 $US

The cost of TEG assembling works can be appraised at approximately the same sum which totals 1700 $US/kW. This figure correlates well with the data for the basic sources of electric energy given in Fig. 4. Even if in reality it will double (which is possible, though the above estimate is rather exaggerated), nevertheless all capital outlays in TEG are well within the range of prices for the existing sources of electric energy (it should be also noted that there is a considerable reserve of increasing the economic efficiency of TEG due to optimization of its regimes and parameters).

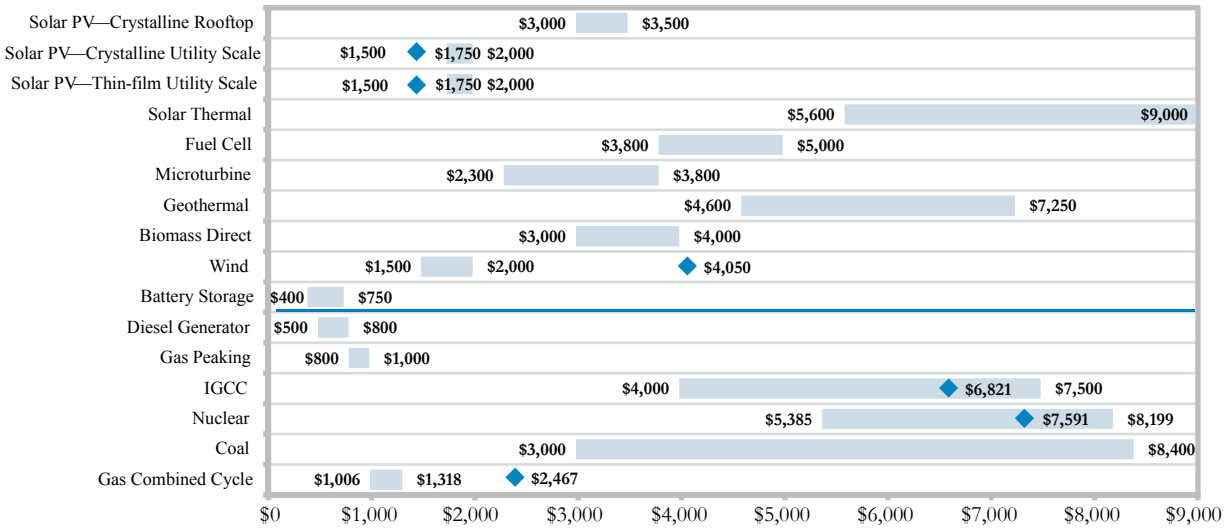

Fig. 3. Capital outlays on the unit of installed power $US/kW [4].

As regards the forecast cost of electric energy, the scheme of TEG in question offers the undeniable advantages due to high efficiency of thermal energy use. It can be estimated as not exceeding the cost of electric energy of the most efficient conventional sources using similar fuel (in this case gas), such as combined-cycle electric generating plants. According to [4], the range of electric energy cost for such sources is 0.052...0.096 $US/kW-hour.

Certainly, the application potential of TEG in power engineering goes beyond the example discussed. There are many opportunities of their use in various technological processes. One of the most large-scale can be the use of heat-exchange type TEG in the technological cycle of thermal power plants. For instance, in low-pressure water heaters [5] assuring water heating in steam-power cycle from 35°C to 150 °C. An introduction of such TEG can assure additional generation of 3...5% of

electric energy, that is, the efficiency of electric power station will increase almost by 10%. Such prospects look fantastic, but there are all technical and economic prerequisites for that.

Conclusions

The analysis performed above offers exciting possibilities of heat-exchange type TEG application for using transit heat flows in industry and power engineering. Development of this line primarily requires creation of TEG equipment unified with standard heat exchangers which will make possible a widespread introduction of this technology.

References

1. Yu.M.Lobunets, Thermoelectric Generator, *Patent of Ukraine №8357* of 27.08.2013.
2. http://www.alfalaval.com/
3. Yu.M. Lobunets, Performance Analysis of Heat-Exchange Type Thermoelectric Generator, *J.Thermoelectricity* **1**, 56 – 63 (2014).
4. Lazard's Levelized Cost of Energy Analysis – Version 7.0, August 2013. – http://gallery.mailchimp.com/ce17780900c3d223633ecfa59/files/Lazard_Levelized_Cost_of_Energy_v7.0.1.pdf
5. http://energoworld.ru/library/poverhnostnyie-podogrevateli-nizkogo-davleniya-tiporazmeryi-i-harakteristiki/

Submitted 11.09.14

L.I.Anatychuk

L.I. Anatychuk[1,2], R.R. Kobylianskyi[1,2]

[1]Institute of Thermoelectricity of the NAS and MES
Ukraine, 1, Nauky Str.,
Chernivtsi, 58029, Ukraine;
[2]Yu. Fedkovych Chernivtsi National University, 2,
Kotsyubinsky Str.,
Chernivtsi, 58000, Ukraine

R.R.Kobylianskyi

INCREASE IN THERMAL GENERATOR EFFICIENCY WITH THE USE OF HUMAN THERMAL ENERGY IN DYNAMIC MODES

This paper studies increase of thermoelectric generator efficiency in transient unsteady conditions due to a thermal contact between the surface area of human body and the thermopile. For such investigations, a computer method for determination of the energy characteristics of thermal generator in unsteady thermal conditions is developed. A physical model for such processes with the respective computer simulation is built. The specific feature of this model is a substitution of a heat sink that extracts heat from a thermopile by a heat accumulator. A mathematical description is performed and a computer model is created on the basis of object-oriented programming.

The case study of a model for a thermopile of Bi-Te based material with a contact area 0×10 mm and a copper heat accumulator is presented. The optimal length of module legs is determined as 2 ÷ 2.5 mm and heat accumulator length – as 5 ÷ 10 mm. In so doing, the thermopile during 20 s generates about 25 mJ of electric energy which is quite sufficient for the operation of electronic medical thermometer.

Key words: thermoelectric microgenerator, dynamic mode, computer simulation.

Introduction

Thermoelectric microgenerators using human heat are promising for power supply to all kinds of low-power electronic equipment [1-11]. In [12] it was established that for power supply to short-life devices one should use thermoelectric microgenerators in dynamic operating modes, since under certain conditions such modes yield higher electric power than in steady-state modes. The use of short-life transient operating modes allows doing away with cumbersome heat sinks that are the major obstacle when creating efficient and compact electric power sources operated by human heat.

Therefore, the purpose of this work is to develop computer methods for simulation of thermal generator operation in transient thermal modes and to use them for the optimization of specific design variants of such generators.

Physical model

According to a physical model (Fig.1), an area of human biological tissue is a structure consisting of three skin layers (epidermis 1, dermis 2, subcutis 3) and internal tissue 4 and characterized by thermal conductivity κ_i, specific heat C_i, density ρ_i, blood perfusion rate ω_{bi}, blood

density ρ_b, blood heat capacity C_b and specific heat release q_{meti} due to metabolic processes (Table 1). The respective biological tissue layers 1-4 are regarded as the bulk sources of heat q_i where:

$$q_i = q_{meti} + \rho_b \cdot C_b \cdot \omega_{bi} \cdot (T_b - T), \quad i = 1..4. \tag{1}$$

The geometric dimensions of each such layer are a_i, b_i and l_i. The temperatures at the boundaries of the respective biological tissue layers are T_1, T_2, T_3 and T_4. The thermophysical properties of human biological tissue are given in [12-17].

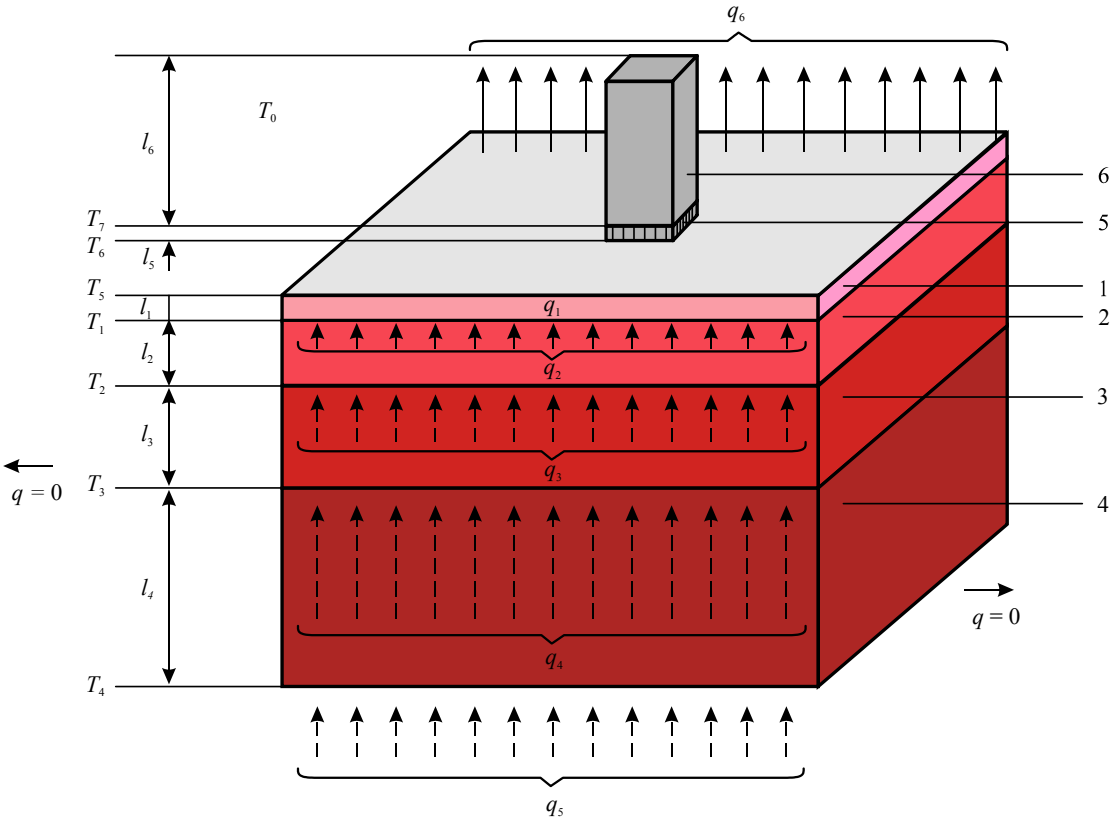

Fig. 1. A physical model of biological tissue with a thermoelectric microgenerator and a heat accumulator: 1 – epidermis, 2 – dermis, 3 – subcutis, 4 – internal tissue, 5 – thermoelectric microgenerator, 6 – heat accumulator.

A thermoelectric microgenerator 5 is an equivalent rectangular bar with dimensions a_5, b_5, l_5, characterized by thermal conductivity corresponding to microgenerator thermal conductivity κ.

The thermoelectric microgenerator 5 with contact surface temperature T_6 is located on the surface of biological tissue (epidermis 1) with temperature T_5. The thermoelectric microgenerator 5 is in a state of heat exchange with a bar-shaped heat accumulator 6 of high thermal conductivity material with geometric dimensions a_6, b_6, l_6. The contact surface temperature is T_7.

Free surface of skin area (epidermis 1) is in a state of heat exchange with the environment with temperature T_0 which is taken into account by heat exchange coefficient α. The rest of free surfaces of thermoelectric microgenerator 5 and bar 6 are adiabatically isolated. The specific heat flux from the free skin surface is q_6, and the specific heat flux from the internal parts of human body is q_5. Skin heat exchange due to radiation and perspiration is disregarded.

As long as a physical model is an area of a four-layered biological tissue, with identical biochemical processes occurring in adjacent layers, it can be assumed that there is no heat overflow through the lateral surface of biological tissue ($q = 0$).

Mathematical description of the model

As long as this research aims at studying the dynamics of physical processes in a thermoelectric microgenerator since the moment it is brought into a thermal contact with the skin surface, one must know the steady-state distribution of temperature in biological tissue in the absence of a microgenerator on its surface. Such temperature distribution should be chosen as the initial conditions in biological tissue in the process of thermal interaction between thermoelectric microgenerator and biological tissue. This, in turn, means that the research should be performed in two steps. At the first step it is necessary to find the steady-state temperature distribution in biological tissue in the absence of a microgenerator on its surface. At the second step – the dynamic temperature distribution in biological tissue and the thermoelectric microgenerator and bar 6 located on its top, assuming as the initial conditions for biological tissue the temperature distribution found at the first step.

A general equation of heat exchange in biological tissue is as follows [12-17]:

$$\rho_i \cdot C_i \cdot \frac{\partial T}{\partial t} = \nabla(\kappa_i \cdot \nabla T) + \rho_b \cdot C_b \cdot \omega_{bi} \cdot (T_b - T) + q_{meti}\,, \tag{2}$$

where $i = 1..4$ are corresponding layers of biological tissue,

ρ_i is the density of corresponding biological tissue layer (kg/m^3),

C_i is specific heat of corresponding biological tissue layer (J/kg·K),

ρ_b is blood density (kg/m^3),

C_b is specific heat of blood (J/kg·K),

ω_{bi} is blood perfusion rate of corresponding biological tissue layer (m^3·s^{-1}·m^{-3}),

T_b is human blood temperature (°C), where T_b = 37 °C,

q_{meti} is the amount of metabolic heat of corresponding biological tissue layer (W/m^3),

T is the absolute temperature (K),

κ_i is thermal conductivity coefficient of corresponding biological tissue layer (W/m·K),

t is time (s).

The left-hand side of equation (2) is the rate of change in thermal energy comprised in a unit volume of biological tissue. Three summands in the right-hand side of this equation are the rate of change in thermal energy due to thermal conductivity, blood perfusion and metabolic heat, respectively.

At the first step of research, $\frac{\partial T}{\partial t} = 0$, so Eq.(2) is simplified as:

$$\nabla(\kappa_i \cdot \nabla T) + \rho_b \cdot C_b \cdot \omega_{b_i} \cdot (T_b - T) + q_{met_i} = 0\,. \tag{3}$$

A steady-state equation of heat exchange in biological tissue (3) is solved with the boundary conditions (4), where q is thermal flux density, T_0 is ambient temperature, α is heat exchange coefficient:

$$\begin{cases} q\big|_{x=0} = 0, \\ q\big|_{x=a} = 0, \end{cases} \quad \begin{cases} q\big|_{y=0} = 0, \\ q\big|_{y=a} = 0, \end{cases} \quad \begin{cases} T\big|_{z=0} = 37\ ^\circ\mathrm{C}, \\ q\big|_{z=b} = \alpha \cdot (T_0 - T), \end{cases} \tag{4}$$

At the second step, temperature distribution in biological tissue is found by solving Eq.(2) with the boundary conditions (4) and the initial temperature distribution T(x, y, z). In so doing, in the thermoelectric microgenerator and heat accumulator we solve a general equation of heat exchange [1, 2]:

$$\rho_i \cdot C_i \cdot \frac{\partial T}{\partial t} = \nabla(\kappa_i \cdot \nabla T), \quad (5)$$

where $i = 5, 6$ is thermal generator and heat accumulator material, ρ_i is substance density, C_i is substance specific heat, κ_i is thermal conductivity coefficient. The boundary conditions for Eq.(5) include adiabatic insulation of thermoelectric microgenerator surfaces and the initial temperature distribution $T = T_{amb} = \text{const}$.

Computer simulation

To study the dynamic operating modes of thermoelectric microgenerators using human heat, a three-dimensional computer model of biological tissue was created having on its top a thermoelectric microgenerator and a heat accumulator. The computer model was constructed with the aid of Comsol Multiphysics applied program package [18] allowing simulation of thermophysical processes in biological tissue with regard to blood circulation and metabolism.

The distribution of temperature and heat flux density in the biological tissue, thermoelectric microgenerator and heat accumulator was calculated by the finite element method (Fig. 2). According to this method, an object under study is split into a large number of finite elements, and in each of them the value of function is sought which satisfies given differential equations of second kind with the respective boundary conditions. The accuracy of solving the formulated problem depends on the level of splitting and is assured by using a large number of finite elements [18].

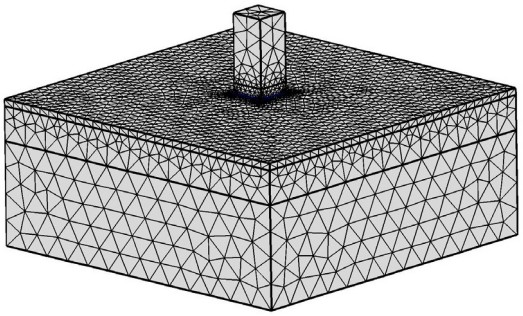

Fig. 2. Finite element method mesh.

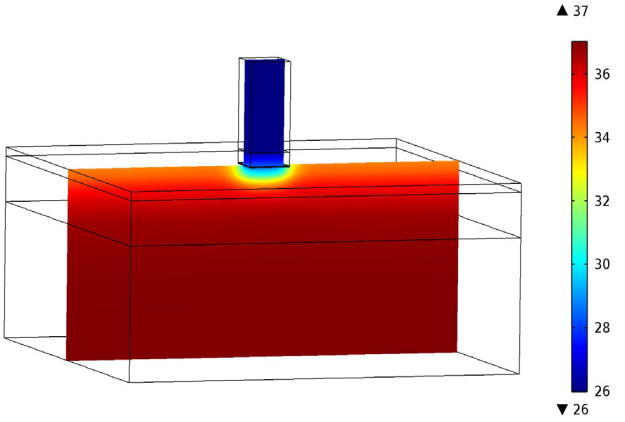

Fig. 3. Temperature distribution in the section of human biological tissue having on its top a thermoelectric microgenerator and a heat accumulator.

Object-oriented computer simulation was used to obtain the distributions of temperature (Fig. 3) and heat flux density lines in human biological tissue, thermoelectric microgenerator and heat accumulator.

Example of computer simulation

Figs. 4-5 a,b,c,d,f represent the dynamics of change in EMF and electric power of a thermoelectric microgenerator of dimensions 10 × 10 mm with the number of legs $N = 624$ and their cross section $S_0 = 0.35 \times 0.35$ mm^2 for different leg length $L = 0.5$; 1.0; 1.5; 2; 2.5; 3 mm and bar-shaped heat accumulator length $h = 0$; 2; 5; 10; 20; 30 mm (ambient temperature $T = 24$ °C).

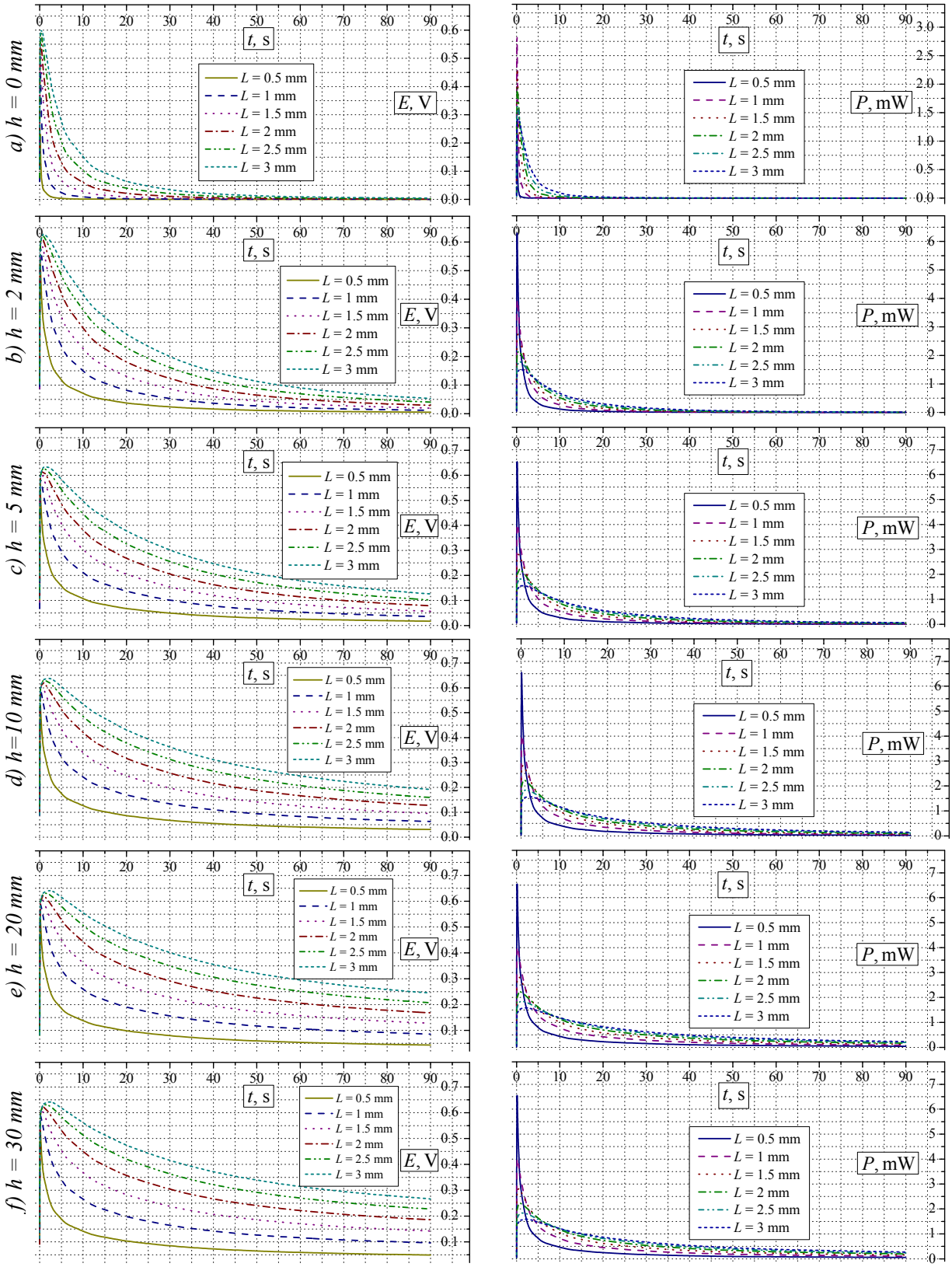

Fig. 4. Dynamics of change in EMF and electric power of thermoelectric microgenerator with different length of legs and heat accumulator (each curve corresponds to certain length of thermogenerator legs, and each figure – to certain length of heat accumulator).

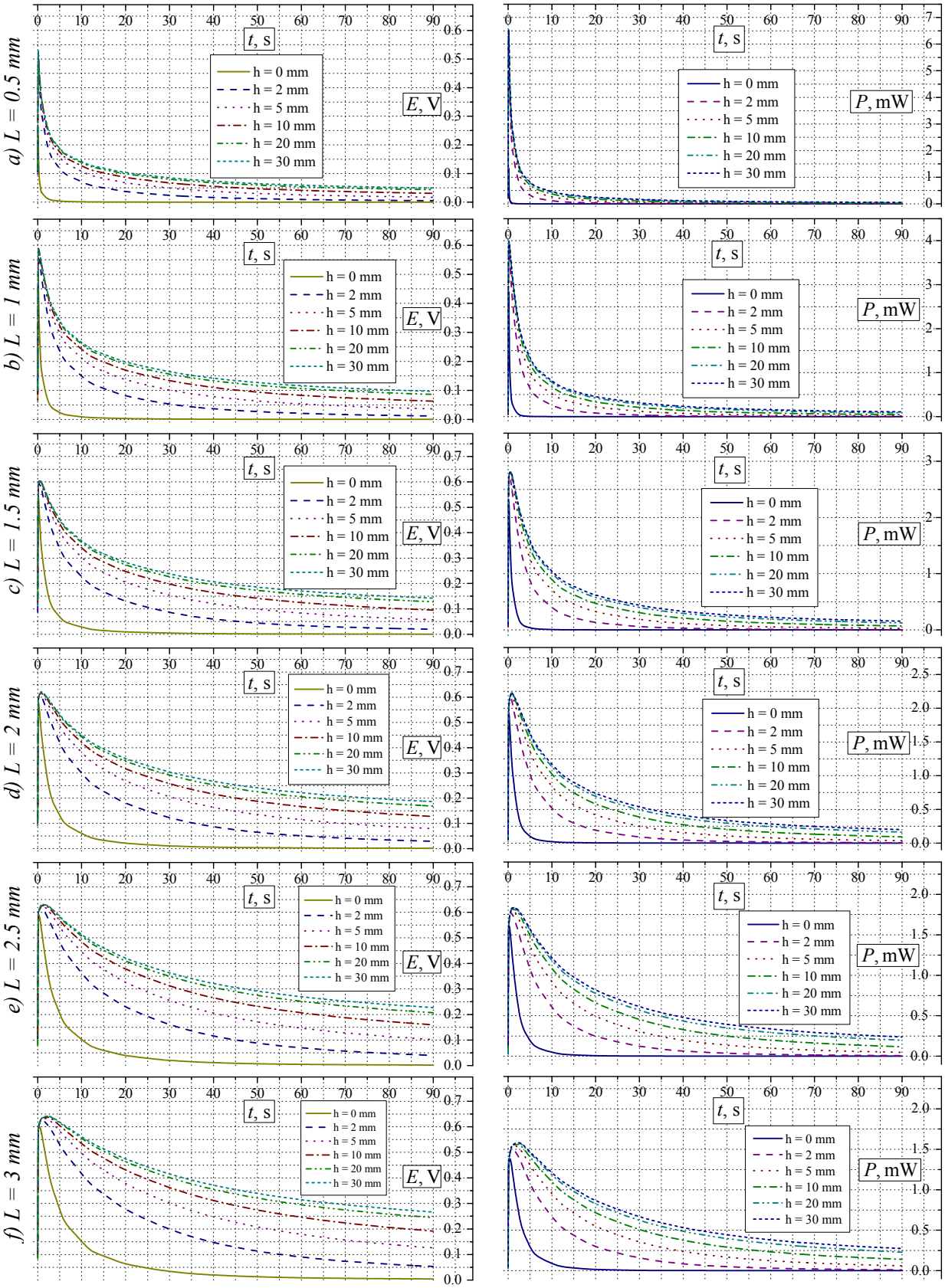

Fig. 5. Dynamics of change in EMF and electric power of thermoelectric microgenerator with different length of legs and heat accumulator (each curve corresponds to certain length of heat accumulator, and each figure – to certain length of thermal generator legs).

From the analysis of Figs. 4-5 a,b,c,d,f it is evident that increasing the length of heat accumulator and the length of thermoelectric microgenerator legs improves its energy characteristics. However, from this representation it is difficult to estimate the rates of the energy characteristics improvement and to determine the optimal length values of heat accumulator and thermoelectric microgenerator legs. Let us consider a more specific case when microgenerator first works in the mode of electric energy accumulation, and then this energy is used to power the electronic circuit of a short-life medical device, for instance, electronic thermometer. The time of electric energy accumulation in this case corresponds to the heating time of thermometer temperature sensor and is nearly 20 s. The dependence of electric power of such microgenerator at this time moment is given in Fig. 6.

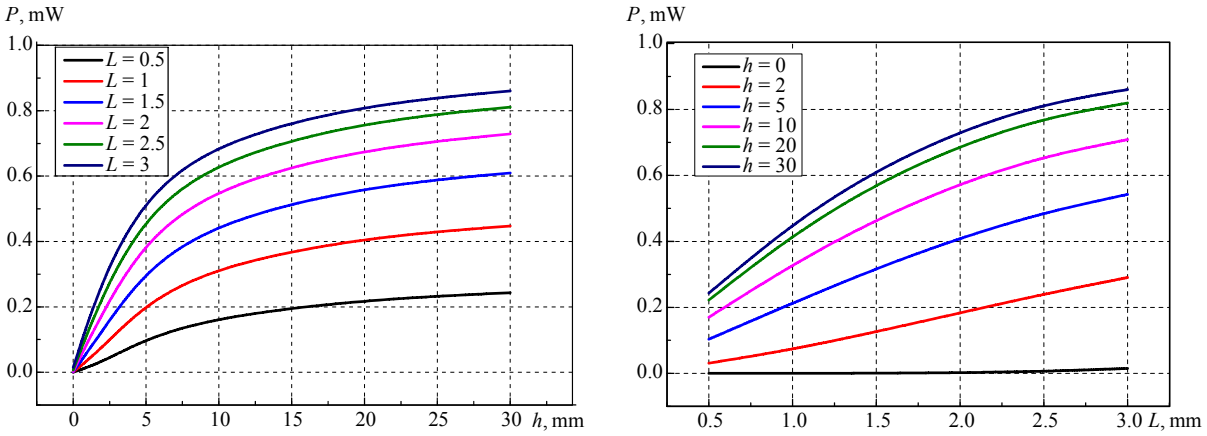

a) *b)*

Fig. 6. Electric power of thermoelectric microgenerator at time moment t = 20 s:
a) versus the length of heat accumulator h for different lengths of legs L;
b) versus the length of legs L for different lengths of heat accumulator h.

From the plots it is evident that it will be most reasonable to use heat accumulator of length about $h = 5 \div 10$ mm, since the rates of increasing the electric power of thermoelectric microgenerator are essentially reduced at lengths larger than $h = 10$ mm.

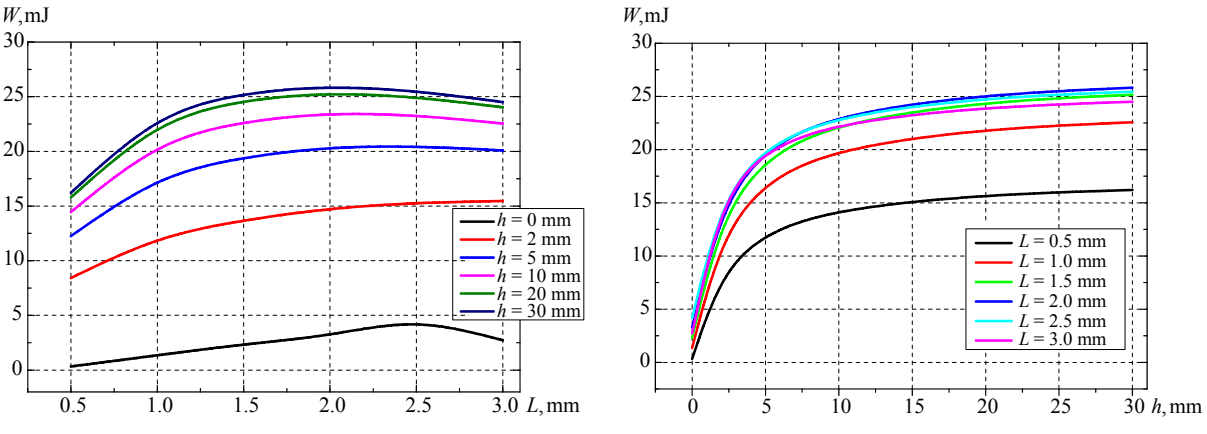

a) *b)*

Fig. 7. Electric energy produced during time t = 20 s:
a)versus the length of legs L for different lengths of heat accumulator h;
b) versus the length of heat accumulator h for different lengths of legs L.

Fig. 6b shows that in the absence of heat accumulator on a thermoelectric microgenerator located on the surface of human skin, the electric power generation is practically absent. Also from the figure it is seen that with heat accumulator length $h = 2 \div 10$ mm the electric power is directly proportional to the length of microgenerator legs.

However, using thermoelectric microgenerators with the length of legs larger than $L = 3$ mm is unreasonable, which is evident if we estimate not the power at certain time moment, but the electric energy W produced by this moment (Fig. 7).

Fig. 7 shows a dependence of electric energy obtained during time $t = 20$ s since the moment of contact between thermoelectric microgenerator and the skin surface. From Fig. 7 a it is seen that in the absence of heat accumulator the optimal length of microgenertaor lengs is $L = 2.5$ mm, and with increasing the length of heat accumulator, the optimal length of legs is gradually reduced to $L = 2$ mm. Thus, the optimal length of microgenerator legs is $L = 2 \div 2.5$ mm (Fig.7 a,b). In so doing, the energy obtained during the first 20 s of microgenerator work is at the best W = 25.8 mJ.

For comparison to the steady-state mode, let us consider the work of a thermoelectric microgenerator of size 10×10 mm with a mass- and size-alike heat sink in the state of heat exchange with the environment. For correct comparison, we will give the energy obtained during time $t = 20$ s in steady-state operating condition of thermal generator depending on the length of microgenerator legs L and the length of heat sink fins h (Fig.8).

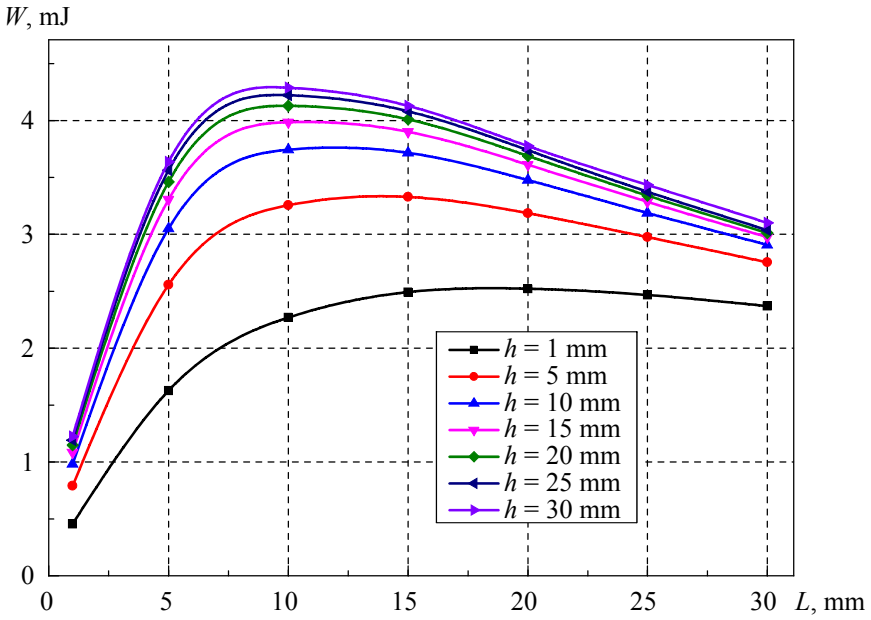

Fig.8. Electric energy produced during time t = 20 s versus the length of microgenerator L for different lengths of heat sink fins h in steady-state mode.

From Fig. 8 it is easily seen that in steady-state operating mode of microgenerator the electric energy is at the best case W = 4.3 mJ. Thus, the energy obtained during the first 20 s of transient mode is 6-fold the energy obtained during a similar time interval in steady-state operating mode of microgenerator. Using a device for electric energy accumulation and output voltage stabilization, one can use the energy generated at the initial step for power supply to short-life equipment, such as electronic thermometers. This confirms the advisability of using dynamic operating modes of thermoelectric microgenerator using human heat for power supply to low-power electronic devices.

Conclusions

A theory of computer simulation of processes of thermal human energy conversion into electric energy is developed enabling one to design thermoelectric microgenerators using the heat of human body and to optimize their design in order to achieve the highest efficiency of thermoelectric energy conversion in dynamic operating modes.

Computer methods of simulation of thermal and electrical processes occurring at the interaction of thermoelectric microgenerators and human body are developed. For the partial case it is established that the energy of the first 20 s of transient mode is 6-fold the energy obtained during the same time interval in steady-state operating mode of microgenerator.

The advisability of using dynamic operating modes of thermoelectric microgenerator for power supply to low-power electronic devices is confirmed.

References

1. L.I.Anatychuk, *Thermoelements and Thermoelectric Devices: Handbook* (Kyiv: Naukova Dumka, 1979), 768 p.
2. L.I.Anatychuk, *Thermoelectricity, Vol.2, Thermoelectric Power Converters* (Kyiv, Chernivtsi: Institute Thermoelectricity, 2003), 376 p.
3. L.T.Strutynska, Thermoelectric Microgenerators. State of the Art and Application Potential, *Tekhnologiya i Konstruirovaniye v Elektronnoi Apparature* **4**, 5-13 (2008).
4. V. Leonov and R. J. M. Vullers, Wearable Electronics Self-Powered by Using Human Body Heat: The State of the Art and the Perspective, *Journal of Renewable and Sustainable Energy* **1**, 062701 (2009).
5. M. Lossec, B. Multon, H. Ben Ahmed, and C. Goupil, Thermoelectric Generator Placed on the Human Body: System Modeling and Energy Conversion Improvements, *Eur. Phys. J. Appl. Phys.* **52**, 11103 (2010).
6. Y.Yang, J. Liu, Evaluation of the Power-Generation Capacity of Wearable Thermoelectric Power Generator, *Front. Energy Power Eng. China* **4**(3), 346–357 (2010).
7. L.I.Anatychuk, R.R.Kobylyanskii, and S.B.Romanyuk, *Patent of Ukraine № 87400*, InCl H0135/00, Electronic Medical Thermometer with Thermoelectric Power Supply, Application № u 2013 08794; filed. 15.07.13; publ. 10.02.14, Bul. № 3.
8. L.I.Anatychuk, R.R.Kobylianskyi, On the Accuracy of Temperature Measurement Using

Electronic Medical Thermometer with Thermoelectric Power Supply, *J.Thermoelectricity* **5**, 75-79 (2013).
9. L.I.Anatychuk, R.R.Kobylianskyi, and I.A.Konstantinovich, The Impact of a Thermoelectric Supply on the Accuracy of Temperature and Heat Flux Measurement, *J.Thermoelectricity* 6, 53-61 (2013).
10. R.R.Kobylianskyi, O.M.Manik, and S.B.Romanyuk, Electronic Medical Thermometer with Thermoelectric Power Supply, *Scientific Bulletin of Chernivtsi University: Proceedings. Physics. Electronics* **3**(1), 38-44 (2013).
11. L.I.Anatychuk, R.R.Kobylianskyi, and I.A.Konstantinovich, Thermoelectric Power Supply for Electronic Medical Thermometer, *Tekhnologiya i Konstruirovaniye v Elektronnoi Apparature* 4, (2014).

12. L.I.Anatychuk, R.R.Kobylianskyi, Some Specific Features of Dynamic Operating Modes of Thermal Generator Using Human Heat, *J.Thermoelectricity* **3**, 59-71 (2014).
13. S.C.Jiang S.C, N.Ma, H.J.Li, and X.X.Zhang, Effects of Thermal Properties and Geometrical Dimensions on Skin Burn Injuries, *Burns* **28**, 713-717 (2002).
14. M.P.Cetingul, C.Herman, Identification of Skin Lesions from the Tansient Thermal Response using Infrared Imaging Technique *IEEE*, 1219-1222 (2008).
15. M.Ciesielski, B.Mochnacki, and R.Szopa, Numerical Modeling of Biological Tissue Heating. Admissible Thermal Dose, *Scientific Research of the Institute of Mathematics and Computer Science* **1**(10), 11-20 (2011).
16. Florin Filipoiu, Andrei Ioan Bogdan, and Iulia Maria Carstea, Computer-Aided Analysis of the Heat Transfer in Skin Tissue, *Proceedings of the 3rd WSEAS Int. Conference on Finite Differences - Finite Elements - Finite Volumes - Boundary Elements*, 53-59 (2010).
17. Daniela Carstea, Ion Carstea, and Iulia Maria Carstea, Interdisciplinarity in Computer-aided Analysis of Thermal Therapies, *WSEAS Transactions on Systems and Control* **6**(4), 115-124 (2011).
18. COMSOL Multiphysics User's Guide, *COMSOLAB*, 804 (2010).

Submitted 17.10.14

L.I. Anatychuk

L.I. Anatychuk, R.V. Kuz

Institute of Thermoelectricity of the NAS and MES
Ukraine, 1, Nauky Str.,
Chernivtsi, 58029, Ukraine

R.V. Kuz

EFFECT OF AIR COOLING ON THE EFFICIENCY OF SECTIONAL THERMOELECTRIC GENERATOR IN A CAR WITH A DIESEL ENGINE

The paper is concerned with a physical model of sectional thermoelectric generator (TEG) for a diesel engine with a system of heat removal from TEG comprising an air-to-liquid heat exchanger and an electric fan. A mathematical description of the model is presented. A computer model of sectional TEG is developed. Computer simulation for a 75 kW disel engine is performed. The optimal hot temperatures of the generator sections and the optimal fan powers whereby maximum net power is attained and, accordingly, maximum real efficiency of TEG with regard to expenditures on the fan supply for ambient temperatures in the range of –40…+50^{O}C are found. A comparison of sectional generator efficiency to the previously obtained values for one-section TEG is made. It is shown that a real efficiency of sectional TEG with a heat removal system is 1.2 – 1.4 times higher than that of one-section TEG.

Key words: heat recovery, thermoelectric generator, internal combustion engines.

Introduction

The use of waste heat from internal combustion engines is a relevant practical application of thermoelectricity. Its purpose is fuel saving due to the use of engine exhaust heat for electric energy generation [1, 2]. It is known that the presence of a thermoelectric generator in a car has a considerable impact on its operation. One of the negative factors reducing TEG efficiency are the expenditures related to the necessity of heat removal from a thermoelectric generator. A detailed estimate of expenditures on heat removal from one-section thermoelectric generator for cars with different engine types is given in [3, 4]. It is shown that expenditures on heat removal from one-section TEG by heat-exchangers with electric fans can reach 15-25% of the electric energy produced by TEG. It is also established that the efficiency of heat removal from TEG in a car has optimal values that depend on the supply power of heat removal system and ambient air temperature. It is important to proceed with investigations in order to establish similar laws for sectional TEG, because, as is known [1, 2], the use of sectional TEG assures more efficient exhaust heat recovery.

The purpose of this work is to develop computer simulation procedure for sectional thermoelectric generator for a car with a diesel engine and liquid-air cooling and to verify its efficiency for a concrete case of engine and thermal generator.

Physical model of sectional thermoelectric generator for a car

A detailed analysis of a physical model of a car with one-section TEG with regard to heat removal from the TEG and its mathematical description is given in [3]. The specific feature of a model

in the present paper is that the TEG comprises 3 sections. As is shown in [6], sectioning yields higher TEG efficiency, however, the use of a larger number of sections is not reasonable. So, let us dwell in detail on TEG model.

The maximum efficiency of sectional thermoelectric generator was calculated according to method [1, 7]. Let us consider a TEG consisting of 3 sections connected in series relative to hot gas flow and cold heat carrier (Fig. 1).

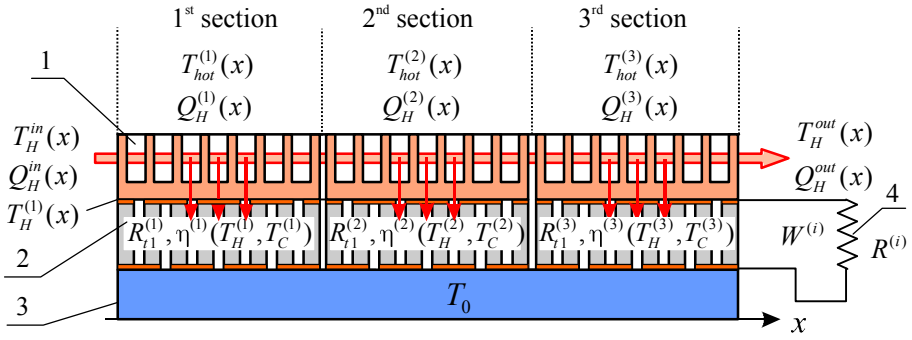

Fig. 1. A physical model of a sectional thermoelectric generator: 1 – hot heat exchanger; 2 – thermopiles; 3 – cold heat exchanger; 4 – matched electric load of a section.

Each TEG section consists of a hot heat exchanger (1), a thermopile (2) with thermal resistance $R_{t1}^{(i)}$ and efficiency $\eta(T_H, T_0)$; a cold heat exchanger (3) with temperature T_0. The thermopiles of each section are loaded on matched electric load $R^{(i)}$ (4). The inlet hot gas flow has temperature T_H^{in} and thermal power Q_H^{in}. The hot gas gives part of heat $Q_H^{(i)}(x)$ at temperature $T_{hot}^{(i)}(x)$ to the hot heat-exchanger. At TEG outlet, the gas flow has temperature T_H^{out} and thermal power Q_H^{out}. Heat from the hot heat-exchanger is transferred to the thermopile heating its hot side to temperature $T_H^{(i)}(x)$. The cold side of thermopiles is maintained at temperature T_0. For the calculations of maximum possible TEG power the thermal expenditures will be ignored.

Mathematical and computer description of the model

For thermoelectric generator optimization it is necessary to find the temperature and heat flow distributions in the thermopiles of each section. Such a calculation for the presented model is possible only with the use of computer simulation.

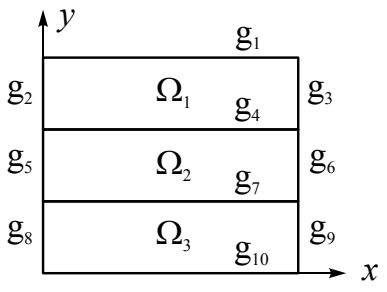

Fig. 2. Computer representation of the areas and boundaries of TEG section.

Let us consider one of generator sections and conventionally divide it into 3 areas $\Omega_1 - \Omega_3$ with the boundaries $g_1 - g_{10}$ (Fig. 2). The area Ω_1 is the hot heat exchanger with a heat carrier, Ω_2 is the thermopile, Ω_3 - the hot and cold heat exchangers.

In the area Ω_1 there is mass transfer of the hot heat carrier. For this area the thermal conductivity equation will be given by

$$-\nabla\left(\kappa_H(T)\nabla T\right) = -\rho_H(T)C_H(T)\vec{v}\nabla T\,, \qquad (1)$$

where ρ_H is gas density, C_H is gas heat capacity, κ_H is gas thermal conductivity, v_H is gas velocity. The boundary conditions for the area Ω_1 take into account the continuity of gas flow within a section and between the sections, heat flow through heat exchangers.

In the area Ω_2 there is the Joule heat release in the thermopile. For the area Ω_2 the thermal conductivity equation is given by

$$-\nabla\left(\kappa_{TE}(T)\nabla T\right) = Q_J \tag{2}$$

where κ_{TE} is the effective thermal conductivity of the thermopile, Q_J is the Joule heat released in the bulk of the thermopile.

The boundary conditions for the area Ω_2 take into account the interaction between the thermopile and the heat exchangers.

The area Ω_3 in this TEG model is considered to be thermostated with temperature T_0.

Mathematically, a set of the boundary conditions is expressed as follows:

g1: $$q_1^{(i)}(x) = 0\,, \tag{3}$$

g2, g3: $$Q_H^{in(1)} = Q_H^{in},\ Q_H^{in(i+1)} = Q_H^{out(i)},\ Q_H^{out(N)} = Q_H^{out}\,, \tag{4}$$

g4: $$Q_H^{(i)}(x) = \left(T_H^{(i)}(x) - T^{(i)}(x)\right) / R_{t1}^{(i)} \tag{5}$$

g5, g6: $$q_4^{(i)}(y) = 0\,, \tag{6}$$

g7: $$Q_C^{(i)}(x) = \left(T_C^{(i)}(x) - T^{(i)}(x)\right) / R_{t2}\,,$$

$$T(x) = T_0 \tag{7}$$

Ω_3, g8, g9, g10: $$T(x,y) = T_0 \tag{8}$$

A set of equations (1)-(2) with the boundary conditions (3-8) allows to find the temperature field $T(x,y)$ in the TEG and to determine the distribution of temperatures $T_H^{(i)}(x)$ across the hot sides of the thermopiles in the sections.

Then the power of each section can be found from the following expression:

$$W^{(i)} = \int Q_H^{(i)}(x)\eta(T_H^{(i)}(x), T_C^{(i)}(x))dx\,. \tag{9}$$

Total generator power

$$W_{TEG} = W^{(1)} + W^{(2)} + W^{(3)}\,. \tag{10}$$

The efficiency of thermoelectric generator

$$\eta_{TEG} = \frac{W_{TEG}}{Q_H^{in}}\,. \tag{11}$$

To calculate the electric power of TEG with regard to provision of heat removal system operation, one should know the efficiency of air-to-liquid heat exchanger

$$Q_{cool} = f(W_{cool}, T_L, T_A) \tag{12}$$

where Q_{cool} is thermal power of heat removal system, W_{cool} is electric supply power of heat removal system, T_L is liquid temperature, T_A is air temperature. This dependence was obtained from the experimental investigations of the heat exchanger [3].

The effective efficiency of TEG is introduced by the expression:

$$\eta_{ef} = (W_{TEG} - W_{cool}) / Q_{in}\,. \tag{13}$$

The system of equations (1)-(2) with the boundary conditions (3)-(8) was solved by finite element method [6] on a 2-dimensional mesh.

Fig. 3 gives an example of computer-simulated 2-dimensional temperature field in TEG sections.

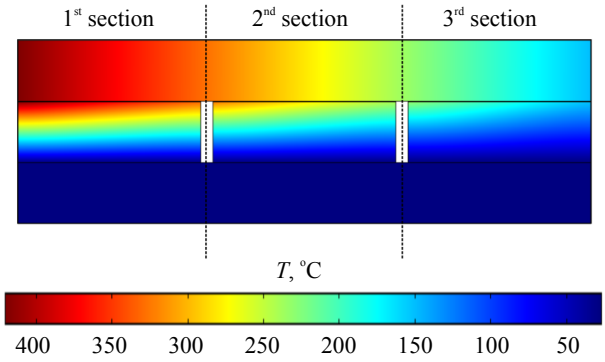

Fig. 3. Temperature distribution in TEG sections.

Further TEG optimization consists in finding the optimal hot temperatures by varying thermal resistances of sections to reach maximum integral efficiency of TEG.

Example of TEG parameters calculation

As an example, we shall calculate the basic parameters of sectional TEG for a 75 kW diesel engine with the exhaust gas temperature 420°C.

For the efficiency and power calculation, the thermoelectric materials based on *Bi-Te*, whose figure of merit is among the best in the operating temperature range of TEG diesel engines, were selected [6]. The characteristics of air-to-liquid heat exchanger necessary for calculations were taken from [3].

TEG hot side temperature optimization. In the beginning, optimization for the hot temperatures of TEG sections took place according to procedure [2]. Fig. 4 shows an example of such optimization for the third TEG section. It is seen that there exists optimal TEG efficiency that depends on the hot and cold temperatures. Fig. 5 shows the values of the optimal hot temperatures of sections versus their cold temperature.

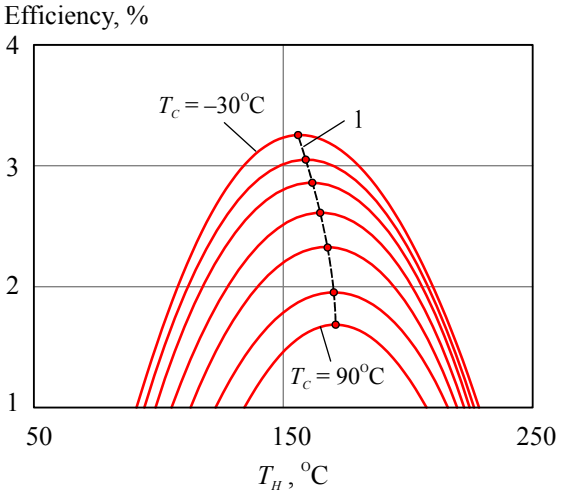

Fig. 4. The efficiency of 3rd TEG section versus section hot temperature. T_C varies from –30°C to +90°C. 1 are optimal hot temperatures.

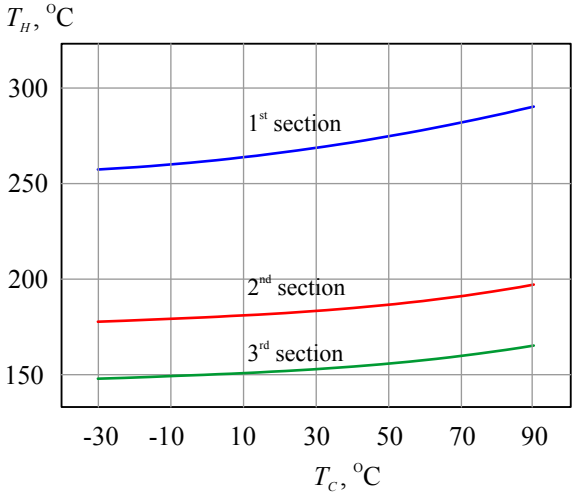

Fig. 5. Optimal hot temperature of TEG sections versus their cold temperature.

Heat removal system optimization. Calculation of the optimal expenditures on heat removal from TEG sections took place according to procedure [3, 4]. Fig. 4 shows the value of thermal power to be removed from TEG versus the cold temperature of TEG.

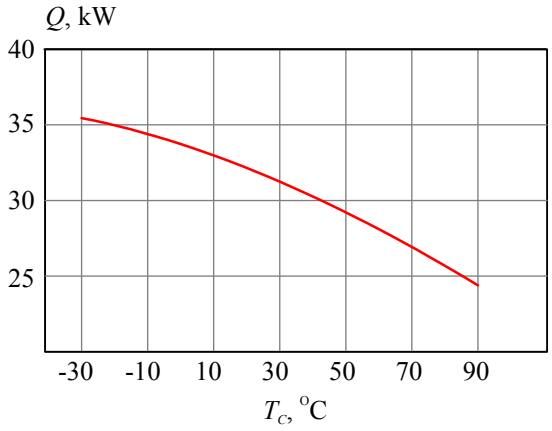

Fig. 6. Thermal power to be removed from TEG versus the cold temperature of TEG.

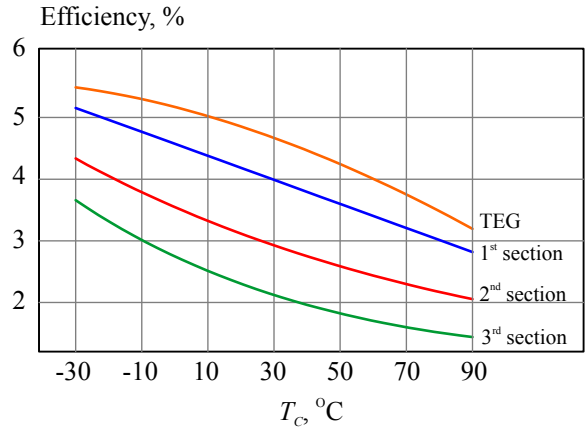

Fig. 7. The efficiency of sections and the integral TEG efficiency versus the cold temperature of TEG.

Fig. 7 shows the efficiency values of each of the three TEG sections and the integral TEG efficiency versus the cold temperature of TEG.

Fig. 8 shows the results of "TEG-cooling system" optimization for different ambient temperatures. The optimal power values of cooling system fan are presented here. They make ~14%...24% of thermal generator power. Fig. 9 shows the electric power of TEG versus ambient temperature with regard to expenditures on heat removal.

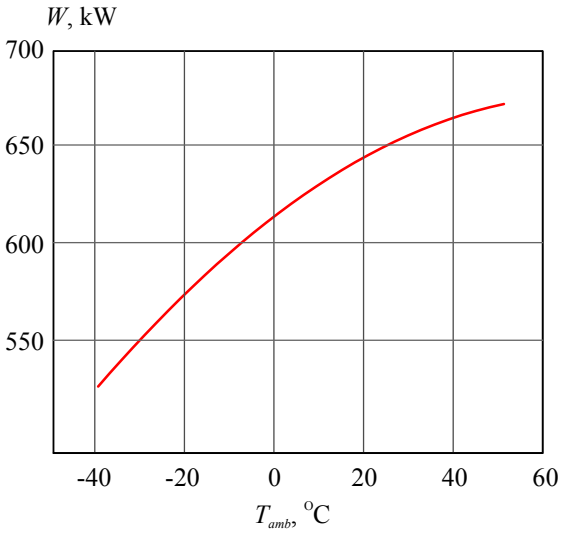

Fig. 8. The optimal electric power of TEG cooling system versus the ambient temperature.

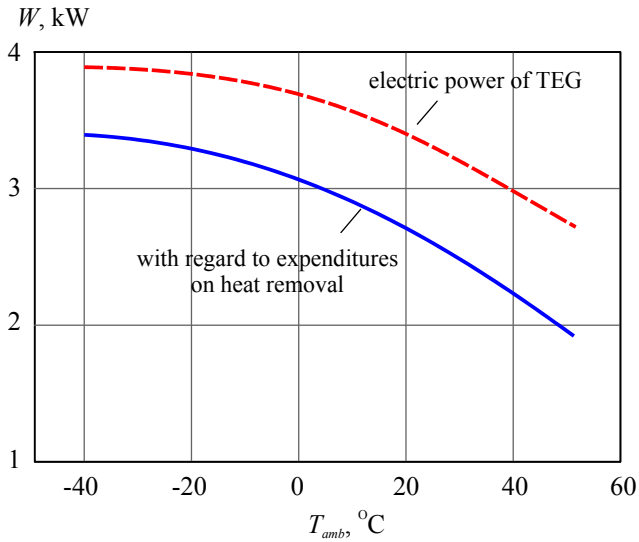

Fig. 9. The electric power of TEG versus the ambient temperature.

Fig. 10 compares the efficiency of one-section TEG [3] and three-section TEG analyzed in the present paper.

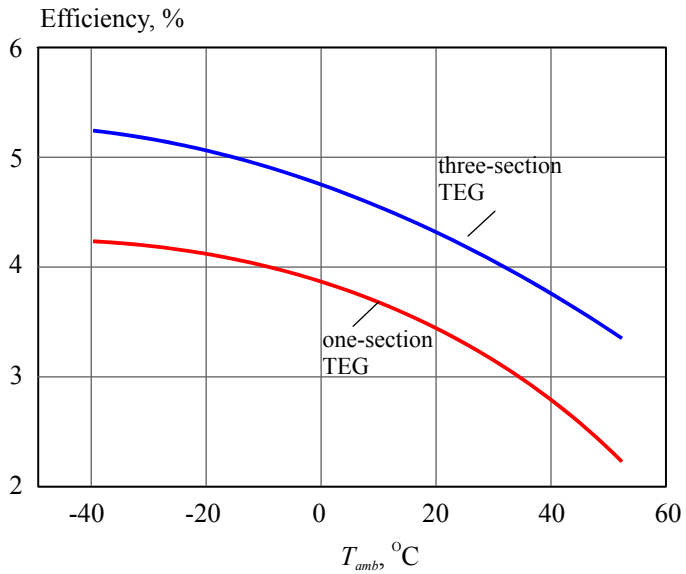

Fig. 8.The efficiency of TEG versus the ambient temperature.

It is seen that the use of generator sections, under otherwise equal conditions, yields better efficiency values. The use of sections assures 1.2 -1.4 times higher efficiency of TEG. According to the results of [3], this can give fuel saving about 3-7%.

Conclusions

1. A physical model of three-section thermoelectric generator for a car with a diesel engine has been created. The presence of three sections has been previously substantiated while investigating a multi-section generator. A mathematical description of three-section generator has been made and software for its study and optimization has been developed.

2. The efficiency of computer simulation has been demonstrated by a case study of a generator for a car with a 75 kW diesel engine. The optimal hot temperatures of sections have been obtained as a function of the cold temperature of TEG in the range of –30…+90^{O}C. It has been established that with increasing the cold temperature of TEG, the optimal hot temperatures are also displaced towards the range of higher values.

3. Optimization of heat removal system has been performed. The optimal electric energy expenditures on heat removal have been determined. It has been established that these expenditures increase from 530 W to 670 W with a rise in ambient temperature from –40^{O}C to +50^{O}C.

4. The power of TEG as a function of ambient temperature has been determined. It has been established that the highest power value (~4 kW) is achieved at T_{amb} = –40 ^{O}C and reduced to 2.8 kW at T_{amb} = +50 ^{O}C. Part of this energy is spent on heat removal from TEG. With regard to these expenditures, the generator power at T_{amb} = –40 ^{O}C is 3.2 kW and reduced to 2 kW at T_{amb} = +50 ^{O}C.

5. The efficiency of sections and the integral efficiency of TEG have been found as a function of the cold side temperature of TEG. The highest efficiency values occur on the first section to which the exhaust gas from the engine is fed directly. The efficiency varies from ~5% to 3% with a change in TEG cold temperature in the range of –30…+90^{O}C. The next section to which the gas that passed through the first section is fed has the efficiency values from 4.3% to 2%. The third section which utilizes the heat of exhaust gases that passed through the first and second sections yields the lowest efficiency values in the

range of 3.6…1.4%. In so doing, the integral efficiency is the highest at $T_C = -30\ ^{O}$C and makes ~5.5%. It is reduced to 3.2% at $T_C = +90\ ^{O}$C.

6. A comparison of the efficiency of one-section and three-section generators demonstrates efficiency increase with the use of three sections from 4.2% to 5.2% at $T_{amb} = -40\ ^{O}$C. The efficiency of three-section generator also remains higher at elevated ambient temperatures. At $T_{amb} = +50\ ^{O}$C the efficiency of three-section TEG is 3.3%, while the efficiency of one-section TEG is as low as 2.2%.

7. In general, the above studies demonstrate the advantages of three-section TEG in the electric power and efficiency by a factor of 1.2…1.4. The results obtained also prove the fact that a TEG for a diesel engine is more efficient when operated at low ambient temperatures. The electric energy expenditures on heat removal from TEG are minimal as well.

References

1. L.I.Anatychuk, R.V.Kuz, Yu.Yu.Rozver, The Efficiency of Thermoelectric Heat Recuperators from the Exhaust Gas of Internal Combustion Engines, *J.Thermoelectricity* **4**, 89-96, 2011.
2. L.I.Anatychuk, R.V.Kuz, and Yu.Yu.Rozver, Thermoelectric Generator for a Petrol Engine, *J.Thermoelectricity* 2, 75-79, (2012).
3. L.I.Anatychuk, R.V.Kuz, Effect of Air Cooling on the Efficiency of Thermoelectric Generator in a Diesel-Engined Car, *J.Thermoelectricity* **2**, 57-64, (2014).
4. L.I. Anatychuk, R.V.Kuz, Effect of Air Cooling on the Efficiency of a Thermoelectric Generator in a Car with a Petrol Engine, *J.Thermoelectricity* **3**, 84-87, (2014).
5. Comsol Multiphysics – http://www.comsol.com.
6. L.I.Anatychuk, R.V.Kuz, Materials for Vehicular Thermoelectric Generators, *Proc. of ICT-2011*, Michigan, USA.
7. R.V. Kuz', M.N. Strutinsky, Computer simulation of single-stage thermoelectric generator module, *J.Thermoelectricity* **3**, 21-27, (2010).

Submitted 17.10.14

L.I. Anatychuk

L.I. Anatychuk, V.V. Lysko

Institute of Thermoelectricity of the NAS and MES
Ukraine, 1, Nauky Str.,
Chernivtsi, 58029, Ukraine

V.V. Lysko

METHODS FOR ASSURING HIGH QUALITY ELECTRIC AND THERMAL CONTACTS WHEN MEASURING PARAMETERS OF THERMOELECTRIC MATERIALS

A computer model is created that allows studying the errors in the measurement of electric conductivity and thermal conductivity when using pressure contacts for current and heat supply to the measured sample. The measurement errors for the case of point contacts are determined. It is established that the errors in the measurement of thermal conductivity and electric conductivity can reach 45%.

The results of research on the methods of reducing these errors by creation of metal contact coatings on the sample end surfaces are presented. It is established that if nickel and copper layers are available on the sample end surfaces, even with the worst arrangement of one point contact, the error in the measurement of electric conductivity lies within 1.5-1.8%.

The errors in the measurement of thermal conductivity are determined. It is established that for Ni-Cu-Ni contact structure with a tungsten anti-diffusion plate these errors with the worst arrangement of point contacts will be reduced to 7.4% in case of one contact point on both sample end surfaces and to 1% – in case of three contact points.

Key words: measurement error, electrical conductivity, thermal conductivity.

Introduction

General characterization of the problem. Absolute method is one of the most reliable methods of measuring the temperature dependences of thermoelectric material properties [1, 2]. The main sources of errors when using this method and the possibilities of their minimization are detailed in [3-6]. The achieved values of errors are as follows: thermal conductivity – up to 2.4%, thermoEMF – up to 0.8%, electric conductivity – up to 0.7%, thermoelectric figure of merit – up to 4.7% [7].

In so doing, one of important measurement problems is to assure a reliable electric and thermal contact between the sample under study and the structural components of measuring installation. This is due to the fact that bad contacts can result in considerable deviations from the uniformity of temperature and electric potential distributions in the sample, and, respectively, in measurement errors. This is particularly important at high-temperatures measurements, when the use of solders becomes impossible, and pressure contacts can be even of point type.

Therefore, the *purpose of this work* is to determine the errors in the measurement of electric conductivity and thermal conductivity that arise when using pressure contacts due to distortions of temperature and electric potential uniformity distributions, and to develop methods for minimization of these errors.

1. Physical, mathematical and computer models

In the case of using pressure contacts, the electric potential and temperature in the near-contact areas are distorted. For the reduction of this effect, measuring probes and thermocouples are arranged possibly far from the ends on the sample lateral surface. This allows eliminating the errors in the determination of sample temperature when measuring sample thermoEMF. However, in the determination of electric conductivity and thermal conductivity, deviations from the uniformity of heat and current distribution in the sample will cause errors in that case as well.

1.1. Measurement of electric conductivity

A sample of thermoelectric material shaped as a cylinder of length l and diameter d (Fig. 1) was considered. Openings were made and cylinder probes were installed on the lateral sample surface. It was considered that electric current to the sample is supplied through point contacts on its end surfaces, i.e. sample contacts to the heater and the thermostat, which in the absolute method are used to measure thermal conductivity and simultaneously serve as current leads when measuring electric conductivity. Arrangement of current supply points on the sample end surface can be arbitrary. Sample electric conductivity is found by the formula

$$\sigma = \frac{l}{S}\frac{I}{U}, \tag{1}$$

where U is voltage drop between measuring probes, S is cross-section area of the sample.

Current density nonuniformity due to non-ideality of contacts will lead to the errors in the measurement of electric conductivity calculated by formula (1).

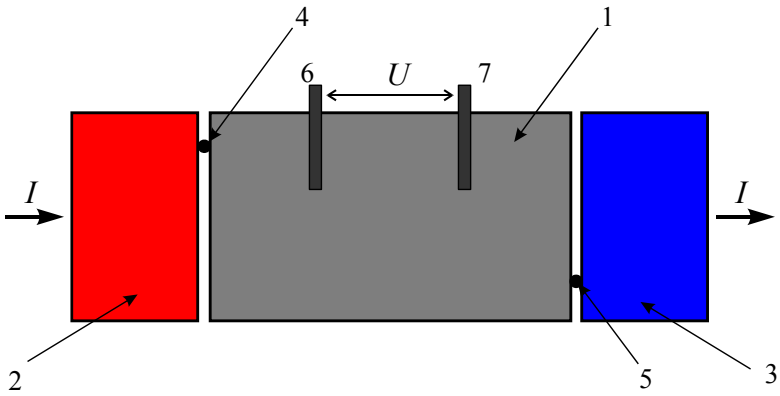

Fig. 1. Physical model for studying the influence of contacts on the accuracy of measurement of thermoelectric material electric conductivity
1 – sample under study, 2 – heater, 3 – thermostat, 4, 5 – point contacts for current delivery to the sample, 6, 7 – measuring probes.

To determine the effect of contact arrangement, it is necessary to calculate the electric potential distribution in the sample based on the equation

$$-\nabla\left(\sigma\nabla\varphi\right) = 0\,. \tag{2}$$

with the following boundary conditions:

1) for sample end surface free from contact to current leads, and the sample lateral surface

$$\mathbf{n}\left(\sigma\nabla\varphi\right) = 0\,; \tag{3}$$

2) for points of current supply to the sample

$$\mathbf{n}\left(\sigma\nabla\varphi\right)=I\,. \tag{4}$$

The error in the determination of electric conductivity δσ is found by the formula

$$\delta\sigma=\left|1-\frac{U/I}{U_{id}/I_{id}}\right|\cdot 100\%\,, \tag{5}$$

where U, I is potential difference between the probes and current through the sample according to the model; U_{id}, I_{id} is potential difference between the probes and current through the sample in the ideal case when current density is identical along the entire sample.

1.2. Measurement of thermal conductivity

When measuring thermal conductivity, the analysis of the sutuation is somewhat complicated by the presence of heat transfer due to radiation and gas thermal conductivity in the area without a direct contact between the sample and the heater and thermostat (Fig. 2).

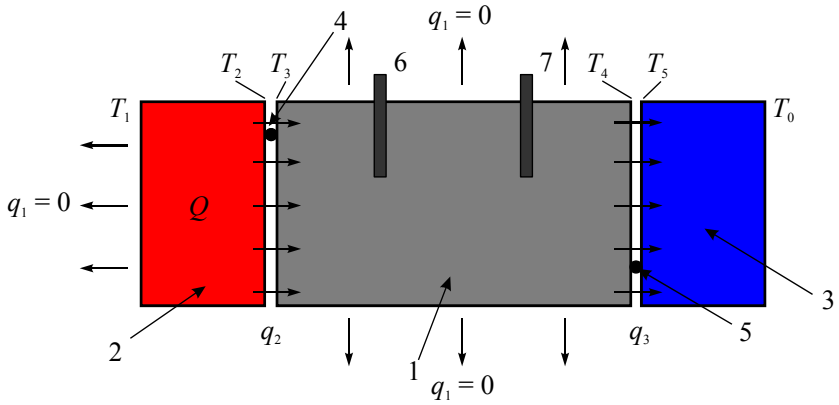

Fig. 2. Physical model for studying the influence of contacts on the accuracy of measurement of thermoelectric material thermal conductivity. 1 – sample under study, 2 – reference heater, 3 – thermostat, 4, 5 – areas of direct contact between the sample and the heater and thermostat, 6, 7 – measuring probes.

To find the distribution of temperature, it is necessary to solve the thermal conductivity equation

$$\nabla\left(-\kappa\cdot\nabla T\right)=Q\,, \tag{6}$$

where κ is thermal conductivity, Q is internal source of heat (equal to Q_h for the heater volume and zero for sample volume).

The boundary conditions for such a problem:

1) thermal insulation of the lateral surface of sample and reference heater

$$q_1=0\,; \tag{7}$$

2) thermostat fixed temperature

$$T=T_0\,; \tag{8}$$

3) heat transfer in the gap between the heater and the sample through gas layer (xenon) and due to radiation

$$q_2=-\varepsilon\sigma_B\left(T_2^4-T_3^4\right)-\kappa_{Xe}\nabla T\,; \tag{9}$$

4) heat transfer in the gap between the sample and the thermostat through gas layer (xenon) and due to radiation

$$q_3=-\varepsilon\sigma_B\left(T_4^4-T_5^4\right)-\kappa_{Xe}\nabla T\,; \tag{10}$$

5) heat transfer from the heater to the sample and from the sample to the thermostat in the area of their direct contact

$$\begin{aligned} T_2 = T_3,\ \kappa_{heater}\nabla T = \kappa_{sample}\nabla T, \\ T_4 = T_5,\ \kappa_{sample}\nabla T = \kappa_{thermostat}\nabla T \end{aligned}. \quad (11)$$

For the calculations, computer simulation via Comsol Multiphysics package was used.

2. Results of computer simulation of the errors in the measurement of electric conductivity

The following variants of places of point contact between the sample and current leads 1-1, 1-2, 1-3, 2-2, 2-3, 3-3, 4-4, 4-2, 4-5 (Fig. 3) were considered for the case of l = 9 mm, d = 6 mm, the distance between the probes a = 5 mm.

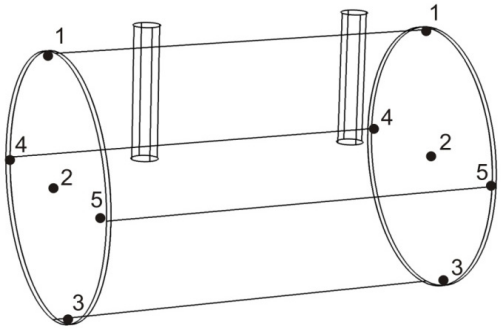

Fig. 3. Arrangement of current supply point contacts on the sample end surfaces.

According to computer simulation, the errors in the measurement of electric conductivity in this case can reach 45%. For current density leveling in the sample, hence, for the reduction of these errors, a thin metal layer, for instance, nickel, can be applied on the end surfaces.

Dependences of a relative error in the measurement of electric conductivity on the thickness of nickel coating h for said current flow directions are shown in Figs. 4, 5.

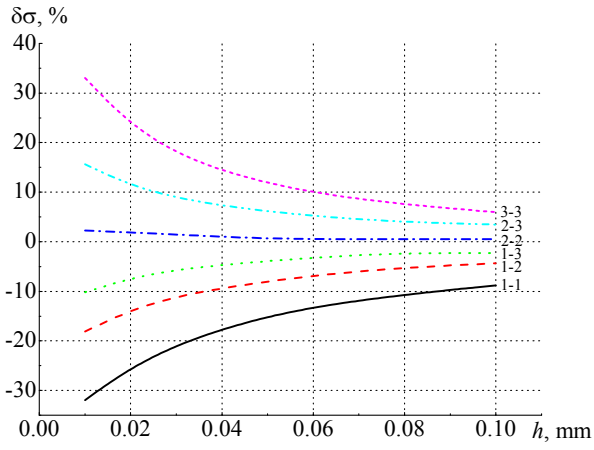

Fig. 4. Dependences of a relative error in the measurement of electric conductivity on the thickness of nickel coating for different current flow directions (1-1, 1-2, 1-3, 2-2, 2-3, 3-3).

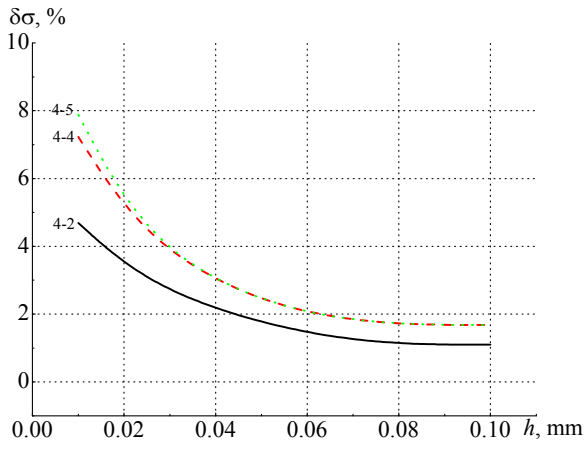

Fig. 5. Dependences of a relative error in the measurement of electric conductivity on the thickness of nickel coating for different current flow directions (4-4, 4-2, 4-5).

For better equalization of electric potential on the sample end surface, an additional copper layer can be applied. Dependences of the error in the measurement of electric conductivity on the thickness of copper coating for different current flow directions are shown in Fig. 6.

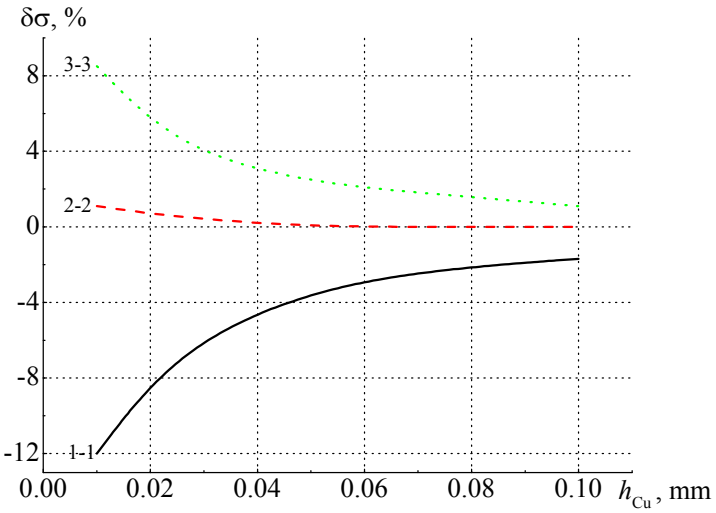

Fig. 6. Dependences of the error in the measurement of electric conductivity on the thickness of copper coating for different current flow directions (nickel thickness – 10 μm).

As is seen, even with the worst arrangement of one point contact, the error in the measurement of electric conductivity lies within 1.5-1.8% (in the presence on the sample end surfaces of 10 μm nickel layer and 100 μm copper layer).

3. Results of computer simulation of the errors in the measurement of thermal conductivity

For the considered case of nickel and copper contact coating Fig. 7 shows the dependences of the errors in the measurement of thermal conductivity on the thickness of heat-levelling copper layer. It is considered that a direct contact between the sample and the heat-exchange surfaces takes place in the area of diameter d_{cont} (for the case of 0.1 μm shown in the figure) and can be arbitrarily arranged on the end surfaces.

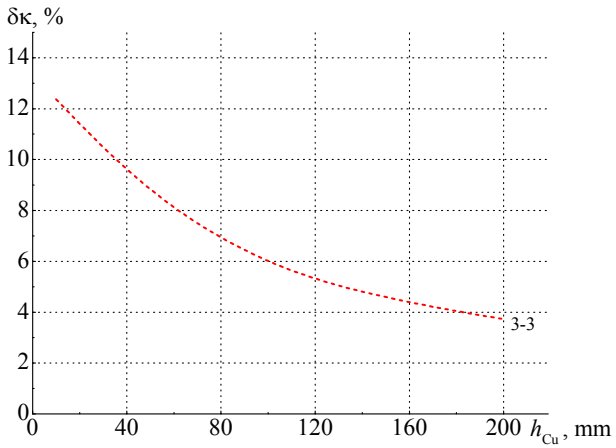

Fig. 7. Dependences of the error in the measurement of thermal conductivity on the thickness of copper coating

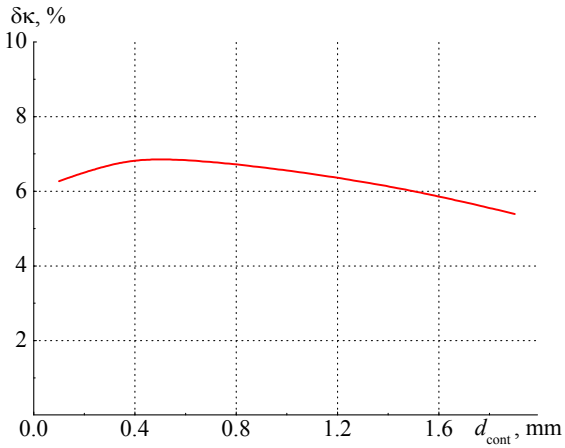

Fig. 8. Dependences of the error in the measurement of thermal conductivity on the diameter of direct

(nickel thickness – 10 μm) *contact area between the sample and the heat-exchange surfaces.*

Dependence of the error on the contact diameter is shown in Fig. 8. In the case at hand the thickness of nickel coating is 10 μm, of copper coating – 100 μm.

Because of heat transfer due to radiation in the gap between the sample and the heat-exchange surfaces, the value of measurement error will be a function of temperature. This dependence for different variants of point contact arrangement and the thickness of copper contact coating is shown in Fig. 9. As is evident, with a rise in temperature, the errors will be reduced.

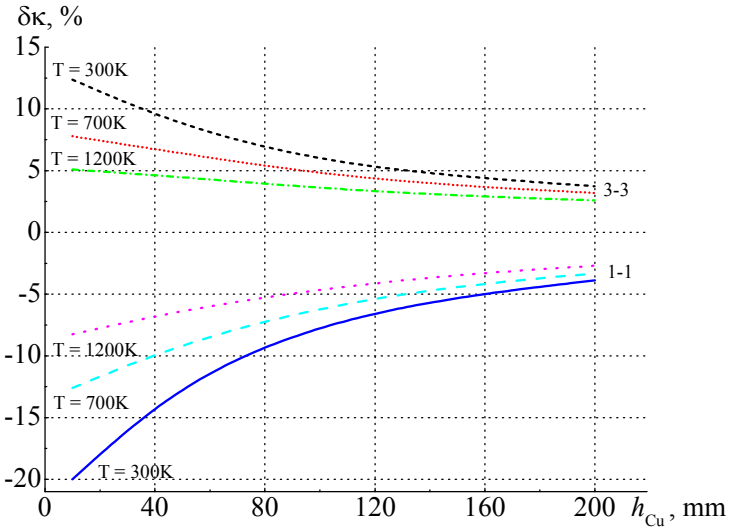

Fig. 9. Dependences of the error in the measurement of thermal conductivity on the thickness of copper coating for different variants of point contact arrangement between the sample and the heat-exchange surfaces and different temperatures.

Another important issue when assuring good contacts is their resistance to elevated temperatures. Experimental studies have shown that at temperatures up to 900°C there can take place a diffusion and adhesion of the heater and the thermostat surfaces to the sample metal coating. This will make it impossible to dismount the sample after the measurements. To prevent this, thin anti-diffusion plates can be placed on both sample sides.

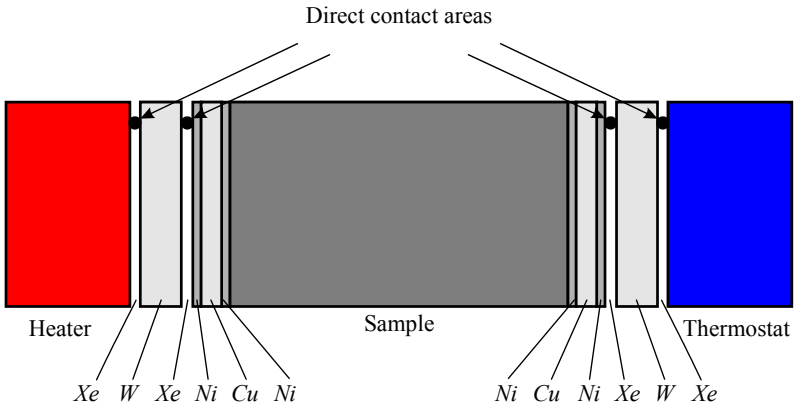

Fig. 10. Schematic of contact structure.

So, the case of a contact structure shown in Fig. 10 was also considered. It has the form of nickel coating (10 μm), copper coating (10 μm) and again nickel coating (10 μm) applied on the

sample end surfaces. A sample with such a coating is forced against the heater and the thermostat through tungsten plates (200 μm thick), so as to assure a direct contact between the sample and the plate and between the plate and the heat exchanger at symmetrical points. Simulation results for different arrangement of such contacts along the sample radius are shown in Fig. 11.

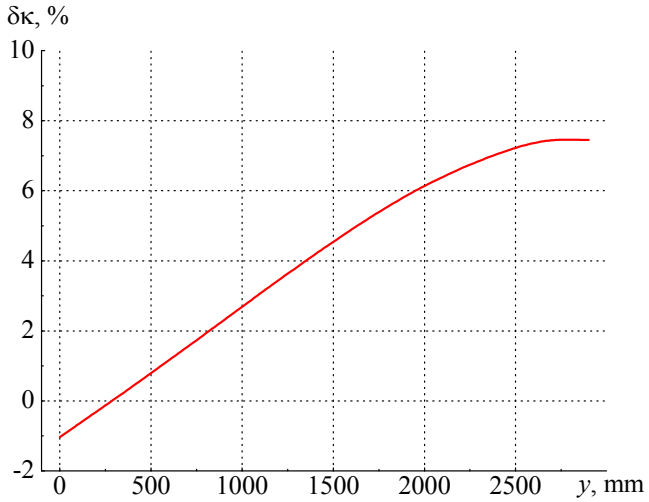

Fig. 11. Dependence of the errors in the measurement of thermal conductivity at place of arrangement of point contacts on the sample end surfaces.

Thus, with the worst arrangement of contacts (one per end surface) the error in the measurement of thermal conductivity will make about 7.4%.

In practice one should expect at least three points of contact between the sample end surfaces and the heater and thermostat. Computer studies of this case were performed that showed considerable reduction of the errors, when with the worst arrangement of three contact points on the sample surface the errors in the measurement of thermal conductivity will not exceed 1%. The errors in the measurement of electric conductivity in this case will be reduced to ~ 0.5%.

Conclusions

The errors in the measurement of electric conductivity and thermal conductivity for the case of point electric and thermal contacts between the sample and current and heat leads are determined. It is established that these errors with the worst arrangement of contact points will reach about 45%.

The methods of reducing these errors by creating on the sample end surfaces of metal contact coatings based on nickel and copper are developed. It is established that for standard sizes of sample under study, in the presence on the sample end surfaces of 10 μm nickel layers and 100 μm copper layers, even with the worst arrangement of one point contact the error in the measurement of electric conductivity will make up to 1.8%, of thermal conductivity – up to 7.8%. In the presence of three contact points, these errors will be reduced to 0.5 and 1%, respectively.

The case of using tungsten anti-diffusion plate to avoid sample contact to the surfaces of current and heat leads at high temperatures is considered. It is established that such a plate will scarcely affect measurement errors.

References

1. J.P. Moore, R.K. Williams, and R.S. Graves, Precision Measurement of the Thermal Conductivity, Electrical resistivity, and Seebeek Coefficient from 80 to 400 K and Their Application to Pure Molybdenum, *Rev. Sci. Instrum* **45**(1), 87-95 (1974).
2. L.L.Anatychuk, S.V.Pervozvansky, and V.V.Razinkov, Precise Measurement of Cooling Thermoelectric Material Parameters: Methods, Arrangements and Procedures, *Proc. of the 12th ICT*, (Japan, 1993), pp. 553-564.
3. L.I.Anatychuk, M.V.Havrylyuk, and V.V.Lysko, Installation for Measurement of Semiconductor Thermoelectric Material Properties, *J.Thermoelectricity* **3**, 41-49 (2010).
4. L.I.Anatychuk, V.V.Lysko, *Patent of Ukraine № 71614*, Device for Measurement of Electric Conductivity, Thermal Conductivity and ThermoEMF of Thermoelectric Materials, Application № u 2011 13846 of 24.11.2011, Publ. 25.07.2012, Bul. №14.
5. L.I.Anatychuk, V.V.Lysko, Investigation of the Effect of Radiation on the Precision of Thermal Conductivity Measurement by the Absolute Method, *J. Thermoelectricity* **1,** 67-76 (2012).
6. L.I.Anatychuk, M.V.Havrylyuk, V.V.Lysko, and Yu.I.Senyuk, Measurement of Thermoelectric Properties of Materials at High Temperatures, *J.Thermoelectricity* **6**, 72-77 (2013).
7. Anatychuk L.I., Lysko V.V. On the Improvement of the Accuracy and Speed in the Process of Measuring Characteristics of Thermoelectric Materials, *Proc. of the 11th ECT*, Netherlands, 2013, p. 64.

Submitted 03.10.14

NEWS
OF INTERNATIONAL THERMOELECTRIC ACADEMY

JOHN STOCKHOLM

(Dedicated to 80th anniversary)

October 14, 2104 is the 80th jubilee date of John Stockholm – Vice-President of the International Thermoelectric Academy, a member of "Journal of Thermoelectricity" editorial board, a well-known investigator and engineer in the area of thermoelectricity, president of company Marvel Thermoelectrics, France.

John Stockholm was born in Neuilly sur Seine (France). A wide range of acquired knowledge, all-round education (Diploma in Engineering of Ecole Nationale, academic degree of the University of Lille (France) and Master of Arts Harward University, Cambridge, Massachusetts (USA) enabled his successful work in various fields of technology (mechanics, heat engineering, environmental protection and plasma technique).

However, the scientist gave preference to thermoelectricity where he excelled in big achievements in the field of thermoelectric materials, simulation and development of cooling systems, production organization and introduction into practice of numerous thermoelectric instruments and devices. Special mention should be made of his papers on using thermoelectricity for air-conditioning on the terrestrial, sea and submarine transport and solving other relevant problems.

John Stockholm is the author of numerous publications and patents in thermoelectricity, participant in the international conferences, forums and meetings on thermoelectric issues. His presentations to these scientific meetings always arouse a big interest, being notable for a wide range of raised problems and their solutions, the realism and understanding of the needs of both manufacturers and consumers of thermoelectric products.

John Stockholm, an expert and connoisseur of his native European culture, promotes the development of culture, science and technology in many countries worldwide, actively approves himself in the international scientific and organizational activities; as recognition of it, he was elected President of the International Thermoelectric Society (1991-1993). Today he is a board member of this society, Vice-President of the International Thermoelectric Academy, a member of EUROSCIENCE society, European Thermoelectric Society, American Association for the Advancement of Science, Materials Research Society (USA), American Society of Heat, Refrigerating and Air-Conditioning Engineers, American Society for Engineering Education, The National Council of Engineers and Scientists of France, French Association for the Advancement of Science.

For his multifarious and fruitful scientific and organizational activities, in particular, for the scientific achievements in thermoelectricity, John Stockholm was awarded by silver medal of Society for Progress Encouragement (France, 1996), diploma of the International Thermoelectric Academy (2002) and Honorary Golden Prize in the nomination "For a Fundamental Contribution to Thermoelectricity" (2004).

The International Thermoelectric Academy, Institute of Thermoelectricity of the National Academy of Sciences and Ministry of Education and Science of Ukraine, "Journal of Thermoelectricity" Editorial Board cordially greet John Stockholm on his glorious jubilee and wish him sound health and new creative success.

ANDRIY OLEHOVYCH TEUT

(Dedicated to 60th anniversary)

September 3, 2014 is the date of 60-th anniversary of Andriy Olehovych Teut – a well-known specialist in the field of semiconductor materials science, academician of the International Thermoelectric Academy, PhD in Engineering and Head of Laboratory at State Affiliate "The Eastern Mining-and-Metallurgical Research Institute for Nonferrous Metals".

A.O. Teut took up the problems of manufacturing (synthesis) of thermoelectric materials, thermoelement leg blanks (pressed, extruded, zone-levelled) for coolers and generators in 1981, working as equipment operator, process engineer, head of shop department. The consumers of marketable products were the enterprises of Leningrad (now Saint-Petersburg), Moscow, Kyiv, Odessa, Lviv, Chernivtsi and other cities. A.O. Teut took part in the development of new materials and improvement of their production techniques.

In 1984, while continuing to work, A.O. Teut joined a post-graduate course of Moscow Institute of Steel and Alloys (department of semiconductor materials science). In 1990 he maintained PhD thesis "Optimization of technique for manufacturing legs for thermoelectric cooling devices extruded from $Bi_2Te_{2.7}Se_{0.3}$ alloys".

In 1994 A.O. Teut was elected academician of the International Thermoelectric Academy. Since 1996, when he was appointed as chief metallurgist (later director of research) of Pilot lead plant, the range of his scientific interests has widened considerably, the work in thermoelectricty has been combined with solving the problems of ore concentration, metallurgy of non-ferrous and precious metals.

Today A.O. Teut takes part in the development of innovation project for organization of production of thermoelectric power converters based on domestic raw materials base of the Republic of Kazakhstan.

The main lines of scientist's research and practical developments are as follows:

– semiconductor materials science;

– thermomechanical treatment of thermoelectric materials;

– development and mastering of technique for manufacturing of thermoelement legs for semiconductor power converters;

– technological and engineering development of semiconductor thermal into electric energy converter and manufacturing of a prototype of thermoelectric current generator.

A.O. Teut is the author of numerous scientific publications in peer-reviewed journals, as well as the patents "Laboratory mill for bulk materials" and "Method for the production of semiconductor materials based on metal chalcogenides". The scientist delivered reports on the problems of research and application of semiconductor materials.

For successes in the scientific and production activity A.O. Teut has been awarded with Third Class Order of Labour Valour and Third Class Badge of the Ministry of Industry and Trade of the Republic of Kazakhstan.

The International Thermoelectric Academy, Institute of Thermoelectricity of the National Academy of Sciences and Ministry of Education and Science of Ukraine, "Journal of Thermoelectricity" Publishers cordially greet Andriy Olehovych Teut on his 60-th jubilee and wish him sound health, happiness and new achievements.

ARTICLE PREPARATION RULES

The article shall conform to the journal profile. The article content shall be legible, concise and have no repetitions.

The article shall be submitted to the editorial board in electronic version.

The text shall be typed in text editor not lower than MS Word 6.0/7.0.

Page setup: "mirror margins"- top margin – 2.5 cm, bottom margin – 2.0 cm, inside – 2.0 cm, outside– 3.0 cm, from the edge to page header – 1.27 cm, page footer – 1.27 cm.

Graphic materials, pictures shall be submitted in color or, as an exception, black and white, in .opj or .cdr formats, .jpg or .tif formats being also permissible. According to author's choice, the tables and partially the text can be also in color.

The article shall be submitted in English on A4 paper sheets; the number of pages shall not exceed 12. By agreement with the editorial board, the number of pages can be increased.

To accelerate publication of the article, please adhere to the following rules:

- the authors' initials and names are arranged in the centre of the first page at the distance of 1 cm from the page header, font Times New Roman, size 12 pt, line spacing 1.2;
- the name of organization, address (street, city, postal code, country) – indent 1 cm below the authors' initials and names, font Times New Roman, size 11 pt, line spacing 1.2, center alignment;
- the title of the article is arranged 1 cm below the name of organization, in capital letters, semi-bold, font New Roman, size 12 pt, line spacing 1.2, center alignment. The title of the article shall be concrete and possibly concise;
- the abstract is arranged 1 cm below the title of the article, font Times New Roman, size 10 pt, in italics, line spacing 1.2 ,center alignment;
- key words are arranged below the abstract, font Times New Roman, size 10 pt, line spacing 1.2, justified alignment. The title "Key words" – font Times New Roman, size 10 pt, semi-bold;
- the main text of the article is arranged 1 cm below the abstract, indent 1 cm, font Times New Roman. size 11 pt, line spacing 1.2, justified alignment;
- formulae are typed in formula editor, fonts Symbol, Times New Roman. Font size is "normal" – 12 pt, "large index" – 7 pt, "small index" – 5 pt, "large symbol" – 18 pt, "small symbol" – 12 pt). The formula is arranged in the text, centre aligned and shall not occupy more than 5/6 of the line width, formulae are numbered in round brackets right;
- dimensions of all quantities used in the article are represented in the International System of Units (SI) with the explication of the symbols employed;
- figures are arranged in the text. The figures and pictures shall be clear and contrast; the plot axes – parallel to sheet edges, thus eliminating possible displacement of angles in scaling;
- tables are arranged in the text. The width of the table shall be 1 cm less than the line width. Above the table its ordinary number is indicated, right alignment. Continuous table numbering throughout the text. The title of the table is arranged below its number, center alignment;
- references should appear at the end of the manuscript. References within the text should be enclosed in square brackets. References should be numbered in order of first appearance in the text. Examples of various reference types are given below.

– L.I. Anatychuk, *Thermoelements and Thermoelectric Devices: Handbook* (Kyiv: Naukova Dumka, 1979), p.766. (Book)
– T.M. Tritt, Thermoelectric Phenomena, Materials, and Applications, *Annual Review of Materials Research* **41**, 433 (2011). (Journal paper)
– U. Ghoshal, *Proceedings of the XXI International Conference on Thermoelectrics* (N.Y., USA, 2002), p. 540. (Proceedings Conference)

The article should be supplemented by:

• letter from the organization where the work was performed or from the authors of the work applying for the publication of the article;

• information on the author (authors): last name and initials; full name and postal address of the institution where the author works; academic degree; position; telephone number; E-mail;

• author's (authors') photo in color or, as an exception, in black and white. With the number of authors more than two their photos are not given;

• author's application to the following effect:

We, the undersigned authors, … transfer to the founders and editors of "Journal of Thermoelectricity" the right to publish the article…in Ukrainian, Russian and English. This is to confirm that the present publication does not violate the copyright of other persons or organizations.

Date Signatures

Below is given an example of article preparation.

Author's photo 3 × 4 cm

A.I. Casian[1], B.M. Gorelov[2]

[1]Technical University of Moldova,
168, Stefan cel Mare Ave.,
Chisinau, MD-2004, Moldova;
[2]Institute of Surface Chemistry of National Academy
of Sciences of Ukraine, 17, Gen. Naumov Str.,
Kyiv, 03164, Ukraine

Author's photo 3 × 4 cm

STATE OF THE ART AND PROSPECTS OF THERMOELECTRICITY ON ORGANIC MATERIALS

The aim of the paper is to analyze the expected thermoelectric opportunities of organic materials, including some highly conducting quasi-one-dimensional crystals. It is shown that interest of investigators in these materials has been growing recently. Quasi-one-dimensional organic crystals have high prospects for thermoelectric applications. These materials combine the properties of multi-component systems with more diverse internal interactions and of quasi-one-dimensional quantum wires with increased density of electronic states. It is shown that the values of the thermoelectric figure of merit ZT ~ 1.3 – 1.6 at room temperature are expected in really existing organic crystals of tetrathiotetracene-iodide, TTT_2I_3, if the crystal parameters are approaching the optimal ones.

Key words: thermoelectricity, tetrathiotetracene-iodide, polarizability.

Introduction

It is known that conducting organic materials usually have much lower thermal conductivity than the inorganic materials. Moreover, the organic materials can be fabricated by simpler chemical methods, and it is expected that such materials will be less expensive in comparison with the inorganic ones. Exactly these properties attracted attention to such materials for the use in thermoelectric (TE) applications long time ago [1, 2]. In spite of relatively high value of the thermoelectric figure of merit $ZT = 0.15$ at room temperature observed in polycopper phthalocyanine [2] as early as 1980, the thermoelectric properties of organic materials are still weakly investigated. This situation has the only explanation that thermoelectricians are still weakly interested in organic materials, and organic chemists are also weakly interested in thermoelectric materials. Moreover, in order to seek good organic thermoelectrics, it is necessary to organize multidisciplinary consortiums of physicists, organic chemists and engineers in the field of thermoelectricity. …

The aim of this paper is to present briefly the state-of-the-art of investigations in the area of new organic thermoelectric materials and to describe the nearest expected results for really existing quasi-one-dimensional organic crystals of tetrathiotetracene-iodide, TTT_2I_3.

Quasi-one-dimensional organic crystals of TTT_2I_3

The structure of quasi-one-dimensional organic crystals of tetrathiotetracene-iodide, TTT_2I_3, has been briefly described in [34]. These needle-like crystals are formed of segregate chains or stacks of planar molecules of tetrathiotetracene *TTT*, and iodine ions. The chemical compound TTT_2I_3 is of mixed-valence: two molecules of *TTT* give one electron to the iodine chain which is formed from I_3^- ions. The

conductivity of iodine chains is negligibly small, so that only *TTT* chains are electrically conductive and holes serve as carriers. The electrical conductivity σ along *TTT* chains at room temperature varies between 10^3 and $10^4\ \Omega^{-1}\text{cm}^{-1}$ for crystals grown by gas phase method [35], and between 800 and $1800\ \Omega^{-1}\text{cm}^{-1}$ for crystals grown from solution [36]. Thus, the conductivity is very sensitive to crystal impurity and perfection which depends on growth method. In the direction perpendicular to chains σ is by three orders of magnitude smaller than in the longitudinal direction and is neglected. …

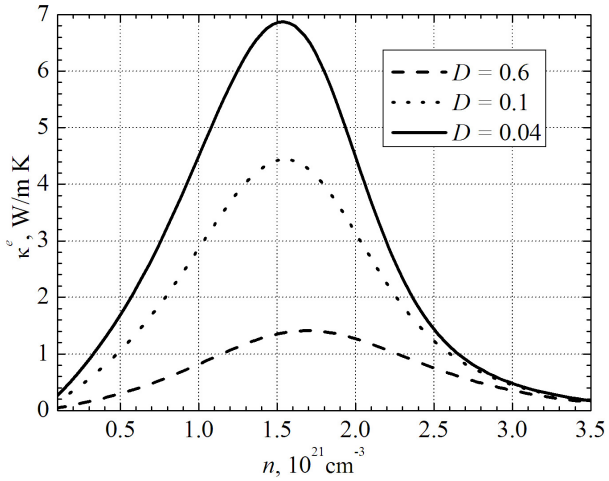

Fig. 1. Dependences of electron thermal conductivity κ^e *on n.*

$$\sigma = R_0,\ S = R_1 / eTR_0,\ \kappa^e = \left(e^2T\right)^{-1}\left(R_2 - R_1^2 / R_0\right), \tag{1}$$

Thermoelectric properties

Expressions (2) – (3) have been calculated in order to determine the thermoelectric properties of quasi-one-dimensional organic crystals of TTT_2I_3 with different degrees of purity….

Conclusions

The state-of-the-art of research on new organic materials for thermoelectric applications is analyzed. It is shown that the interest of investigators in these materials has been growing in recent years. The highest value of $ZT \sim 0.38$ at room temperature has been measured in doped acetylene, with the only problem that this material is not stable. Accurate control of the oxidation level in poly (3, 4-ethylenedioxythiophene) (PEDOT) gave the power factor $324\ \mu\text{W}\cdot\text{m}^{-1}\text{K}^{-2}$ and in combination with its low intrinsic thermal conductivity ($\kappa = 0.37\ \text{W}\cdot\text{m}^{-1}\text{K}^{-1}$) yielded $ZT = 0.25$ at room temperature, and this material is air-stable….

References

1. Ali Shakouri, Recent Developments in Semiconductor Thermoelectric Physics and Materials, *Annu.Rev.Mater.Res*.**41**, 399-431 (2011).
2. L.I. Anatychuk, *Thermoelectricity, Vol.2, Thermoelectric Power Converters* (Kyiv, Chernivtsi: Institute of Thermoelectricity, 2003), 376p.
3. M.E. Bengen, *German Patent Appl*. OZ 123, 438, 1940; *German Patent* 869,070, 1953, Tech. Oil Mission Reel, 143,135, 1946.